Sensor Fault Detection and Isolation for Degrading Lithium-ion Batteries in Electric Vehicles

by

Manh-Kien Tran

A thesis

presented to the University of Waterloo

in fulfillment of the

thesis requirement for the degree of

Master of Applied Science

in

Chemical Engineering

Waterloo, Ontario, Canada, 2020

Author's Declaration

I hereby declare that I am the sole author of this thesis. This is a true copy of the thesis, including any required final revisions, as accepted by my examiners.

I understand that my thesis may be made electronically available to the public.

Abstract

With the increase in usage of electric vehicles (EVs), the demand for lithium ion (Li-ion) batteries is also on the rise. A Li-ion battery pack in an EV consists of hundreds of cells and requires a battery management system (BMS). The BMS plays an important role in ensuring the safe and reliable operation of the battery in EVs. Its performance relies on the measurements of voltage, current and temperature from the cells through sensors. Sensor faults in the BMS can have significant negative effects on the system, hence it is important to diagnose these faults in real-time. Existing sensor fault detection and isolation (FDI) methods are mostly state-observer-based. State observer methods work under the assumption that the model parameters remain constant during operation. Through experimental results, this thesis shows that degradation can affect the long-term performance of the battery and its model parameters, hence it can cause false fault detection in state observer FDI schemes. This thesis also presents a novel model-based sensor FDI scheme for a Li-ion cell, that takes into consideration battery degradation. The proposed scheme uses the recursive least squares (RLS) method to estimate the equivalent circuit model (ECM) parameters in real-time. The estimated ECM parameters are put through weighted moving average (WMA) filters, and then cumulative sum control charts (CUSUM) are implemented to detect any significant deviation between unfiltered and filtered data, which would indicate a fault. The current and voltage sensor faults are isolated based on the responsiveness of the parameters when each fault occurs. Finally, the proposed FDI scheme is validated by conducting a series of experiments and simulations. Various injection times, fault sizes, fault types and cell capacities are considered. The results show that the proposed scheme consistently detects and isolates voltage and current sensor faults at different cell capacities in a reasonable time, with no false or missed detection. The preliminary findings are promising, but in order for the proposed FDI scheme to be utilized in practical settings, more work is needed to be done. The scheme should be expanded to include FDI for temperature sensors. In addition, other battery models as well as other fault diagnosis methods, specifically knowledge-based ones, should be investigated. Furthermore, additional experiments, including longer test cycles and extension to modules and packs testing, need to be conducted to obtain more data to improve the reliability of the FDI scheme.

Acknowledgements

I would like to thank my family, friends, colleagues, professors and mentors who have helped me throughout my university career.

Firstly, I would like to acknowledge my supervisors, Dr. Michael Fowler and Dr. Roydon Fraser. They are great mentors with amazing dedication to the development of their students. Dr. Fraser guided me through the first few months of my graduate studies and introduced me to the UWAFT team where I was able to learn more about modeling and simulation. Dr. Fowler gave me my first co-op job in his lab which inspired me to come back for my Masters, and PhD in the future. I received an incredible amount of support and guidance from him that I will forever be grateful for. I would also like to thank Dr. Aiping Yu and Dr. Zhongwei Chen for their constructive feedback on my thesis.

I would also like to acknowledge Manoj Mathew who has been my "go-to" throughout my Masters. His expertise on the subject helped guide me through the project which eventually became my thesis. Thank you to the co-ops, Haocheng, Phillip, Nusayba, Mide and Xinge, for their help with running experiments and collecting data to assist my research. And to the UWAFT team, thank you for the great experience. I have met some amazing people in the team who motivated me, and I hope to collaborate with the team more in the future.

Thank you as well to all my friends, Paul, Olsi, Sky, Jack, Brandon, Matt and many others, for creating countless unforgettable memories with me in university. A special thank you to my girlfriend, Danielle, who provided constant support and motivation, and I could not have completed this thesis without her.

Finally, I would like to express my very profound gratitude to my parents for providing me with unfailing support and continuous encouragement throughout my years of study. They are my ultimate role models.

Dedication

I would like to dedicate my thesis to my beloved late grandmother who raised me with affection and love and made me the person I am today.

Table of Contents

List of Figures

List of Tables

List of Acronyms

EVs	Electric vehicles
BMS	Battery management system
FDI	Fault detection and isolation
RLS	Recursive least squares
ECM	Equivalent circuit model
WMA	Weighted moving average
CUSUM	Cumulative sum control charts
SOC	State of charge
SOH	State of health
UDDS	Urban Dynamometer Driving Schedule
LFP	Lithium iron phosphate
NMC	Lithium nickel manganese cobalt oxide
EOL	End-of-life
OCP	Open circuit potential
SEI	Solid electrolyte interface
OCV	Open-circuit voltage
EMI	Electromagnetic interference
CPD	Change point detection
EPA	Environmental Protection Agency
HWFET	Highway Fuel Economy Test
FTP	Federal Test Procedure
HPPC	Hybrid Pulse Power Characterization
APE	Average percent error
DT	Detection time
FDR	False detection rate
MDR	Missed detection rate

1. Introduction

The rise of gas prices and the negative effects of air pollution on public health and climate change have pushed the automotive industry to look for renewable energy sources and storage systems to provide for the needs of the future. Currently, non-renewable energy sources make up 27% of the energy used to meet the grid needs within the province of Ontario [1]. To decrease the dependency on non-renewable energy, the automotive industry has been developing electrified powertrains, which also help to increase overall vehicle efficiency and reduce emissions [2] [3] [4]. The electric vehicles (EVs) market is on the rise, due to factors such as cost-effectiveness, rising fuel prices, technological advancements, increasing R&D in the field, growing environmental concern worldwide, surge in government initiatives towards the protection of the environment [5]. Hybrid Electric Vehicles (HEVs), Plug-in Hybrid Electric Vehicles (PHEVs), and Battery Electric Vehicles (BEVs) have experienced a substantial increase in market share. In 2018, the global electric car fleet exceeded 5.1 million, up 2 million from the previous year and almost doubled the number of new electric car registrations [6]. The battery pack is a very important component in an EV, and most EVs nowadays are utilizing lithium-ion (Li-ion) battery pack as their energy storage system.

Li-ion batteries are the most popular energy storage in the world, amounting to 85.6% of the energy storage system utilized in 2015. Although it has the highest price, it shows the lowest cost per cycle [7]. The substantial demand for Li-ion batteries is due to portable devices and EVs. EVs require an energy storage system that can provide a great amount of power to accelerate the vehicle, sustain the energy for a large distance, and last for a long period of time after the vehicle life span begins. Thus, Li-ion batteries are used in EVs due to their high power and energy density, long life span and reduced environmental impact.

EVs require a battery system that consists of hundreds or thousands of single cells. In order to manage this large number of cells, the battery pack needs a battery management system (BMS). It is important that the performance of the BMS is accurate and reliable to ensure the performance and safety of EVs application. The functions of the BMS include state of charge (SOC) and state of health (SOH) estimation, battery safety and protection, cell monitoring and

balancing, charge control, and thermal management [8]. The functions are heavily dependent and can be seen in Figure 1. These functions rely heavily on voltage and current sensor measurements [9]. It is possible for the sensors to experience malfunctions during operation of the battery, due to manufacturing defects or environmental factors. The SOC and SOH estimation would be affected if there were any faults with the sensors, leading to over-charge and/or over-discharge phenomenon which would degrade the battery faster. The current and voltage protection would also fail to work properly due to faulty sensors [10]. Therefore, it is critical to develop an algorithm that can reliably and accurately diagnose any faulty operation of the voltage and current sensors in real-time.
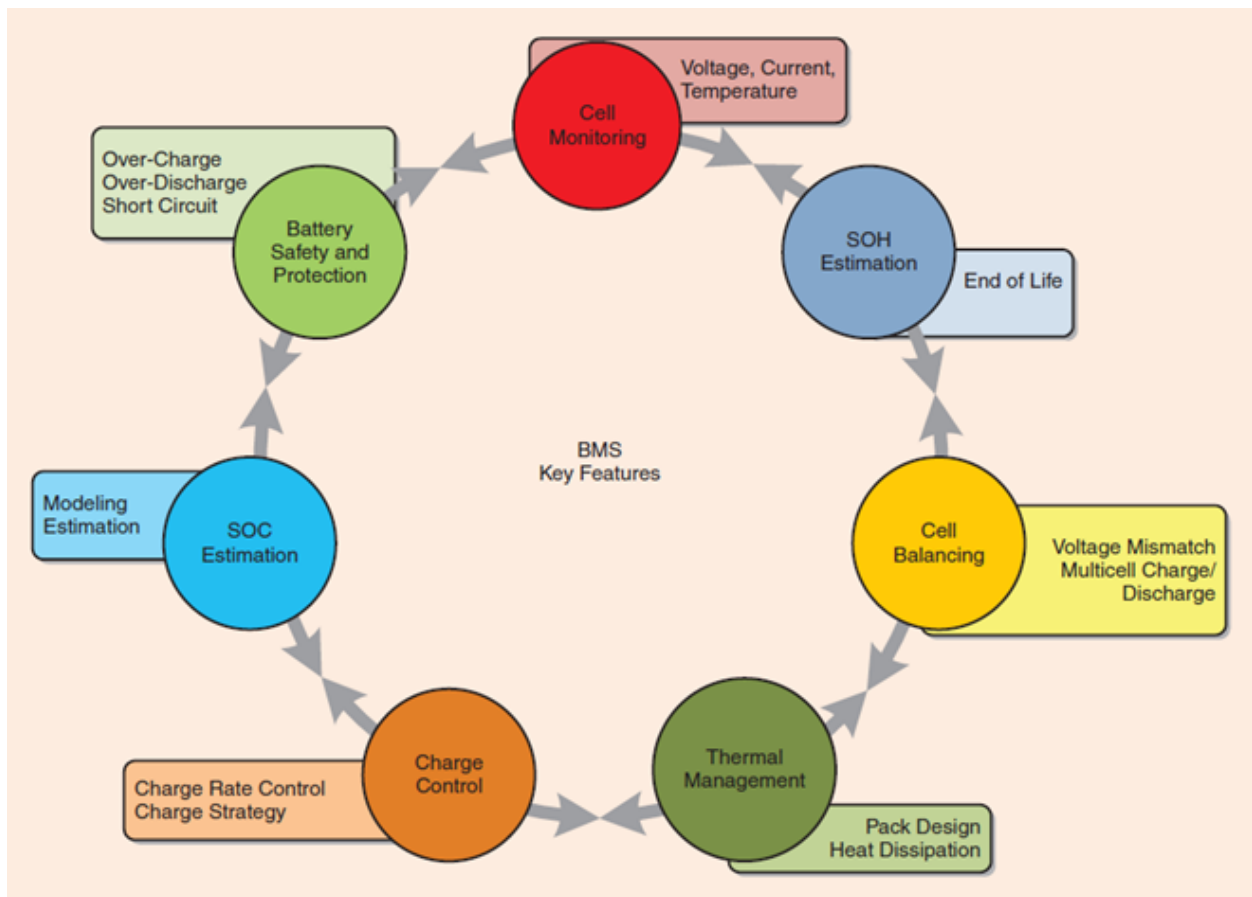
Figure 1. The BMS features. [15]

1.1. Motivation

There has been some research done on sensor fault detection and isolation (FDI) schemes, which are mostly state-observer-based. All of these methods work under the assumption that the battery model parameters remain constant throughout the battery pack's life span. However, the parameters can be affected by degradation, a significant property of battery operation. Currently, there has not been any mention of cell degradation in any FDI works done in literature.

There are a few models used to illustrate battery behavior, but the equivalent circuit model (ECM) is the most widely used in FDI works [11]. The parameters of the ECM were derived using the conservation of species, conservation of charge, and reaction kinetics in [12]. The results show that the parameters have physical meanings and can be affected by the chemistry of the battery as well as the environment of operation. Therefore, the degradation of the battery would have some effects on the parameters. The existing FDI schemes can be improved by integrating degradation into the ECM. However, this has been proven to be a difficult task. Currently, battery degradation models can be obtained by fitting experimental data under constant conditions. However, this is not an appropriate model for battery degradation in EVs application due to its complex operating state [13]. Experimental models are also less accurate, time-consuming and costly. Adaptive models are more accurate but require training to estimate the parameters that correlate with degradation. Moreover, the models can have high computational effort which is not suitable for real-time BMS applications [14]. Another approach is needed to effectively diagnose faults while considering the effect of degradation on ECM parameters, which this thesis will present.

1.2. Objectives and Contributions

The main objectives of this thesis are to outline the background, confirm the degradation effect on the ECM parameters, design an FDI scheme for voltage and current sensor faults, and validate its performance using a series of experiments. As the ECM parameters are expected to change during battery operation due to the effect of degradation, this thesis studies and confirms this

effect through a series of experiments. The proposed FDI scheme uses the recursive least squares (RLS) method to estimate the ECM parameters in real-time, then applies a weighted moving average (WMA) filter coupled with a cumulative sum control chart (CUSUM) to detect any voltage and current sensor faults. The use of RLS is suggested because of its low computational demand and easy implementation [15]. The implementation of the WMA filter eliminates the concern of battery degradation, in addition to the effect of SOC and temperature on ECM parameters. Furthermore, the sensor faults are isolated based on the responsiveness of the parameters when a specific fault occurs. Finally, the Urban Dynamometer Driving Schedule (UDDS) cycle with sensor fault simulation is applied to validate and evaluate the performance of the proposed FDI scheme for a lithium iron phosphate (LFP) cell. The key contribution of this thesis is the novel ability of the proposed FDI scheme to operate reliably when the battery undergoes degradation.

1.3. Thesis Outline

The rest of this thesis is organized as follows. Chapter 2 discusses the background and literature focusing on battery basics, BMS, sensor faults and fault diagnosis methods. Chapter 3 outlines the battery model used and the details of the proposed FDI scheme. Chapter 4 provides the experimental design and analysis of the effect of degradation and various faults on the parameters. The evaluation of the proposed fault diagnosis scheme is presented in Chapter 5, and the resulting conclusions are given in Chapter 6.

2. Background and Literature Review

2.1. Battery Basics

2.1.1. Batteries and Cells

A battery is a device that converts stored chemical energy into electrical energy by means of an electrochemical oxidation-reduction (redox) reaction. For a rechargeable battery, the process is reversed. The redox reaction occurring within batteries involves electrons being transferred from one material to another through an electric circuit. [8] [16] [17]. Because batteries convert chemical energy into electric energy through an electrochemical process, they are not subject to the limitations of the Carnot cycle, unlike combustion engines, and thus batteries have higher energy conversion efficiencies [18].

A battery consists of one or more cells, connected in series and/or parallel. The cell consists of three major components: the anode, the cathode, and the electrolyte. The anode is the negative electrode or reducing electrode, which produces electrons and is oxidized during the redox reaction. The anode is usually selected based on some specific requirements, including reducing potential, good conductivity, stability, ease of fabrication and low cost. Hydrogen, lithium and zinc are some examples of materials that have been used as the anode [19]. The cathode is the positive electrode or oxidizing electrode, which accepts electrons and is reduced during the redox reaction. A good cathode material should be an efficient oxidizing agent and have a useful working voltage, and some common materials are metallic oxides, oxygen and halogens [19]. The electrolyte, usually liquid, is the ionic conductor that provides the medium for ions to transfer between the anode and cathode. It should be nonreactive with the electrodes, stagnant with change in temperature, safe and cost-efficient. It should also be ionically conductive but not electronically conductive to prevent internal short-circuiting. There are many shapes and configurations for the cells, including cylindrical, button, and flat, and the components are designed to fit different cell shapes [18].

There are three common classifications for batteries: primary (nonrechargeable), secondary (rechargeable) and flow batteries. Primary batteries are normally discharged once and discarded due to their inability to be effectively recharged, but they have a good shelf life and high energy density at low discharge rates. They are a convenient, inexpensive and lightweight solution to many applications such as portable electronic devices, lighting, and cameras. Secondary batteries can be recharged electrically to their original state by passing the current in the opposite direction to that of the discharging process. They are used the same as primary batteries but instead of being discarded, they can be recharged to be used again. Some notable applications for this type of battery are cell phones and laptop computers. Secondary batteries usually possess traits like high power density and high discharge rate. Flow batteries utilize chemical energy outside of the battery in a fluid state. The fluid passes through the battery and reacts to produce electrical energy. An example of this type of battery is fuel cell [18].
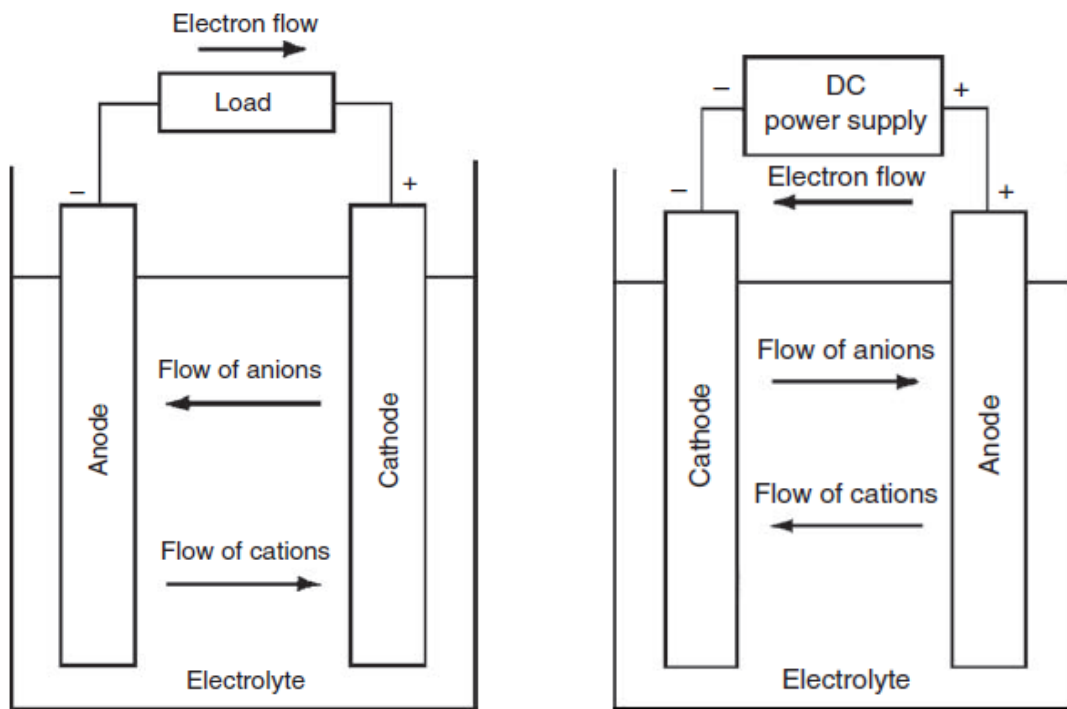
Figure 2. Electrochemical operation of a cell (left-discharge, right-charge). [18]

The operation of a cell (rechargeable) during the discharge and charge process is shown in Figure 2. During discharge, the cell is connected to an external load and the electrons flow from the

anode to the cathode through the load. In the electrolyte, the ions flow to their respective destination, completing the electric circuit. During the charge, the current flow in reverse, provided by a power supply, and the oxidation and reduction processes occur in the opposite electrode of the discharge (the positive electrode is now the anode and the negative is the cathode).

Some properties of batteries include voltage, capacity, energy, SOC and SOH:

- The theoretical voltage of a cell can be calculated from the standard electrode potentials. It is the difference between the voltage potential of the two electrodes. The theoretical voltage is modified by the Nernst equation, which takes into account the non-standard concentration and temperature of the cell during its operation. The actual potential changes with time either because of use or self-discharge by which the activity (concentration) of the electroactive component in the cell is modified. The actual voltage produce will always be lower than the theoretical voltage due to polarisation. It is also affected by the resistance losses (IR drop) of the battery which depends on the load current and the internal impedance of the cell. These factors are dependent on electrode kinetics and thus vary with temperature, SOC, and the age of the cell. The actual voltage appearing at the terminal needs to be sufficient for the intended application [18].

- The capacity of a cell is determined by the mass of active material contained in the cell, measured in coulombs or ampere-hours. It is essentially the quantity of electricity that can be obtained from the active materials. The cell capacity represents the maximum amount of energy that can be extracted from the battery under certain specified conditions. However, the actual energy storage capabilities of the battery can vary significantly from the nominal-rated capacity, as the battery capacity depends strongly on the age and operational history of the battery, the charging or discharging regimes of the battery, and the temperature [18].

- The energy of the cell considers both voltage and capacity, being the multiplication product of the two quantities. It is the maximum value in watthour that can be delivered by a specific electrochemical system. However, energy is not a good metric for cell specification because only a fraction of the theoretical energy of the battery is realized,

7

due to the need for electrolyte and other nonreactive components such as containers, electrodes and separators. Better metrics used for batteries to evaluate their performance are specific energy (Wh/kg) and energy density (Wh/L). The specific energy density is the energy that can be derived per unit weight of the cell. The energy density is the energy that can be derived per unit volume of the weight of the cell [18]. For example, the development of pouch cells significantly decreased the weight and volume of the cell, increasing its specific energy and energy density when compared to past cell shapes, and thus making it more efficient and viable to use.

- The SOC is defined as the available capacity expressed as a percentage of some reference, which can sometimes be the rated capacity of the cell, and sometimes its current (latest) capacity. It is not usually an absolute measure in Coulombs, kWh or Ah of the energy left in the cell. The fact that it is not an absolute measure combining with unclear reference point creates some confusion around the SOC estimation. The preferred SOC reference should be the rated capacity of a new cell rather than the current capacity of the cell. This is due to the fact that the cell capacity gradually reduces as the cell ages [18]. For example, towards the end of the cell's life, its actual capacity, even when the cell is fully charged, will be approaching only 80% of its rated capacity. Therefore, in this case, the cell SOC would only be 80% of its rated capacity [20]. Even though this is the case, some applications still use the cell's current capacity as the reference point, including EVs [21]. This is because the SOC in EVs is normally regarded to as the "fuel" gauge. This value gives the users a sense of how much "fuel" is left in their battery. If the battery is indicating a "fuel" level of 80% even when it is fully charged, the users will believe that their battery is not working properly, even though this behavior should be expected from a battery. Using the current capacity rather than the rated capacity is usually a design shortcut to avoid the complexity of determining and allowing for the age-related capacity adjustments, which are often conveniently ignored.
- The SOH is defined as the measurement of the general condition of a battery and its ability to deliver the specified performance compared with a fresh battery. It takes into account factors such as charge acceptance, internal resistance, voltage and self-discharge. It

measures the long-term capability of the cell and gives an indication, not an absolute measurement, of how much of the available "lifetime energy throughput" of the battery has been consumed, and how much is left [18]. In EVs application, it can be analogized to the "odometer" display function which indicates the number of miles traveled since the vehicle was new.

2.1.2. Li-ion Batteries

Since the application of EVs requires high power density and discharge rate, secondary batteries are the most suitable solution. The ability to be recharged also allows for convenience and cost savings, because of the complexity of battery replacement in that application [22]. One of the most important aspects involving the use of batteries in EVs is the range of the vehicle. Users want longer driving range and better performance, which requires a battery solution that has high energy and power density, low weight and small volume. Li-ion batteries satisfy many of the EVs application requirements [23]. As can be seen in Figure 3, they possess higher energy potential while maintaining a smaller size and weight compared to other rechargeable batteries.
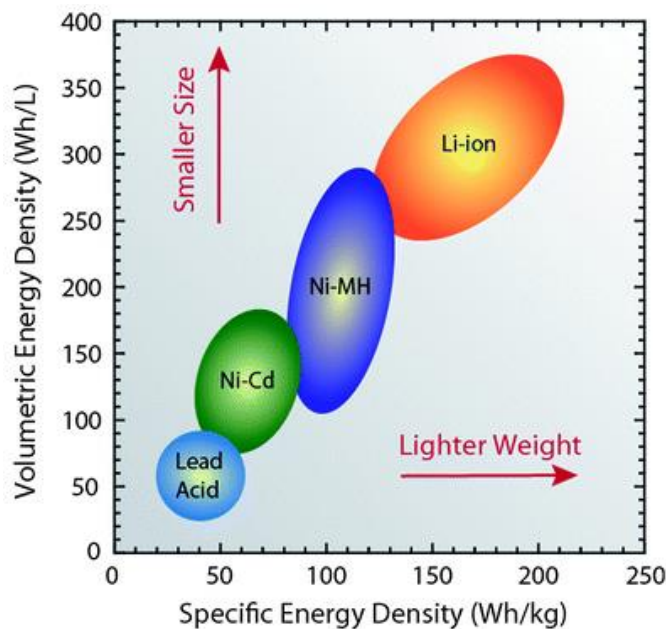
Figure 3. Ragone plot for different cell chemistry. [22]

9

Li-ion batteries utilize lithium compounds for both positive and negative electrodes. The Li^+ ions move back and forth between the electrodes as the cell cycles. The negative electrode material is commonly graphite, used for its availability, cycling performance and safety, layered on a copper current collector. The positive electrode has been researched more, with many available materials such as $LiCoO_2$ (LCO), $LiMn_2O_4$ (spinel), $LiFePO_4$ (LFP) and $Li(NiMnCo)O_2$ (NMC) [24] [25]. These materials each have different advantages which are appropriate for different applications, such as low cost, high thermal stability, long cycle life, high rate capability and high capacity.

Positive:
$$LiMO_2 \underset{\text{Charge}}{\overset{\text{Discharge}}{\rightleftarrows}} Li_{1-x}MO_2 + x\ Li^+ + x\ e^-$$

Negative:
$$C + y\ Li^+ + y\ e^- \underset{\text{Charge}}{\overset{\text{Discharge}}{\rightleftarrows}} Li_yC$$

Overall:
$$LiMO_2 + x/y\ C \underset{\text{Charge}}{\overset{\text{Discharge}}{\rightleftarrows}} x/y\ Li_yC + Li_{1-x}MO_2$$
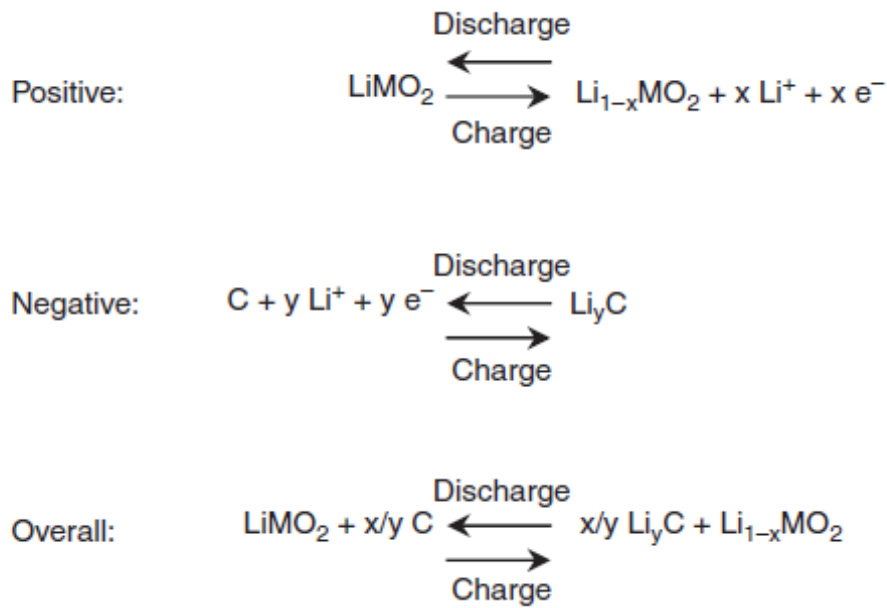
Figure 4. Reactions within Li-ion battery cell. [22]

When a Li-ion cell is charged, the active material from the positive electrode is oxidized and the material from the negative electrode is reduced. During this process, lithium ions are deintercalated from the positive to the negative side [24]. The reactions are shown in Figure 4, where $LiMO_2$ represents the metal oxide such as $LiCoO_2$ and C represents the carbonaceous material such as graphite. The graphical schematic of the cell in operation of discharge and charge is shown in Figure 5.
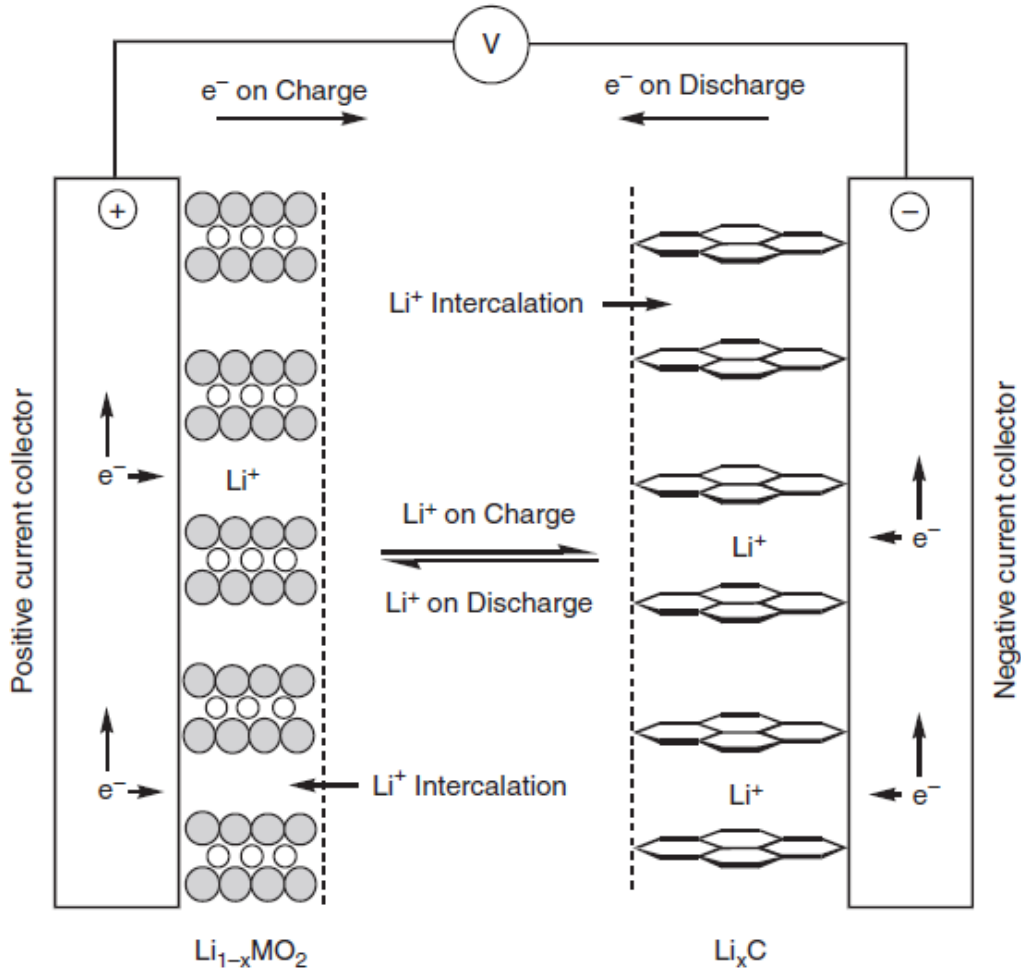
Figure 5. Schematic of Li-ion cell in operation of discharge and charge. [22]

2.1.3. Use of Li-ion Batteries in EVs Application

The big and relatively new application for Li-ion cells between 2010 and 2020 is electrified vehicles [24]. Some advantages of Li-ion batteries allow for this to occur: long cycle life, broad operating temperature range, long shelf life, rapid charge capability, high-power discharge capability, high specific energy and energy density, and ability to be contained in a pouch (for size and weight reasons). However, there are also some disadvantages to Li-ion batteries, namely: not cost-efficient for big applications, susceptible to degradation at high temperature, needs for protective circuitry, capacity loss and possible thermal runaway when overcharged, venting and

possible thermal runaway when crushed [22]. Most of the disadvantages involve safety, and batteries used in automotive vehicles should be designed and built to the highest standard for the requirements of both safety and function of the application. Therefore, Li-ion batteries used in EVs typically employ a management system combined with mechanical disconnect devices to provide protection from overcharge, over-discharge or extreme temperature conditions [22].

2.1.4. Battery Degradation

Li-ion batteries are the most commonly used energy storage system in EVs, due to its energy-to-weight ratio and low self-discharge rate [18]. However, in order to make a significant impact on the existing automotive market, these batteries must satisfy performance requirements and last long enough for customers to be interested [26]. Battery degradation is one of the factors that can affect performance in EVs since it directly affects battery lifetime, the measure of battery performance and longevity. Degradation can be quantified as runtime on a full charge (estimated in Ah) or as the number of charge/discharge cycles until it degrades irreversibly [27]. For vehicle use, the end-of-life (EOL) point is defined to be when the battery has degraded to 80% of its original SOC [28].

It was determined that the performance loss of the battery is caused by many different mechanisms [29]. These mechanisms are often difficult to identify and quantify due to the complexity of the reactions and physical changes taking place inside the battery while under operation. The common effects are capacity fade and impedance increase, but the degree of these are distinct depending on the conditions the battery operates at or is stored at and the materials that make up the battery [26]. While the degree of degradation can vary, its occurrence over time is inevitable. The aging mechanisms can be grouped into two categories, calendar aging and cycling aging.

Calendar aging is the degradation of the battery over time when the battery is stored under open circuit potential (OCP) conditions [23] [30]. Essentially, the battery will lose its capacity with time, even if it is not being used. Even though the effect of calendar aging is less than that of cycling

aging, a vehicle is normally parked for most of its service life, hence, EV battery would experience this type of aging the most [23]. The loss of capacity in the cell with time can be reversible and irreversible loss [31]. The reversible capacity loss is the result of the spontaneous re-intercalation of the Li ions from the electrolyte into the unstable cathode when the cell is fully charged [32]. The irreversible capacity loss can be attributed to the side reactions occurring within the cells [31] [33]. These reactions can be caused by the operating conditions of the battery, namely temperature and SOC. With high temperatures, secondary reactions such as corrosion proliferate can occur, causing losses of usable lithium [26]. In research conducted by Grolleau et al., Li-ion cells stored at different temperatures were found to experience different degrees of capacity fade. Cells stored at 30°C experienced less than 10% capacity loss after 450 days of storage, while capacity fade was 20% for cells stored at 45°C. Cells stored at 60°C reached a 20% capacity loss after only 60 days [23]. For the effect of SOC, Ohue et al. showed that cells stored at the same temperature but different SOCs have different aging results. The cells stored at higher SOCs experienced increased degradation effect [34]. This is because, at higher SOC, there are significantly more Li ions available at the graphite electrode to partake in potential side reactions there.

Cycling aging refers to aging mechanisms that occur within the cell while it is operating under load. The losses for this type of aging are typically irreversible [35]. They include the loss of capacity in the formation of the solid electrolyte interface (SEI) layer (occurs at both electrodes), loss of active materials due to dissolution, structural degradation and electrode delamination, and impedance increase from the formation of the SEI layer that passivates the active particle surface [35]. Aging can occur at both electrodes, but the most prominent loss of capacity has been determined to occur at the anode [17]. The primary source of aging at the anode is the formation of the SEI layer. As the cell is cycled, the graphite is exposed to the electrolyte resulting in the utilization of more lithium to form an SEI over the exposed surface. This leads to the loss of cyclable lithium in the cell as well as an increase in resistance on the electrode. There are also many other factors that can induce the aging of the battery at the anode, which are summarized in Figure 6. Aging can also occur at the cathode, due to structural factors and SEI formation, similar to the anode [30]. The electrolyte can also be a reason for cycling aging, since the

13

materials used in the electrolyte have the capability to undesirably react at low voltage [36]. This can sometimes produce gaseous species in the cell and lead to swelling of the cell, which is a major safety concern [37].
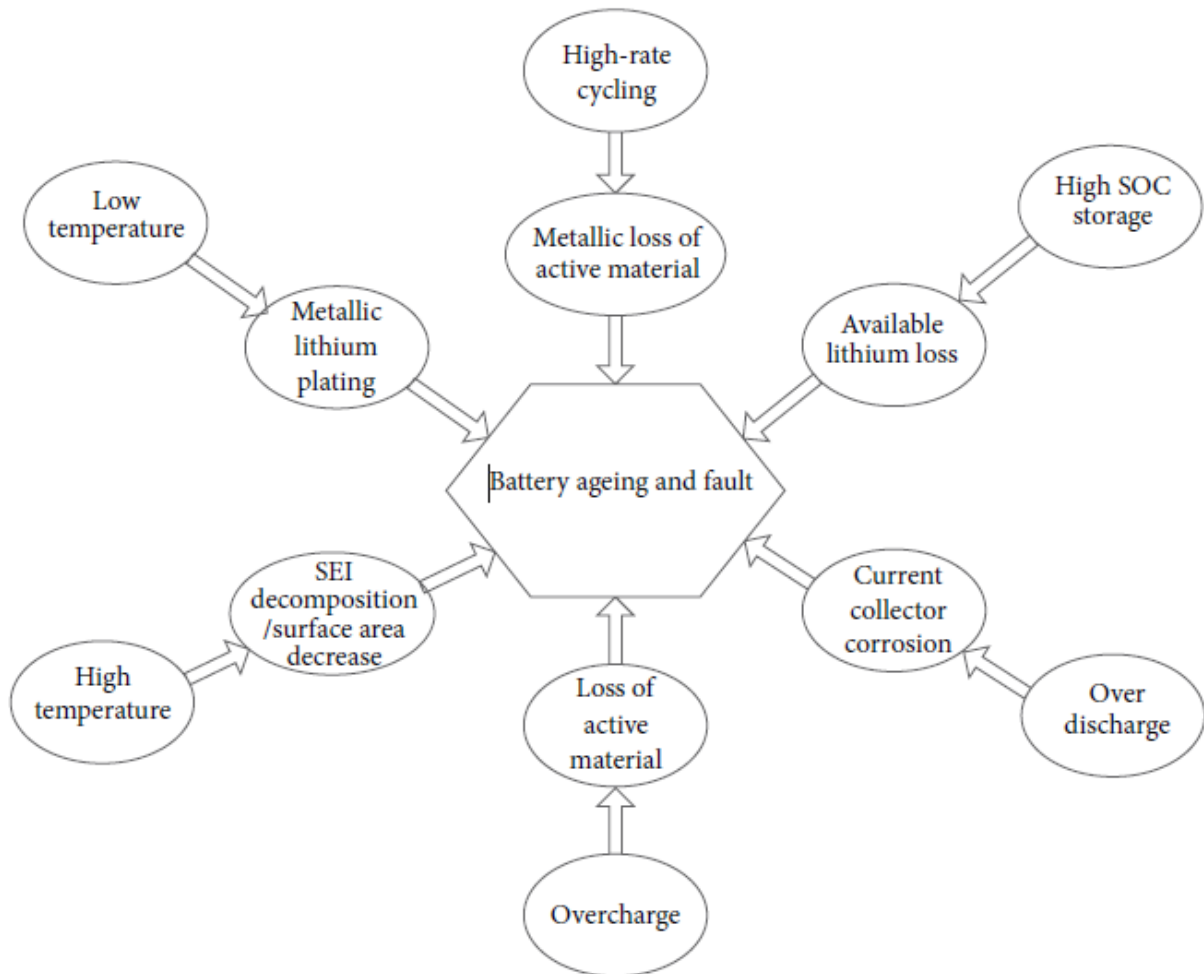
Figure 6. Causes for battery ageing at anode and their effects. [11]

2.2. Battery Models

In order to manage and control the battery with a smart system, it is necessary to understand how the battery behaves in various conditions. This prompts the need for mathematical modeling

of battery systems, in order to predict the system behaviors and provide appropriate safety measures. There have been many suggested battery models in literature, with different levels of detail depending on their intended use.

Mathematical models for batteries started out as empirical relationships between measured parameters, such as battery voltage, overall resistance, temperature of the cell and remaining capacity. With more research being done on battery models, chemistry-based and physics-based models were developed. Some models are the combination of all the above. The three most commonly used types of battery models are electrochemical, empirical and electrical.

Electrochemical models are based on the physical aspects of the battery and characterize power, current and voltage. The models use equations developed from the chemical processes that occur within the cell. Some examples of these equations include Fick's law, Ohm's law, the Butler-Volmer and Tafel equations [33]. These models are usually highly accurate because they can describe the behavior of the battery in great detail. However, due to the level of detail of these models, they are often too complex and computationally inefficient, especially for the use of online applications like EVs. These models often involve a system of coupled time-variant spatial partial differential equations and battery-specific information that is difficult to obtain. The solver may take hours or even days to solve the equations within these models, making them unsuitable for real-time use. These types of battery models are mostly used in research settings, not in battery management systems for vehicles.

Empirical models, also known as mathematical models, use experimental data from cells to predict behavior of the battery in similar conditions. These models only fit the data without considering the physical or chemical principles that would require large computing requirements. This is more feasible for real-time applications. However, they cannot offer any information on characteristics of the battery which are critical for use in control and optimization algorithms. Also, since they are only based on a limited amount of data in certain conditions, these models cannot predict with high accuracy the battery behavior in other operational conditions [38]. The EV applications are constantly in flux, hence, these models would not satisfy the requirements to be used in EVs [33]. With the rise of the data analysis and machine learning fields nowadays,

these models will eventually be developed to have the highest accuracy out of all the types of battery models, when an adequate amount of data is collected [38].

Electrical models predict the terminal characteristics of the battery, such as current and voltage, through variations of equivalent circuits [39]. An equivalent circuit is a theoretical circuit consisting of electrical components that represent various behaviors of the battery during its operation [20]. Electrical models can efficiently monitor the performance of the battery and other critical battery parameters such as SOC and SOH. They are more intuitive, useful and easy to use for engineers. Electrical models are becoming important in order to compute battery parameters, because of their adaptability (for real-time use). This ability to be adaptive makes electrical models the most feasible ones to be used in EVs. There are numerous electrical-based methods to model a battery, and a few of them taken from literature are illustrated below.

2.2.1. Simple Battery Model

This model consists of an open-circuit voltage (OCV) and a constant internal resistance, as can be seen in Figure 7. The internal resistance can be obtained from open-circuit measurements and one extra measurement with a load connected at the terminal. The terminal voltage V0 can be determined from open-circuit measurement [40].
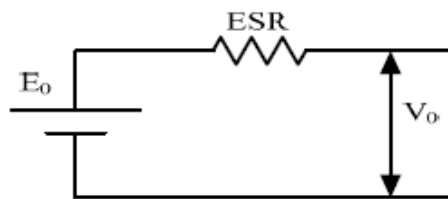
Figure 7. Circuit of the simple battery model. [44]

This model is simple and easy to work with, but it also has several disadvantages. It does not consider the varying internal resistance due to changes in SOC and electrolyte concentration. The undermining importance of SOC in this model makes it unviable to be used for battery monitoring in EVs.

2.2.2. Modified Battery Model

This model has the same schematic as the previous model but with some improvements. In this model, the ESR is not constant but a function of the battery SOC. A common formula is shown below [41].

$$ESR = \frac{R_0}{S^k} \tag{2.1}$$

where R_0 is the internal battery resistance when the battery is fully charged, k is the coefficient representing the battery discharge rate calculated using manufacturers data and

$$S = 1 - \frac{Ah}{C_i} \tag{2.2}$$

where C_i is the initial capacity of the battery when fully charged, and Ah represents the capacity used during operation. S, representing SOC, varies from 0 (fully discharged) to 1 (fully charged). This model takes into account the change in SOC, but it does not illustrate the transient behavior of the battery and the transient time constant.

2.2.3. Thevenin-Based Model

As can be seen in Figure 8, the Thevenin model uses a resistor and an RC parallel pair to predict the battery response to a transient load at a particular SOC where the OCV is assumed to be constant [42]. The $R_{self-discharge}$ represents the self-discharge phenomena of the battery. The R_{series} accounts for the internal resistance of the battery and the parallel RC network represents the transient behavior of the battery and the time constant for the transient conditions. This is a good model because it has the ability to accurately describe the battery behavior while retaining a certain degree of simplicity. However, it cannot capture runtime information of the battery.
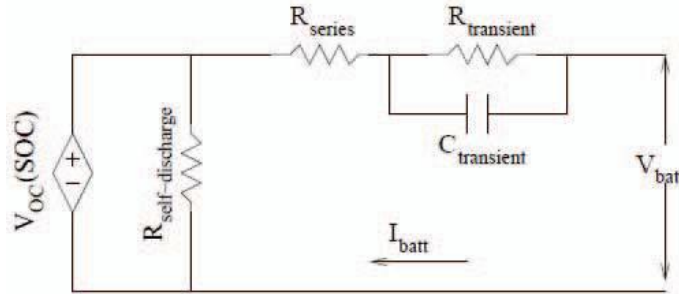
Figure 8. Thevenin equivalent model including transient behavior. [44]

2.2.4. Impedance-Based Model

This model consists of R_{series} and L_{series} to account for the internal resistance of the battery, and impedance Z_{ac} to model the electrochemical portion of the battery, as shown in Figure 9. The impedance-based model uses electrochemical impedance spectroscopy to obtain an ac-equivalent impedance model in the frequency domain, and then uses an equivalent network (Z_{ac}) to fit the impedance spectra [43]. This model only works for a constant SOC and temperature setting, and also, the fitting process for this model is complex and non-intuitive, hence it is not commonly used for EV applications.
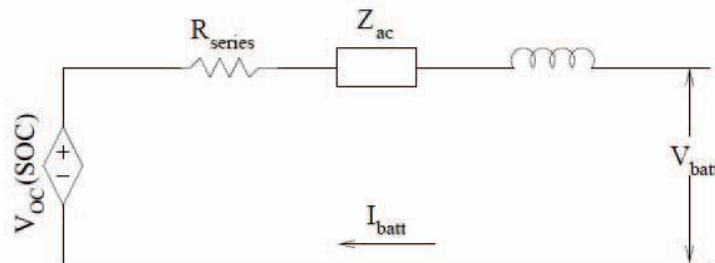
Figure 9. Impedance-based battery model. [44]

2.2.5. Runtime-Based Model

This model comprises of three different parts, as shown in Figure 10. The first part represents the transient behavior of the battery with $R_{transient}$ and $C_{transient}$. The second part consists of V_{lost}, R_{self-}

discharge and $C_{capacity}$, which are the voltage lost due to internal losses, the self-discharge resistance and the total capacity of the battery. The last part characterizes the terminal voltage V_{batt} and SOC of the battery through the internal resistance R_{series} [42]. This model uses a complex circuit network to simulate the battery runtime and behavior under a constant discharge current, but it cannot predict accurately for varying load currents. The required current profile to be drawn for an EV is normally a dynamic one, hence this model would not be desirable for the use in EV applications.
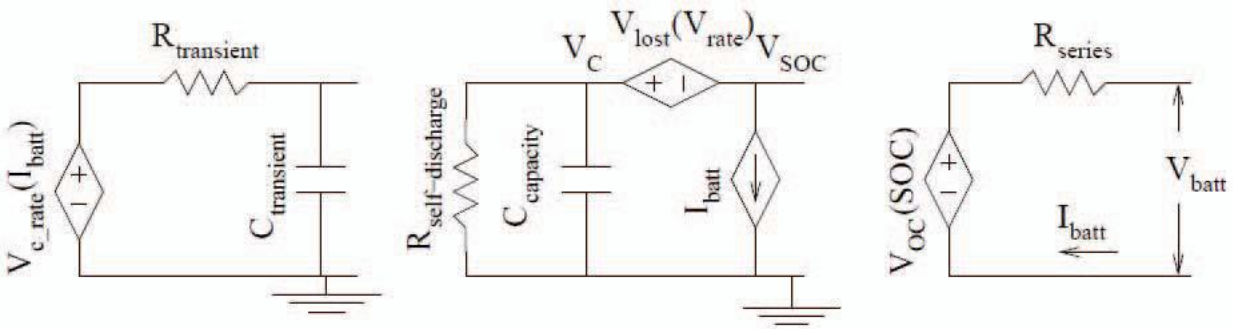
Figure 10. Circuit of runtime-based model. [44]

2.3. Battery Management System

The BMS is an important element to keep EVs safe, reliable and efficient. It not only controls the operational conditions of the battery to prolong its service life and ensure its safety but also provides accurate estimation of the SOC and SOH for the energy management modules in EVs. In order to fulfill these tasks, a BMS has several components and functional requirements to control and monitor the operation of the battery [45].

The design of a BMS is complex and requires some considerations about the application's specific needs, the context of the system, and the characteristics of the cells. From these considerations, a list of requirements can be developed. In general, the BMS component and functional requirements include: acquisition of temperature, voltage and current, data communication between BMS master module and slave modules and between battery pack and surrounding

applications, and other requirements on robustness against electromagnetic interference (EMI), contactors, redundancy of the system in terms of functional safety, galvanic isolation of functional systems, balancing and power consumption, size weight, etc. [46]. The structure of a typical BMS for EV applications is shown in Figure 11. The BMS can monitor different parameters in a battery pack (temperature, voltage, current, capacity, SOH and coolant flow) to determine if any problems arise in the battery and take necessary actions to mitigate the issues [8]. One of the more significant issues is the battery exceeding the operational limits. For example, overcharging can have a very damaging effect on the cells [47]. The BMS is responsible for estimating the battery SOC from measured quantities and preventing overcharging phenomenon based on the SOC estimation [45]. This would require accurate information from the measurements of the battery parameters such as voltage and current.

Figure 11. Structure of a typical BMS for EV applications. [46]

The voltage measurements are done on both cell and pack level. While the cell voltages are just a few volts, the pack voltage can reach over 800V in some applications [48]. Therefore, the BMS
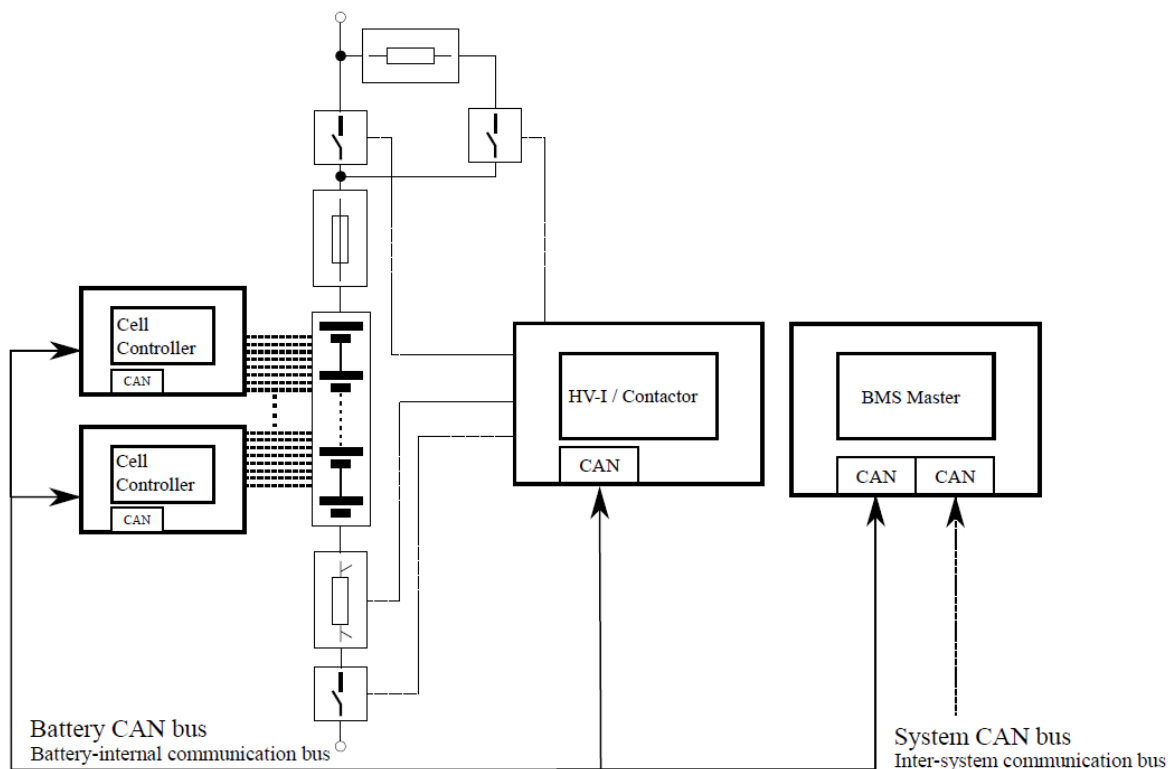
20

needs to distinguish between cell voltage measurement and pack voltage measurement. The sum of the cell voltages must be identical to the total pack voltage, which can be a criterion for fault detection [49]. The acquisition of cell voltages is usually through integrated BMS frontend chips with an absolute accuracy of 1mV and a full range scale of 12 to 16 bits. The better the voltage accuracy, the better the SOC estimation. However, using only voltage data is not sufficient to determine a cell's SOC [46]. Information regarding the current measurements is also needed for accurate SOC estimation.

Current acquisition is important for dynamic SOC determination because a method to estimate SOC is coulomb counting, which simply integrates the current flowing in or out of a battery. This method is only an additional one and does not have sufficient reliability due to the fact that current sensors can undergo drift and offset, otherwise know as faults, but it is still used as reference for other methods [46]. Current acquisition devices can be divided into two sensor technologies, galvanically connected and isolated. An example of the galvanically connected technology is the shunt resistor current sensing, where a low-resistance high-precision resistor combines with a high-precision voltage measurement system to determine the current. An example of the isolated current acquisition is the use of electromagnetic properties of the current to obtain the magnetic field strength with Hall sensors. Based on the Hall effect, when the current flows through the Hall sensor, the sensor creates a voltage that is proportional to the product of magnetic flux density and current [50] [51]. Current sensors, as well as voltage sensors, are very important to the operation of the BMS and battery. However, despite having great accuracy after multiple iterations of improvement in the industry, they are still subjected to having faulty operation, which can lead to inefficient and unsafe operation of the battery, and EV applications in general.

2.4. Battery Faults and BMS Faults

A fault is defined as a deviation of at least one property or parameter of the system from the standard conditions. Faults are commonly classified as actuator faults, sensor faults and component/parameter faults. They can affect the control action from the controller, produce

measurement errors or change the input/output properties of the system, which leads to degradation and damage of the system [52].

There are multiple faults that can be caused by the operation of the battery. Some common faults are overcharging, over-discharging, sulphation, physical damage and short-circuiting. These faults are specifically battery faults caused by electrochemical reasons and can be detected by the BMS to assure minimum damage to the application. However, in order to detect these faults, the BMS measurements from the battery (voltage, current and temperature) need to be reliable. Because the devices used for the measurements are sensors, the BMS are mostly susceptible to sensor faults.

Readings from the sensors in the BMS have an important role in estimating other characteristics of the battery. For instance, as mentioned before, the measurements from voltage and current sensors can affect the estimation of SOC. A ±1mV voltage accuracy system used to calculate SOC in an NMC cell can have a base error of 0.2%. If the same accuracy is used to acquire an LFP cell's SOC, then a base error of 5.9% can be expected for the SOC estimation [46]. Inaccurate SOC estimation can lead to overcharge and over-discharge phenomena as well as undesirable faulty controls of the BMS, which can result in poor performance and fast aging of the battery. It is desirable to avoid these faults by using the highest-performance sensors, but there is still a need for a secondary plan in case the sensors fail to operate correctly. A reliable fault detection and isolation scheme for BMS sensors is required to fulfill this need.

The BMS current and voltage sensors used in EVs application are Hall effect sensors. Therefore, the two main faults can be categorized as bias (offset) and gain (scaling) faults. Bias fault is a constant offset from the sensor signal during normal operation. Gain fault happens when the measurement magnitudes are scaled by a factor while the signal form itself does not change. The faults are considered additive and can be modeled as follows [10]:

$$\tilde{y} = y + f \qquad\qquad (2.3)$$

where $\tilde{y}$ is the measured value of current and voltage from the sensors, y is the actual current or voltage, and f is the sensor fault.

2.5. Sensor FDI Methods in Literature
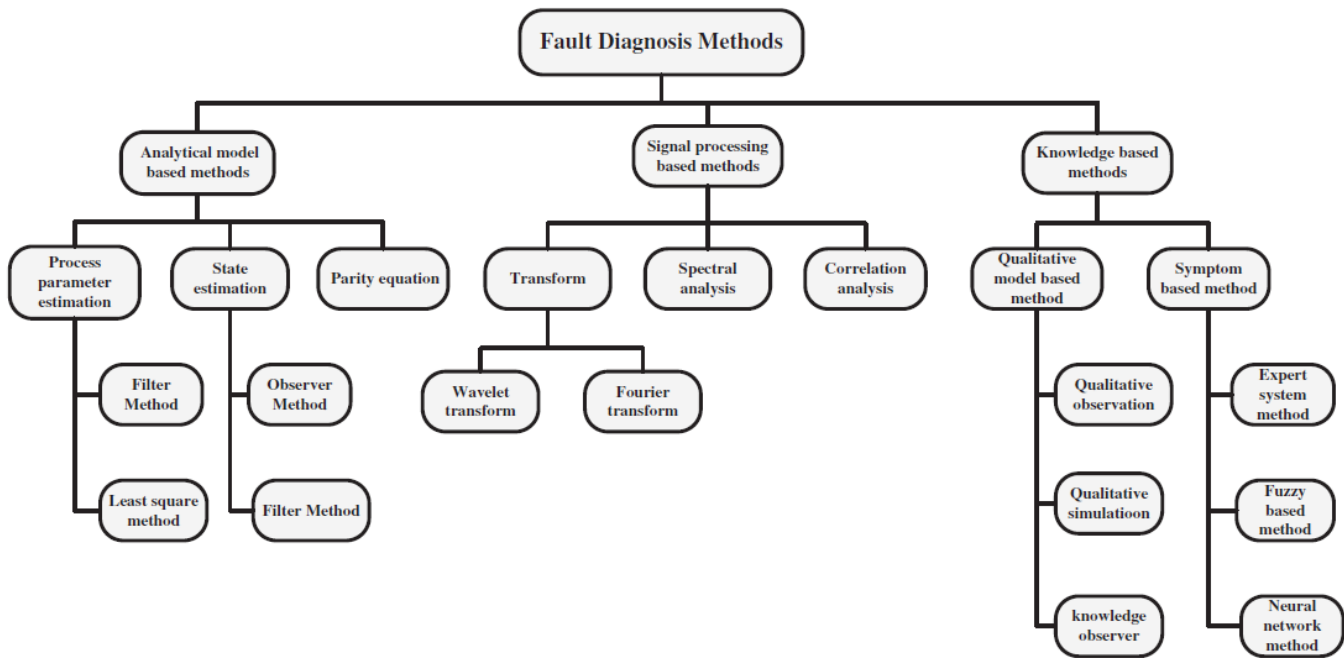
Figure 12. Typical fault diagnosis methods. [11]

There are many FDI schemes used for various applications in different industries, depending on the nature of the application. The main categories for fault detection methods include analytical model-based methods, signal-processing-based methods, and knowledge-based methods, as can be seen in Figure 12. Signal-processing-based methods do not require system modeling, making them simpler to develop while having better dynamic performance. However, the drawbacks of these methods are the inability to detect fault early and hence, the inability to locate faults correctly. Also, the calculation requirement for these methods is always larger compared to model-based methods. Knowledge-based methods are suitable in the case of complicated and nonlinear systems, where developing a system model is a difficult task. They take both experience and knowledge into consideration, which can potentially make them artificially intelligent and highly accurate. However, the training process and rule establishment for these methods are time-consuming and require an immense amount of data in order to be usable. Model-based methods are great for linear system diagnosis, but Li-ion batteries are nonlinear electrochemical systems. These are still the most appropriate methods for fault detection in BMS since they do

not require a great amount of computational effort, and the nonlinear aspect can be resolved using nonlinear theory, adaptive observers and qualitative methods (filters) [11]. Most of the FDI schemes for sensor faults in Li-ion batteries in literature have been model-based methods.

The reviews on sensor fault mechanism and diagnosis approaches for Li-ion batteries can be found in [8] and [11]. Desirable characteristics of a fault detection and isolation (FDI) scheme include quick detection and diagnosis, isolability, robustness, adaptability, low modeling requirements and a reasonable balance between storage and computational requirements [53]. Several existing FDI methods were able to accomplish some of the desired characteristics stated above. An extended Kalman filter was used in [10] to diagnose sensor faults but fault isolation was not achieved. This study confirms that the battery can be over-charged or over-discharged due to sensor faults, caused by the inaccuracy of SOC estimation. In [54], the nonlinear parity equation approach coupled with sliding mode observers were used to develop an FDI scheme to detect sensor faults for a single battery cell. A set of Luenberger and learning observers were used in [55] for simultaneous single-fault isolation and estimation of a faulty cell in a battery string. In [56], an FDI strategy using structural analysis theory and statistical inference residual evaluation was presented, but the computational effort was rather high, hence, not appropriate for a real-time application like the BMS. An FDI scheme using sliding mode observers with equivalent output error injection was introduced in [57], with findings that false detection rate is affected by variation in model parameters. This means that if the model parameters change, the FDI scheme will become unreliable. All of the methods in current literature are forms of state observers, and require the knowledge of battery parameters, which can be affected by degradation, a significant property of battery operation. These FDI schemes operate under the assumption that the model parameters do not change, which is untrue with the constant occurrence of degradation. There has not been any mention of cell degradation in any FDI works done in literature, hence, all of the FDI schemes mentioned above will become unreliable at some point of the battery operation, when the parameters have changed enough due to degradation and started to affect the state observers. Given the nature of EV applications, degradation of Li-ion batteries is inevitable, and it is impossible to perform characterization of the battery to obtain updated values for model parameters once the pack is in the vehicle. Therefore, it is necessary

to develop and implement an FDI scheme that can decouple and isolate the effect of fault and degradation during battery operation to make the BMS sensor fault diagnosis more reliable.

2.6. Online Parameter Estimation Methods for Fault Diagnosis

The battery system is one that many have looked at and researched to understand extensively, which is why there are many models to describe its behaviors during operation and rest. Because the battery models are readily available, with some being very simple but reliable for the purpose of monitoring, the fittest BMS sensor fault diagnosis strategy is model-based. This can be seen in previous literature publications shown in the previous section. However, all of the existing FDI methods use state estimation and not parameter estimation. It can be seen that with the inevitable occurrence of degradation, state estimation is not a suitable method, as it requires knowledge of the process parameters and assumes them to be constant. After some investigation into the literature, it can be determined that the use of the parameter estimation method for BMS sensor fault diagnosis has not been thoroughly researched in any work.

Online parameter estimation method for fault diagnosis is the diagnosis of any parameter drifts when the system is operating in real-time. It requires accurate parametric models of the process and assumes the process parameters to be either constants or dependent only on state variables [58]. For example, in the case of the BMS using the Thevenin based model, the parameters are dependent on the current and voltage of the battery the most. Other state variables that can affect the parameters are temperature and SOC, but to a lesser degree. Degradation is also known to affect the parameters and needs to be filtered out by some means. Therefore, if there are any abrupt changes in the measurements of current and voltage (caused by faulty operation of the sensors), they should reflect on the estimated values of the parameters and fault detection would be made available then.

The procedure for parameter estimation methods is outlined below:

$$y(t) = f(u(t), \theta) \tag{2.4}$$

25

The model parameters θ are estimated from the measurements y(t) and u(t). Changes in the parameters are then computed. Using methods of pattern recognition, these changes can be related to process faults. There are some common parameter estimation techniques such as least squares, instrumental variables and estimation via discrete-time models [59]. Recursive least squares method is one that has been suggested and used in many BMS algorithms in literature, for the purpose of estimating parameters and SOC online. Since the estimation is a time series, instead of a residual generation (prediction versus measurement) method, the fault would have to be detected using a change point detection method.

2.7. Change Point Detection Methods

A change point is defined as an abrupt variation in time series data. Time series data are sequences of measurements over time describing the behavior of systems [60]. These behaviors can change due to external events and/or internal systematic changes [61]. The purpose of change point detection (CPD) is to find abrupt changes in data when a property of the time series has changed [62].

CPD algorithms are often categorized as online or offline. Offline algorithms analyze the entire data set at once, in batch mode, and identify where the change occurred. These are often used in climate change analysis or medical condition monitoring. Online, or real-time, algorithms can detect change while running concurrently with the monitored process. They process each data point as it becomes available and aim to detect the change point when the system change occurs [63]. From a practical standpoint, it is impossible to perfectly detect changes in real-time because of the complexity of most applications. There is a lag for any CPD algorithms, but the goal is always to minimize this lag.

There are two types of online CPD algorithms, supervised and unsupervised. Supervised methods require a sufficient amount of training data, essentially machine learning algorithms. Unsupervised methods include likelihood ratio methods, subspace models, probabilistic methods, clustering, and graph-based method. These are used depending on the application and

the nature of the system. Subspace model, cumulative sum control chart (CUSUM) and clustering methods are common CPD algorithms, but they do not exhibit good performance for noisy data or highly dynamic systems [60]. One possible solution is to smooth the time series out before implementing a CPD method, using a low pass filter such as a weighted moving average (WMA) filter.

2.8. Drive Cycles

A drive cycle is a set of data that represents an actual driving situation by plotting vehicle speed versus time. Drive cycles are normally produced in order to assess the performance of the vehicles regarding several metrics, including fuel consumption and emissions [64]. The Environmental Protection Agency (EPA) uses different types of drive cycles for different vehicles and scenarios, varying in duration, distance and speed profile. Some common drive cycles run by the US EPA are the Urban Dynamometer Driving Schedule (UDDS), the Highway Fuel Economy Test (HWFET), the Federal Test Procedure (FTP), and the Inspection and Maintenance Driving Schedule (IM240) [65].
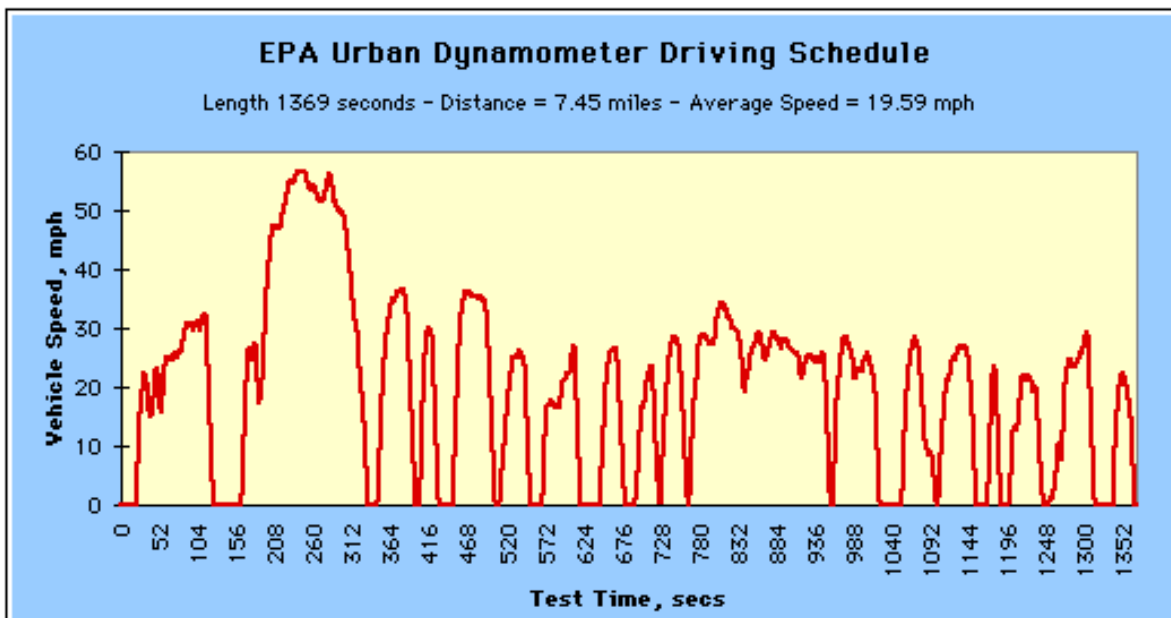

Figure 13. The Urban Dynamometer Driving Schedule speed profile. [65]

Drive cycles are also often used in vehicle simulations. The data obtained from simulating drive cycles in vehicles can lead to meaningful findings for the powertrain components such as the battery pack. Battery operation in EVs can be simulated and observed when a vehicle is running a drive cycle. This is more cost-effective and less time-consuming for experimental testing of batteries. The drive cycle can also be translated into a current profile, which can then be used to run a separate laboratory test for a specific cell instead of obtaining measured data from a pack in the vehicle.

The EPA UDDS is commonly called the "LA4" or "the city test" and represents city driving conditions. It is used for light-duty vehicle testing [64]. The speed profile of the UDDS drive cycle is shown in Figure 13 above. It is the most common drive cycle in battery simulation and testing.

2.9. Cell Characterization

Cell characterization is a very important step in battery testing because it helps researchers to understand how a particular cell behaves in certain conditions and predict its behavior in another simulated condition. Simulation of cell operation is necessary due to the fact that some experiments can be unrealistic to conduct because of cost, time and/or physical constraints. Cell characterization includes three main tests: capacity test, SOC-OCV curve construction, and Hybrid Pulse Power Characterization (HPPC) test to determine battery model parameters [66].

There are various types of battery testing equipment. One that is commonly used is from the manufacturer Maccor. The Maccor equipment can charge and discharge the battery using different current and voltage profiles, and measure and record various battery metrics during the runs. The data obtained from the Maccor equipment is often reliable and can be used to determine the battery parameters and also to simulate the battery performance. Figure 14 shows an example of the Maccor 4200.
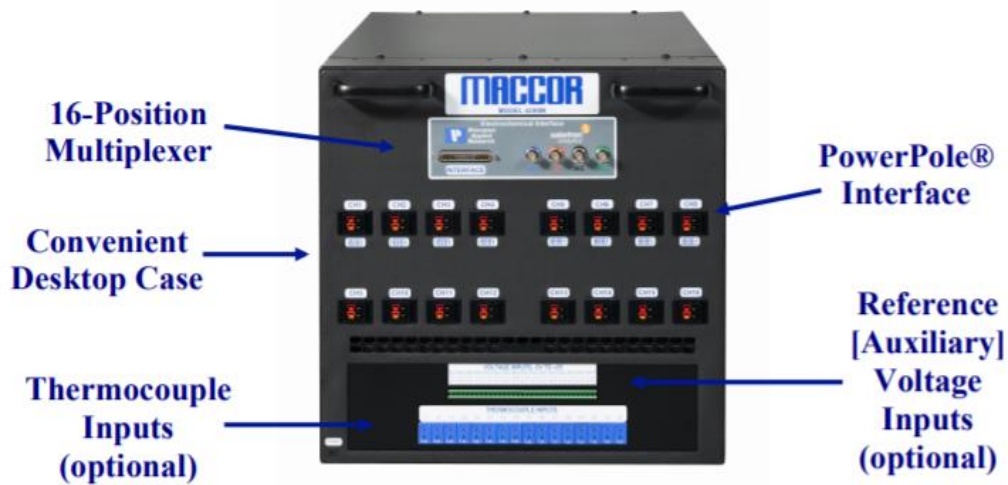
Figure 14. The Maccor 4200. [67]

The capacity test is carried out by discharging the cell at a constant current, at a user-selected C-rate (normally ranged from 0.5 to 2), until the cell reaches its upper voltage limit. Then, the cell is discharged at a constant voltage (the upper limit), until the current reaches a relatively small value, close to 0. The process is repeated for charging [68]. The capacity test should be conducted multiple times for a cell to obtain a reliable value for its capacity. Figure 15 shows the current, voltage and capacity profiles for the charging portion of the capacity test. The capacity then is calculated from the data obtained as follow:

$$Q = I * \Delta t \tag{2.5}$$

where Q is the charge or capacity in coulombs (1 Ah = 3600 Coulombs), I is the current in A and t is the time in seconds.
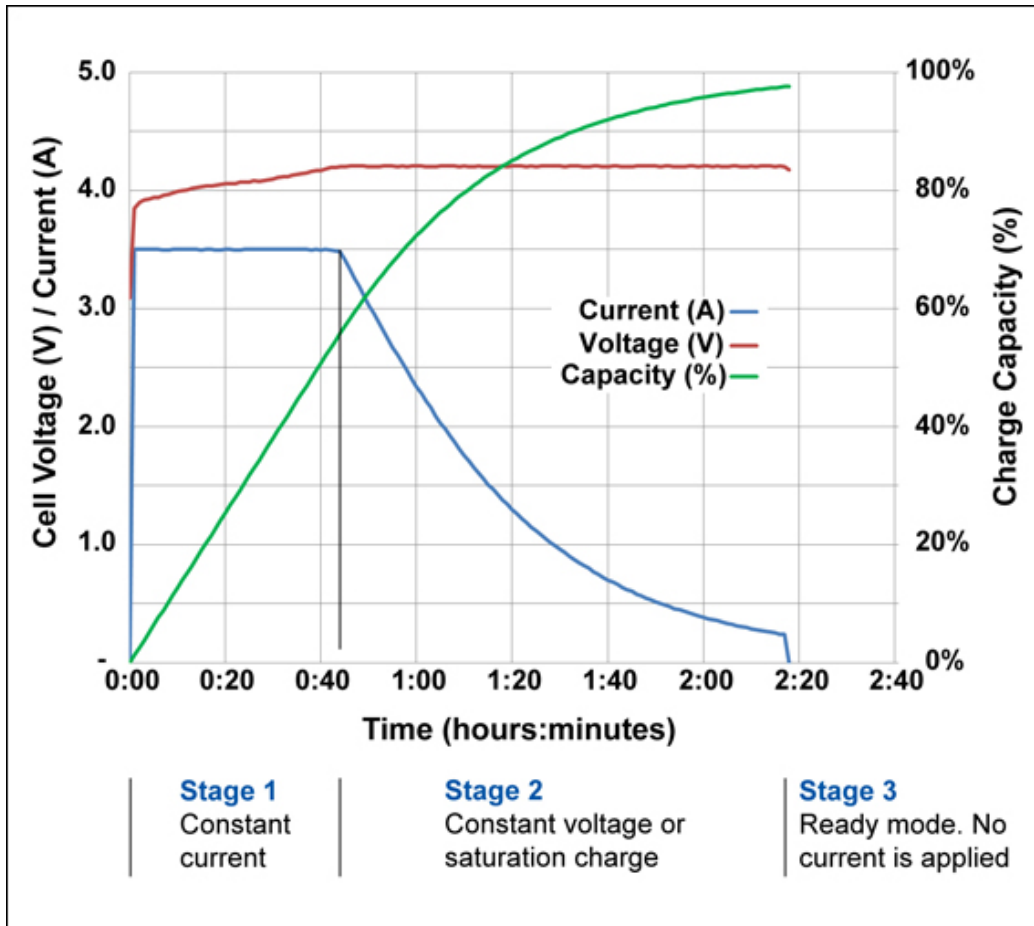
Figure 15. Current, voltage, capacity profiles for the charging portion of the capacity test. [69]

For the construction of the SOC-OCV curve, a constant discharge of C/25 rate is performed on the cell, running from the upper voltage limit to the lower voltage limit of the cell. At the beginning and end of the SOC range, the discharge rate should be C/50 rate for a more refined curve, because the OCV often changes drastically at the extremes of the SOC. The process is repeated for the charging of the cell. SOC can be calculated as the ratio of the remaining useful capacity over the initial capacity of the cell at full charge. The OCV is the average of all the measured voltages at each SOC, normally in the SOC interval of 0.01. Figure 16 shows an example of an SOC-OCV curve for an NMC cell. This experiment should be repeated multiple times in order to obtain the average values for the OCV at different SOC so that the curve is more reliable.
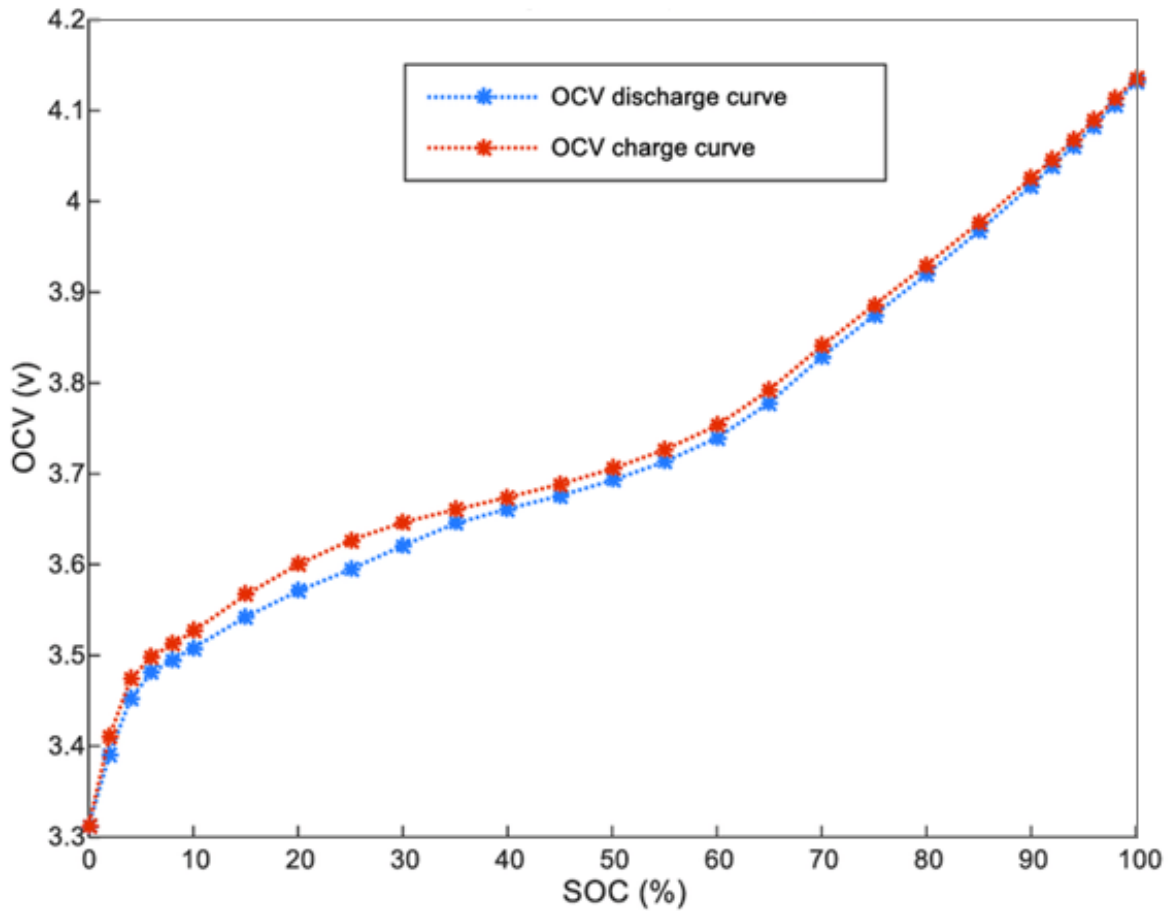
Figure 16. SOC-OCV curve for an NMC cell.

The HPPC test is used to determine dynamic power capability within the cell's usable voltage range. Its profile includes both discharge and charge pulses. The data obtained from this test can be used to derive performance characteristics such as peak power and available energy. This test can also help with determining the voltage response curves, from which the ohmic (fixed) cell resistance and cell polarization resistance as a function of SOC (or capacity) can be obtained. These are parameters in some battery models, such as the Thevenin based model.

The pulse profile includes a discharge pulse for 10 seconds, followed by a rest period of 40 seconds, then a 10-second charge pulse. The pulses can range from C/3 to 3C rate, depending on the purpose of the experiment. The entire HPPC test is made up of single repetitions of this pulse profile, followed by discharge to the next 10% increment of the SOC. The SOC can be calculated from the fully charged cell capacity (determined from the capacity test) and the remaining capacity (calculated using coulombs counting of the cell in operation). An hour of resting period is standard between each 10% SOC interval [68]. The HPPC test is run within the range of voltage limits specified by the cell manufacturer. An example of an HPPC test with 2 pulse profiles is shown in Figure 17.
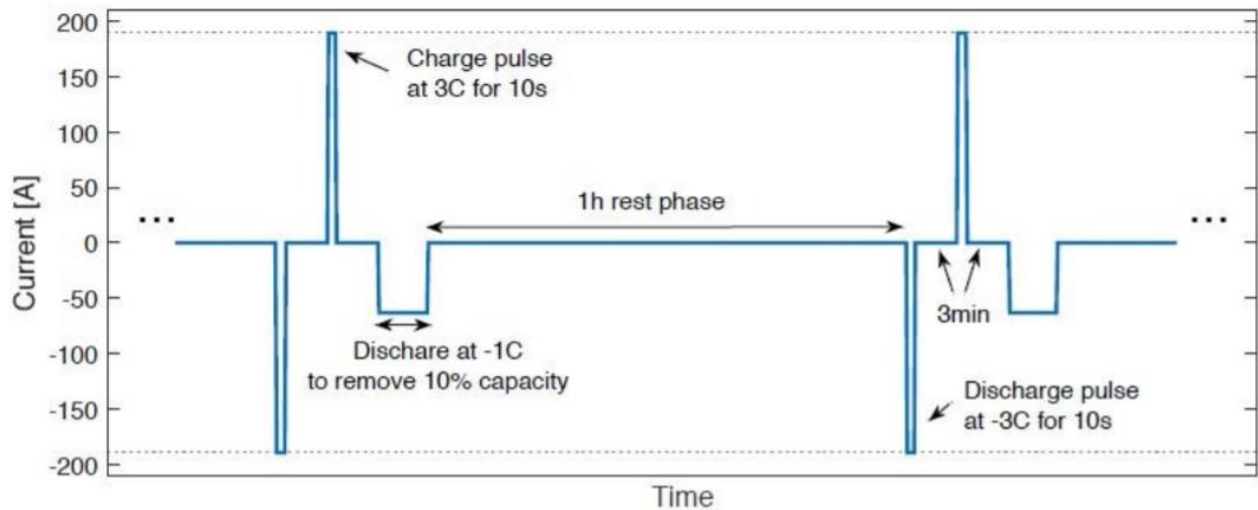
Figure 17. Current profile for 2 pulses in HPPC test. [68]

3. Proposed FDI Algorithm

3.1. Battery Model

The most common model used to describe battery behaviors in EVs application is the equivalent circuit model. For an LFP battery running drive cycles that are highly dynamic such as UDDS, an ECM with at least two RC pairs is recommended [45]. This is because the first order ECM neglects the effect of diffusion. However, the higher the model order is, the more computational effort it demands, due to the larger number of model parameters. For the implementation of the proposed FDI, it is not required for the model to have great accuracy, since the extraction of ECM parameters is used to monitor the state of battery operation, rather than to model the battery performance. Therefore, in order to optimize the computational complexity of the approach, the first order ECM is used in this thesis. The simplified ECM model is shown in Figure 18.
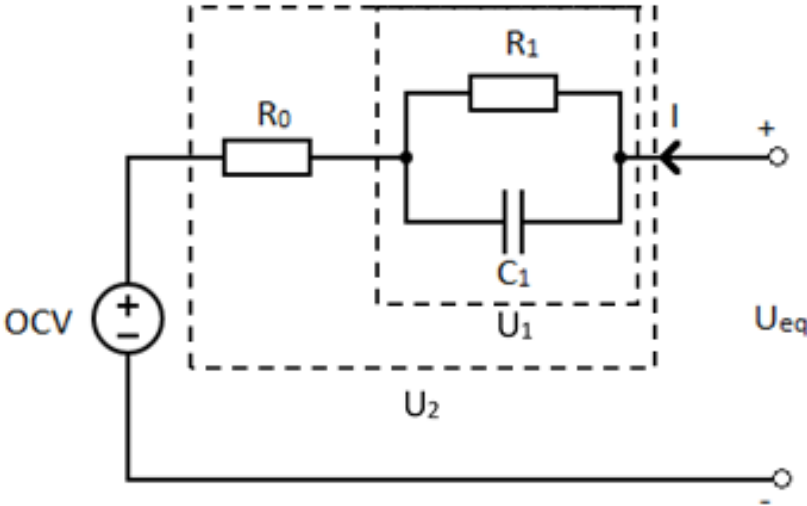
Figure 18. Schematic of a first-order ECM.

The state-space equation of this battery model can be expressed as follows:

$$\dot{U}_1 = \frac{I}{C_1} - \frac{U_1}{C_1 R_1}$$

(3.1)

$$U_{eq} = OCV - U_1 - IR_0$$

In order to perform the proposed recursive approach on the model, an autoregressive exogenous model is needed. This is done through obtaining the transfer function of the battery impedance from Equation (3.1) in the s-domain, as shown in Equation (3.2). The transfer function is then discretized using the basic forward Euler transformation method, in which s is replaced by $\frac{1-z^{-1}}{T.z^{-1}}$ where T is the sampling time. The discretization is shown in Equation (3.3) below.

$$G(s) = \frac{U_2(s)}{I(s)} = -R_0 - \frac{R_1}{1 + sR_1 C_1}$$

(3.2)

$$G(z) = \frac{a_2 + a_3 z^{-1}}{1 + a_1 z^{-1}}$$

(3.3)

where

$$a_1 = \frac{T}{R_1 C_1} - 1$$

(3.4)

$$a_2 = -R_0$$

(3.5)

$$a_3 = R_0 - \frac{T}{C_1} - \frac{TR_0}{R_1 C_1}$$

(3.6)

R1 and C1 can be determined as follows:

$$R_1 = \frac{a_1 a_2 - a_3}{1 + a_1}$$

(3.7)

$$C_1 = \frac{T}{a_1 a_2 - a_3}$$

(3.8)

The autoregressive exogenous model then can be obtained as follows:

$$y_k = OCV_k + a_1(OCV_{k-1} - y_{k-1}) + I_k a_2 + I_{k-1} a_3 \qquad (3.9)$$

with y_k, which can be rewritten as:

$$y_k = \theta_k^T \phi_k \qquad (3.10)$$

where

$$\theta_k = [1; \ a_{1,k}; \ a_{2,k}; \ a_{3,k}] \qquad (3.11)$$

$$\phi_k = [OCV_k; \ (OCV_{k-1} - y_{k-1}); \ I_k; \ I_{k-1}] \qquad (3.12)$$

The values for OCV in Equation (3.12) will be determined from the OCV-SOC relationship. The OCV-SOC curve will be obtained experimentally. The SOC is normally estimated by the BMS, and the OCV will be determined from the SOC value and the established OCV-SOC curve, simply through a look-up table. This reduces the computational effort for θ_k, which gives more accurate ECM parameter estimations. Equations (3.10-12) will be used in the proposed RLS algorithm, and Equations (3.5), (3.7) and (3.8) will be used to extract the ECM parameters for the purpose of fault diagnosis.

3.2. Recursive Least Squares Algorithm

The RLS algorithm used in this thesis employs an optimal forgetting factor to give more weight to recent data, avoiding the saturation phenomenon [70]. The forgetting factor is applied to the parameter vector θ_k. The recursive algorithm of Equation (3.10) can be represented as follows:

$$K_k = \frac{P_{k-1}\phi_k}{\lambda + \phi_k^T P_{k-1}\phi_k} \qquad (3.13)$$

$$P_k = \frac{P_{k-1} - K_k \phi_k^T P_{k-1}}{\lambda} \tag{3.14}$$

$$\hat{\theta}_k = \hat{\theta}_{k-1} + K_k(y_k - \hat{\theta}_{k-1}^T \phi_k) \tag{3.15}$$

where $\hat{\theta}_k$ is the estimated parameter vector θ_k, K_k is the algorithm gain, P_k is the covariance matrix and λ is the forgetting factor, which is normally in the range of [0.95, 1] and will be tuned later to give optimal results. The values of θ_0 and P_0 are initially guessed. The schematic diagram for the RLS algorithm is shown in Figure 19.
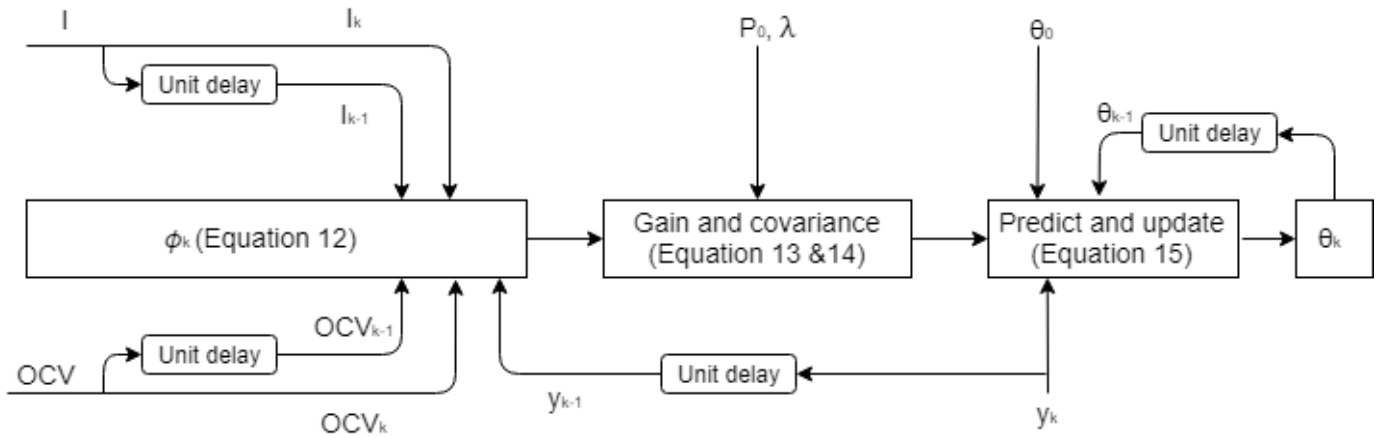
Figure 19. Schematic diagram of the RLS algorithm.

3.3. Weighted Moving Average Filter

WMA is a low-pass filter that is used for smoothing fluctuations, such as noise, in a time series to allow for more reliable trend analysis. Additionally, one can use WMA to compute short-term forecasts of time series [71]. The RLS-estimated ECM parameters are time series that contain noise and small fluctuations due to operational conditions (SOC and temperature) and degradation of the cells. A fault, however, is expected to affect the parameters more significantly. Therefore, the difference between WMA-filtered and unfiltered values of the ECM parameters during normal operation of the battery should be considerably smaller than when a fault first

occurs. The WMA chosen for the proposed FDI is a two-term WMA to minimize storage requirements. The formula is presented in Equation (3.17).

$$P_{f,k} = \lambda_{WMA}P_{i,k} + (1 - \lambda_{WMA})P_{f,k-1} \tag{3.17}$$

where $P_{f,k}$ is the kth WMA value, $P_{i,k}$ is the kth unfiltered value obtained from RLS (P represents R_0, R_1 and C_1) and λ_{WMA} is the weighting factor. The discrepancy between $P_{f,k}$ and $P_{i,k}$ is characterized by an absolute fractional error term, as shown in Equation (3.18).

$$e(P_k) = \left| \frac{P_{i,k} - P_{f,k}}{P_{f,k}} \right| \tag{3.18}$$

3.4. Cumulative Sum Control Chart

The error is monitored using CUSUM, a common change-point detection algorithm, which accumulates deviations of data and signals when the cumulative sum exceeds a certain threshold. The algorithm is outlined in Equation (3.19) below [72]:

$$S(e(P_k)) = \max\{0, S(e(P_{k-1})) + e(P_k) - (\mu_0 - L\sigma)\} \tag{3.19}$$

where S is the cumulative sum value, $S(e(P_0)) = 0$, e is the absolute fractional error from Equation (3.18), μ_0 and σ are the mean and standard deviation of the error population, and L is a specified constant.

In this thesis, the λ_{WMA} value from Equation (3.17) is set to 0.01, since it is more favorable for the filter to obtain a smooth line which can adapt to minor changes over a long period of time, such as noise or degradation effect. In Equation (3.19), the expected value for μ_0 is 0 and σ is estimated experimentally (0.0001 for R_0, 0.005 for R_1 and 0.005 for C_1). During normal operation, the unfiltered values should not deviate from the smooth filtered line, because the amplitude of those fluctuations (noises due to changes in SOC, temperature, or degradation) is not significant. When a fault occurs, the unfiltered values would diverge significantly from the

smooth filtered series. The CUSUM algorithm detects this divergence by indicating a fault $(F(P_k) = 1)$ when $S(e(P_k))$ exceeds an experimentally calibrated threshold J, as shown in Equation (3.20).

$$F(P_k) = \begin{cases} 1 \ \ if \ S(e(P_k)) > J \\ 0 \ if \ S(e(P_k)) < J \end{cases} \qquad (3.20)$$

3.5. Fault Isolation

The method outlined in this chapter, summarized in Figure 20 (P_k represents the parameters), can only be used for fault detection, not fault isolation. The full proposed FDI scheme will be shown in Section 4.8, after determining the effects of different sensor faults on the ECM parameters. Since there has not been any work done in literature to determine fault effects on the parameters, some experiments will need to be performed to obtain this data before completing the full FDI scheme. Preliminary experiments done for this thesis showed that the fault isolation can be achieved based on the fault detection (response) time of the parameters when a certain fault occurs (each parameter is sensitive to a certain fault); this will be confirmed in the next chapter.
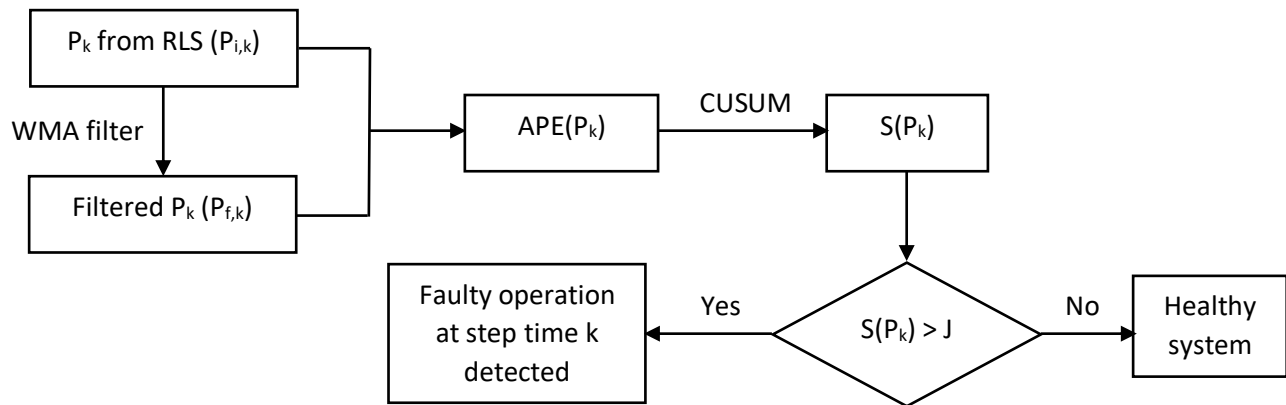

Figure 20. Fault detection schematic not including fault isolation.

4. Experimental and Results

4.1. Purpose of Experiments

There is a number of experiments that need to be run in order to characterize the battery cell, observe the effect of degradation on the cell and determine the effect of sensor faults on the ECM parameters to establish the completed FDI scheme. The data obtained from the experiments can also be used for fault simulation and fault diagnosis validation. The experiments include cell characterization tests (capacity, OCV-SOC, and HPPC), UDDS simulation runs and cell degradation runs.

The cell characterization gives information about the cell capacity, OCV-SOC curve, and cell parameters using HPPC. The capacity indicates the SOH of the cell, with which cell degradation can be observed. The OCV-SOC curve can be used to create a look-up table, matching the OCV to the SOC in an interval of 1%. This is used to estimate the OCV in the RLS algorithm to increase the accuracy of the parameter estimation. The HPPC test is done to obtain the cell model parameters. The results show the effect of degradation on the parameters, and are also used to confirm the inaccuracy of state observer FDI methods when degradation occurs.

The UDDS simulation runs mimic the current profile that the cell would experience in an EV running a UDDS drive cycle. This run consists of 32 consecutive UDDS drive cycles, lasting a total of 43,808 seconds (approximately 12 hours). The results from this run give the cell voltage profile corresponding to the input current profile. The data obtained from this can be used to estimate the ECM parameters using RLS in order to observe how the parameters of an operating cell are affected by degradation as well as sensor faults. This data can also be used to simulate sensor faults because it is unrealistic to create and control sensor faults in real life. Finally, it can be used to validate the performance of the proposed FDI scheme. After the sensor fault is injected (in simulation), the series of data is run through the fault diagnosis algorithm to see if and when the fault is detected and isolated.

The cell degradation run is essentially the complete charge and discharge of the cell, being repeated multiple times for a long duration. This run normally lasts for approximately 5 days, and

the cell capacity test is conducted after every degradation run in order to confirm cell degradation. The purpose of the degradation run is to expedite the progress of cell degradation. The details of the test sequence for all the experiments will be outlined in Section 4.2, along with the laboratory setup. The current profiles for UDDS and degradation runs will be shown in Section 4.3.

4.2. Experimental Setup and Sequence

For the experiments, graphite/LiFePO$_4$ (LFP) cells produced by A123 Systems, which are designed for power-type applications, were used. LFP cells have a theoretical capacity of 170mAh/g and a redox potential of around 3.43 V with the Li electrode. LFP is commonly used as a cathode material because it has a high thermal stability which makes it safe, a low toxicity, and a low cost compared to cathodes such as LiCoO$_2$. The salt used for the electrolyte is LiPF$_6$, but the solvent solution was not determined. The specifications of the cell at its initial state are listed in Table 1.

Table 1. LFP cell specifications.

Cell dimension (mm)	7.25 x 160 x 227
Cell weight (g)	496
Nominal cell capacity (Ah)	19
Nominal cell voltage (V)	3.3
Voltage limit (V)	2.0 – 3.65
Operating temperature (°C)	-30 to 55

The experimental setup consists of a battery test system (Maccor 4200), connected to a testing station and a computer. The test components are shown in Figure 21. The cell is connected to the Maccor. There are two thick wires connected to the positive and negative terminal of the cell in order to charge and discharge the cell. The charge and discharge current profile can be set up

on the computer software for Maccor. There are also two thin wires connected to the cell, serving the purpose of measuring the voltage of the cell. Run settings and controls are done with computer software. Other battery characteristics such as capacity and energy are calculated in the software, and presented in the data along with time, voltage and current. All experiments were carried out at a room temperature of 23°C. The current is assumed to be positive when discharging and negative when charging. The data was collected at a frequency of 1 Hz and then stored in the computer.
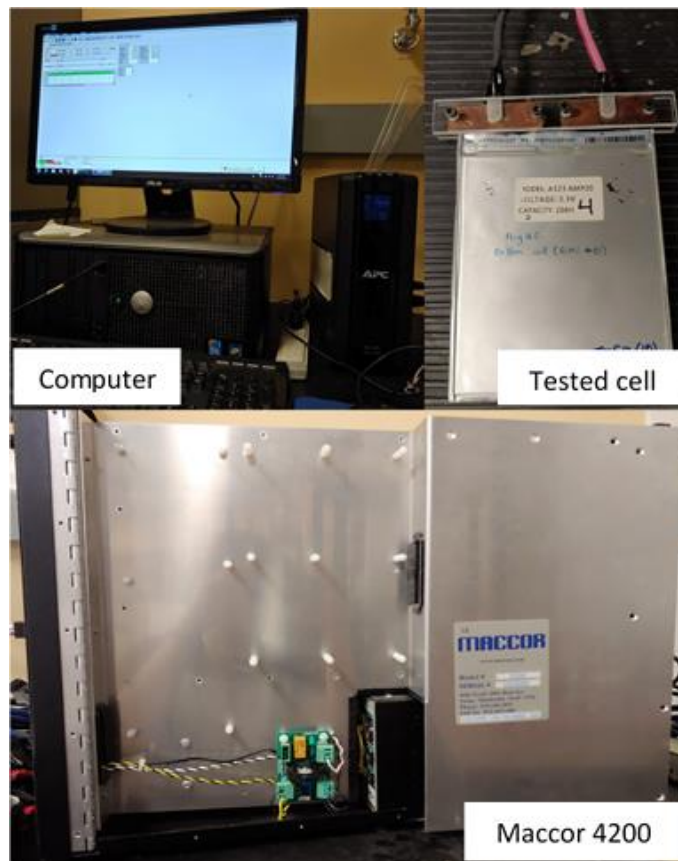
Figure 21. Experimental setup.

The experimental sequence begins with all three cell characterization tests. The OCV-SOC test only needs to be carried out once because the curve does not change significantly within the planned cell degradation range (only down to 80% initial capacity). The HPPC will be conducted twice, at different capacities, only to confirm the accuracy of the RLS algorithm and show how state observer FDI methods become unreliable when degradation occurs. The capacity tests need

to be performed after every degradation run, in order to confirm that the cell has degraded and quantify the degradation progress [13]. After the initial cell characterization, the main testing cycle, including UDDS (12 hours) and degradation (5 days), is run and repeated multiple times, with the capacity test being performed in between each cycle. The test procedure is shown in Appendix A.

4.3. Current Profiles

The profiles for the three cell characterization tests were outlined in Section 2.9. The two test profiles in the main testing cycle (the UDDS drive cycle and the degradation cycle) are shown in Figures 22 and 23. The degradation cycle simply consists of charging and discharging multiple times between the extreme limits of the cell to degrade it quickly. The UDDS drive cycle was translated and scaled into a current profile using a powertrain model in Simulink. It was run from the cell SOC of 100% to 20%. The powertrain model is from a built-in blockset in Simulink. The battery component was changed to consist of the LFP cells being tested, with the configuration of 80S1P. Battery model parameters from HPPC were input into the battery model in the powertrain. The powertrain was then simulated in Simulink to run a UDDS drive cycle and the current profile was obtained for the pack, and ultimately scaled down for a single cell.
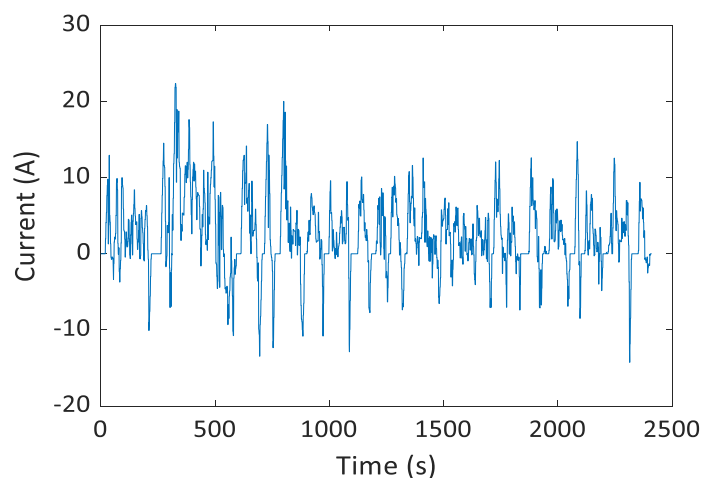

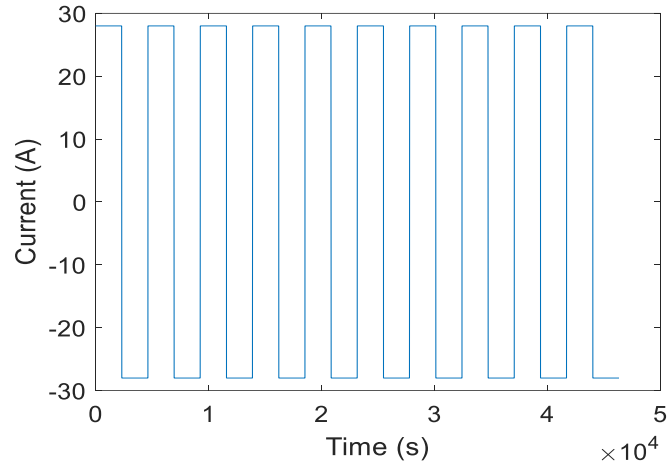**Figure 22. UDDS drive cycle current profile.**

Figure 23. Degradation cycle current profile.

4.4. Cell Characterization Results

As mentioned before, the cell capacity was captured at the beginning of each testing cycle and it best represents the cell degradation, since capacity decreases with degradation [13]. A total of 8 main cycles were conducted, hence there are 8 different cell capacity values captured. The capacity results are presented in Table 2.

Table 2. Initial cell capacity for each test cycle.

Cycle	1	2	3	4
Capacity (Ah)	18.26	18.01	17.84	17.66
Cycle	5	6	7	8
Capacity (Ah)	17.32	16.93	16.61	16.47

The OCV-SOC relationship was also established and a look-up table was built, which is used to estimate the cell OCV for the RLS algorithm. The OCV-SOC curve is assumed to change minimally with cell degradation going from 100% down to 80% of the initial capacity, hence only one curve

43

is used for all cell capacities in the RLS algorithm. The results can be seen in Figure 24. The look-up table is shown in Appendix B.
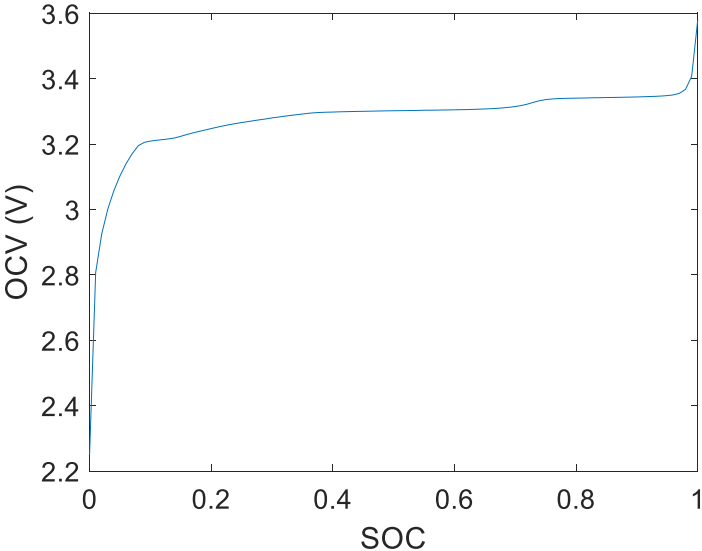
Figure 24. Experimental result for OCV-SOC relationship.
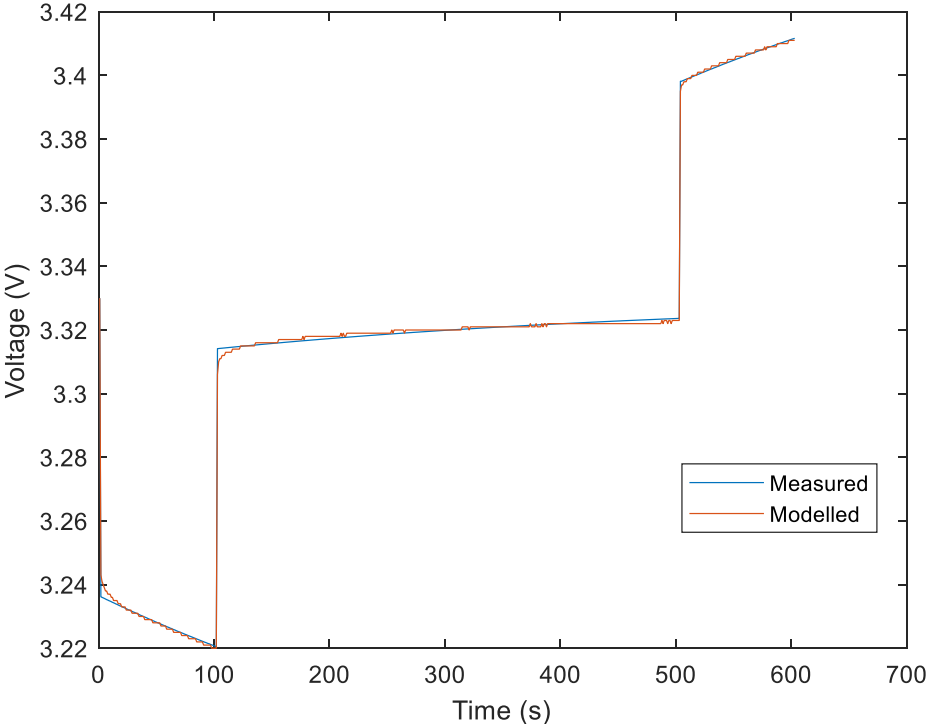
Figure 25. Fitting of one HPPC charge/discharge pulse at 80% SOC at capacity 16.22 Ah.

The HPPC test was performed at cell capacity of 17.51 Ah and 16.22 Ah. The data was analyzed using MATLAB scripts, specifically the "nlinfit" built-in function, which are shown in Appendix C, in order to obtain the first-order ECM parameters at different SOC levels (from 10% to 90%). An example fitting plot is shown in Figure 25. All fitting efforts resulted in errors of less than 0.02%. The results are shown in Figure 26 (a), (b), (c).

(a)

(b)

(c)
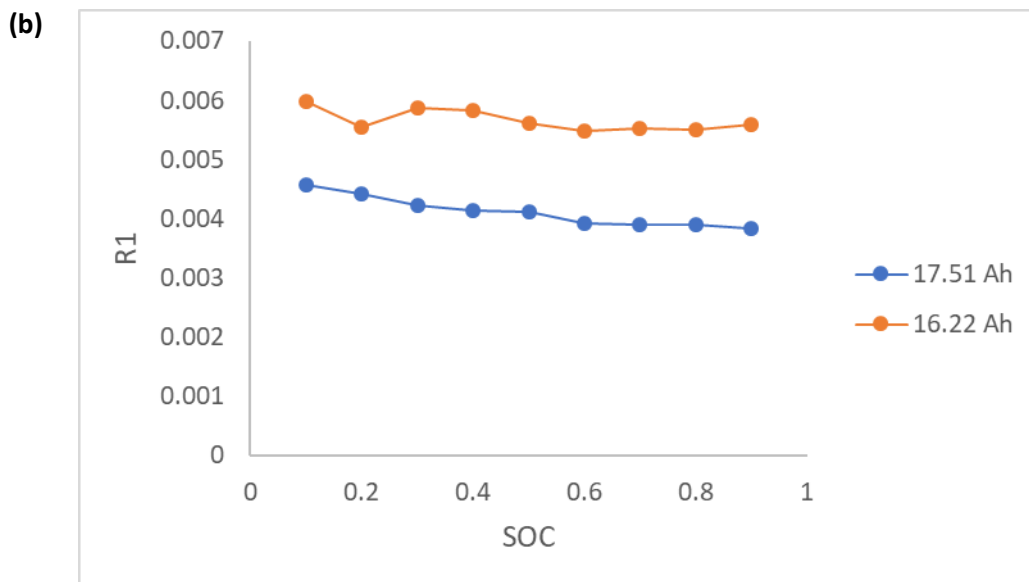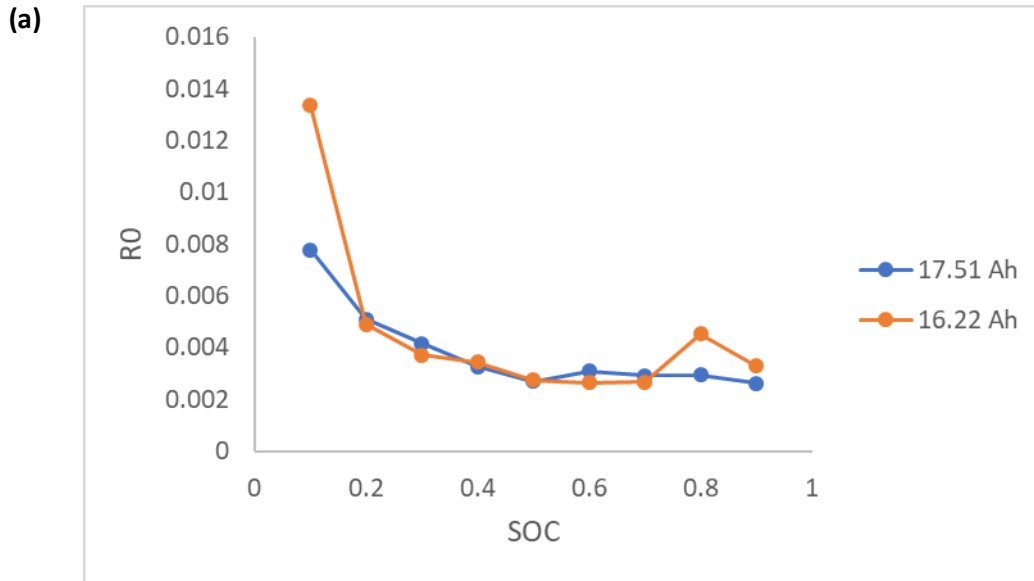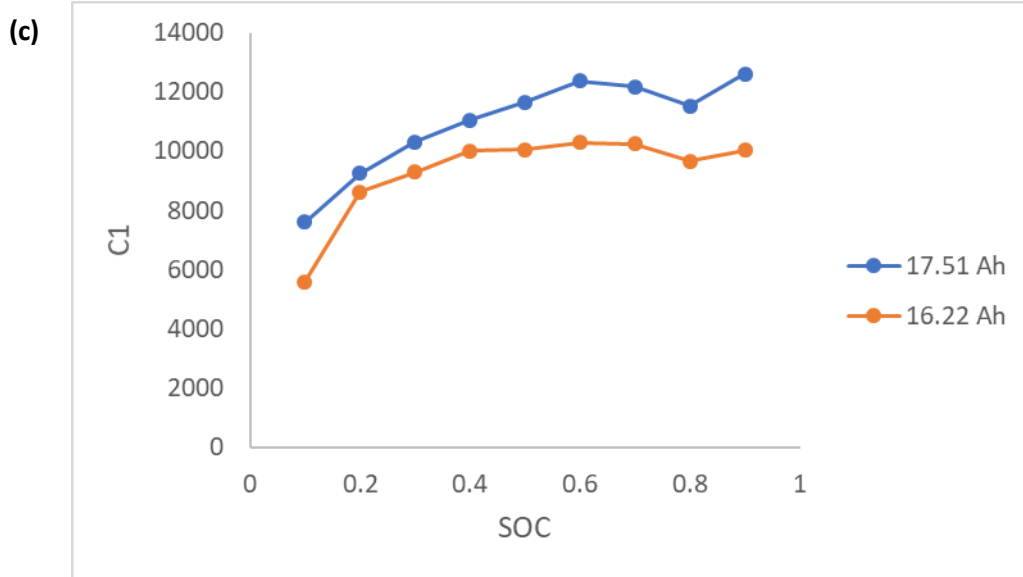
Figure 26. Parameter fitting results from HPPC test. (a) R_0; (b) R_1; (c) C_1.

The results from the HPPC test confirm that the ECM parameters are affected by the capacity of the cell, or ultimately by cell degradation. It can be observed that R_0 does not show any clear trend, but R_1 can be seen to increase with capacity decreasing while C_1 decreases. This will be discussed further in Section 4.6.

4.5. Effect of Degradation on State Observer FDI Schemes

The parameters used in state observer FDI schemes are normally obtained through HPPC results, as can be seen in [9] and [10]. The HPPC test is usually run when the battery is at its initial state, and then the parameters are input into the state observer FDI algorithms, where they are used to calculate the voltage from the battery current. The predicted voltage is then compared with the measured voltage, with filters such as Kalman filters, and any discrepancy after that would signify a fault. This type of FDI scheme is only reliable under the assumption that the parameters remain constant throughout the life of the battery. At a later stage in the battery life, the predicted voltage value will deviate significantly from the measured voltage because the model parameters are no longer accurate.

An example is shown in Figure 27, presenting the comparison between measured voltage and predicted voltages using appropriate and inappropriate (fixed initial) parameters. As can be seen in Figure 27 (b), using parameters at the corresponding cell capacity leads to more accurate voltage estimation compared to using parameters at higher cell capacity. The mean absolute percent error when using parameters estimated at 16.22 Ah is 0.5%, while the mean absolute percent error when using parameters estimated at 17.51 Ah is 0.7%. It can be concluded that using fixed initial parameter values will eventually lead to false fault detection in the state observer methods, since the faults are detected from the deviation between the measured and predicted voltage. Therefore, existing state observer FDI schemes are not reliable when the battery undergoes the process of degradation.

(a)
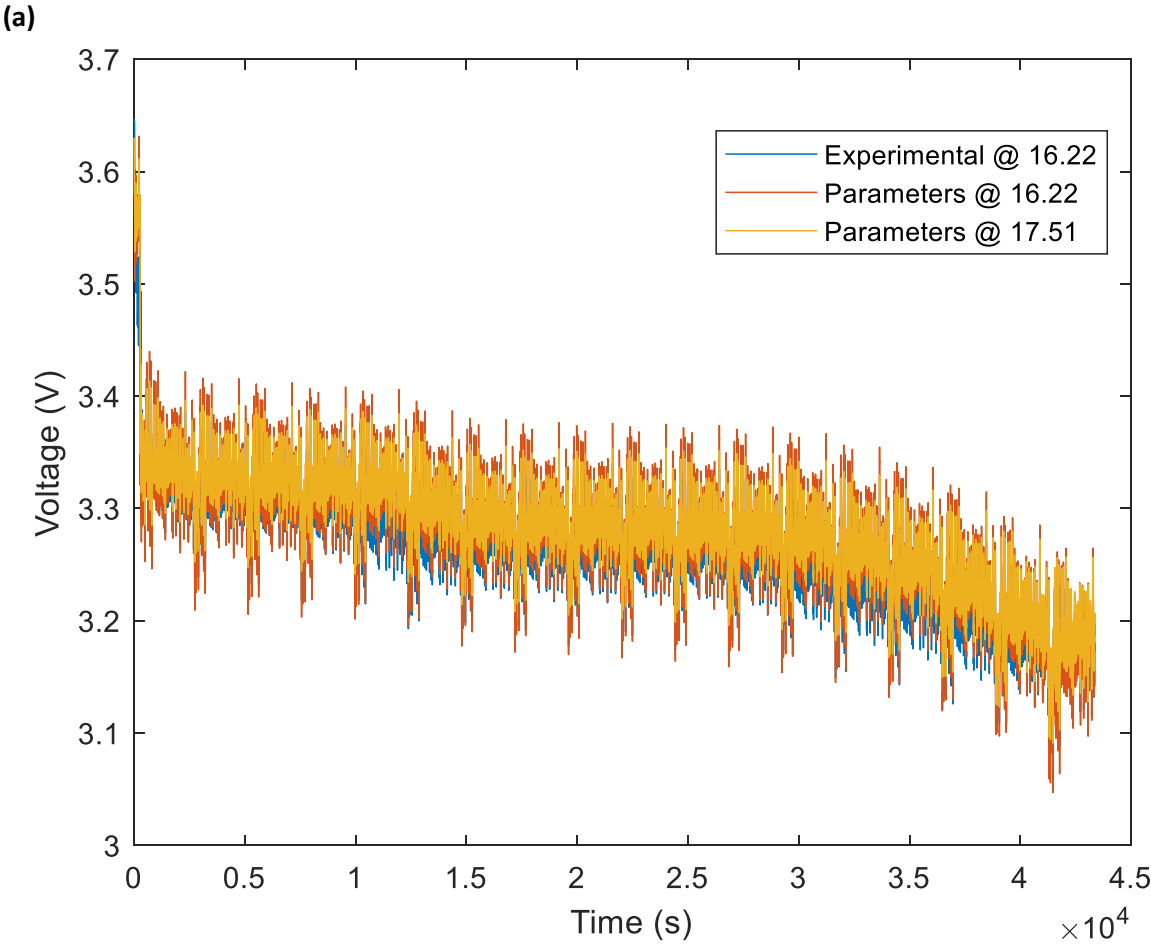
(b)
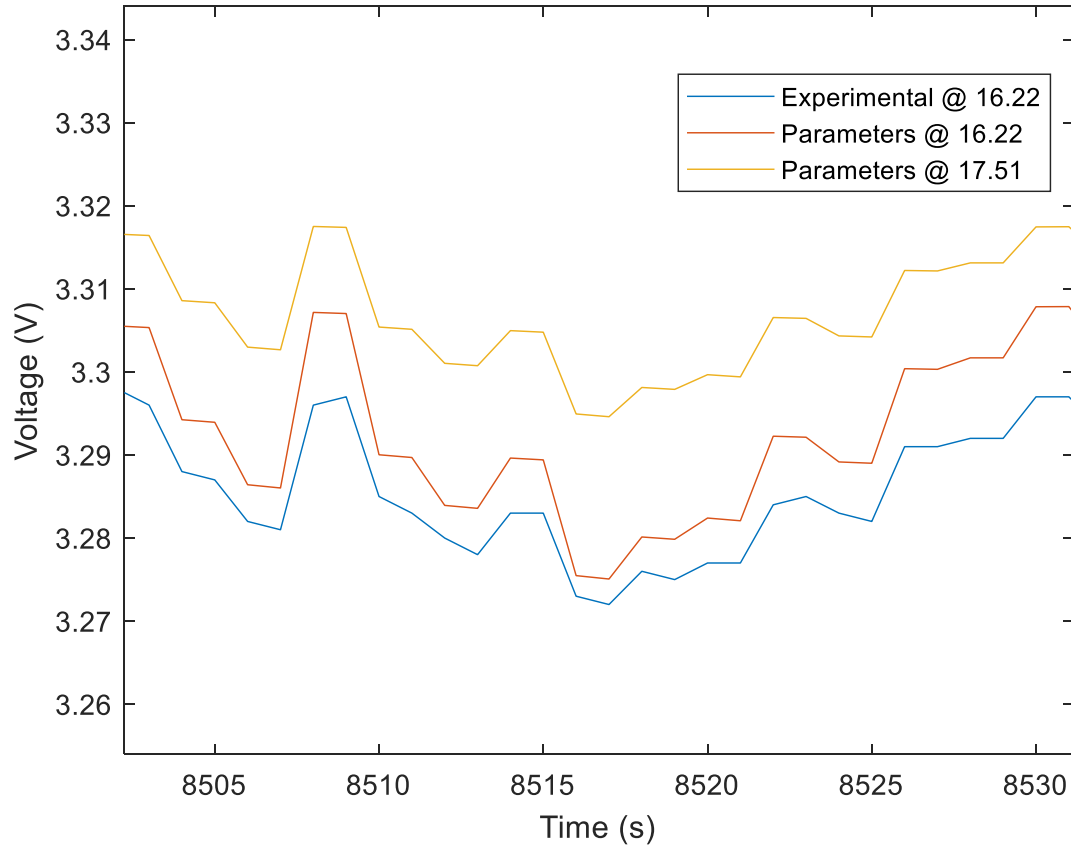
Figure 27. Experimental vs modeled voltage for UDDS cycle run using initial ECM parameters and degraded ECM parameters. (a) Full cycle; (b) Zoomed in.

4.6. Effect of Degradation on ECM Parameters

The RLS estimation was used to estimate the ECM parameters for the UDDS drive cycle at different cell capacities. The selected value for λ is 0.9999 after some tuning, as it gives optimal estimation accuracy for the LFP cell tested. Figure 28 shows how degradation affects these parameters. The degradation effect is more apparent in this figure than in Section 4.4. The effect of degradation on R_0 does not show any clear trend. However, it can be clearly seen that R_1 increases while C_1 decreases with degradation. This makes sense as the RC pair represents the

charge-transfer phenomenon, and degradation can affect the amount of available charge in the battery which is simply capacity. The changes in these parameters are not significant in a short amount of time, i.e. a few drive cycles, but can be very prominent over the lifetime of the battery.

Figure 28. Estimated ECM parameters at various cell capacities. (a) R_0 estimation at different cell capacities; (b) R_1 estimation at different cell capacities; (c) C_1 estimation at different cell capacities.

The qualitative and quantitative results from RLS are consistent with the findings from the HPPC tests in Section 4.4. Therefore, the accuracy and reliability of the RLS algorithm can be confirmed, and RLS can be used with great confidence for the purpose of fault detection.
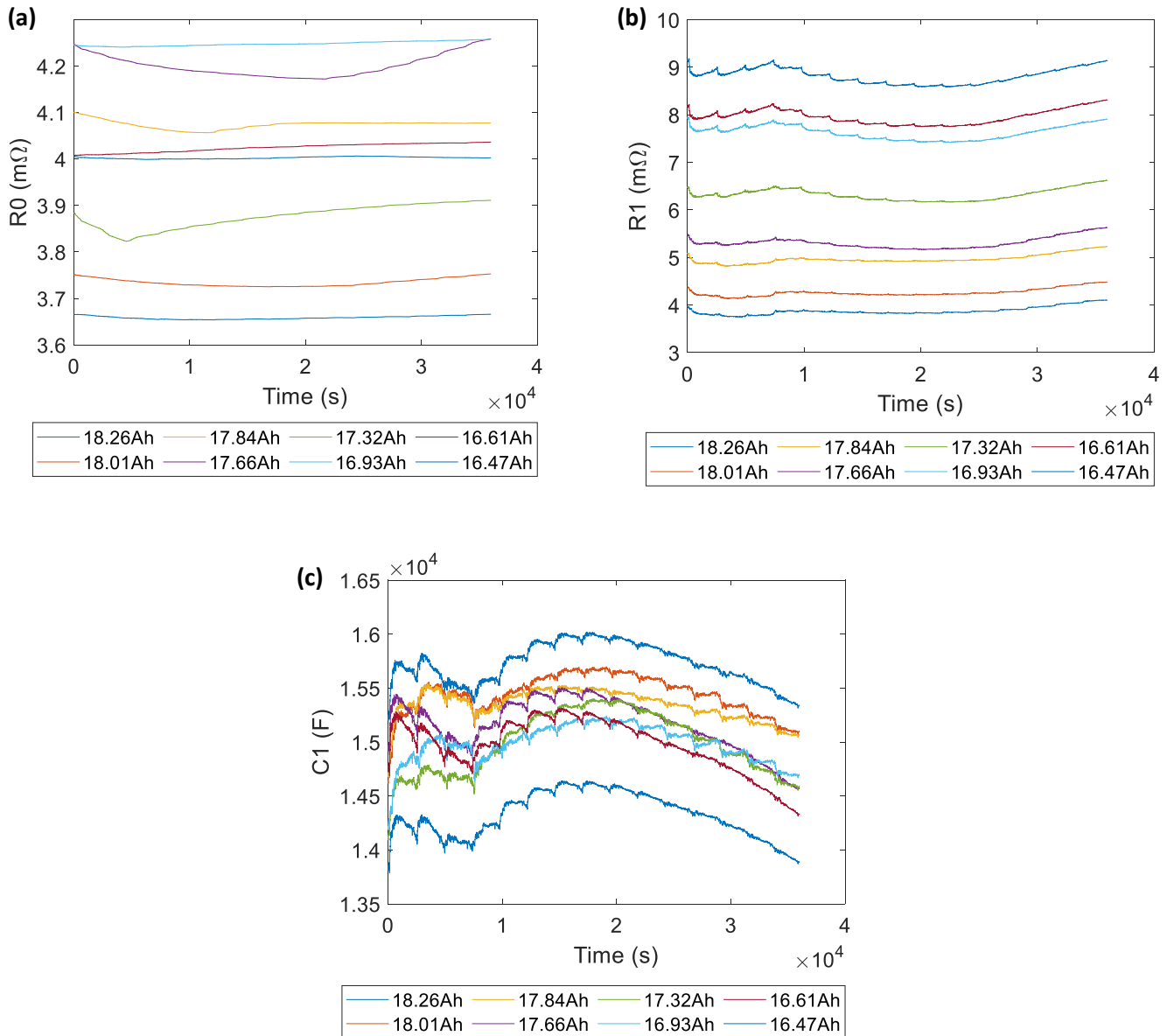
One important detail should be noted, that these changes in ECM parameters due to degradation normally take a long period of time to occur in practical applications such as EVs. In general, a battery is considered to have approached its end of life in EVs application when it reaches about 80% of its original capacity [20]. Most studies have found that an EV battery lifespan ranges from 8 to 10 years, which is consistent with the length of many vehicle manufacturers' warranty terms [73]. The range of capacity shown in Figure 6 above is within 80-90% of the original cell capacity. Therefore, for a short period of time such as a few drive cycles, the degradation effect would be very minimal.

4.7. Effect of Faults on ECM Parameters

The changes in the parameters when the fault is injected are expected to be more significant than other noises such as changes with degradation, SOC or temperature [74]. In order to confirm this, bias and gain faults were injected into the UDDS drive cycles at various cell capacities, times and sizes. Then the RLS algorithm was performed on the runs containing faults. The WMA filter was also applied to confirm its ability to smooth out insignificant noises and its inability to mask faults as normal noises.

The effects of the faults were found to be similar across fault types regardless of the injection time and fault size. An example is shown in Figure 29, where a voltage gain fault of +10% was injected at the time 30,000 s.
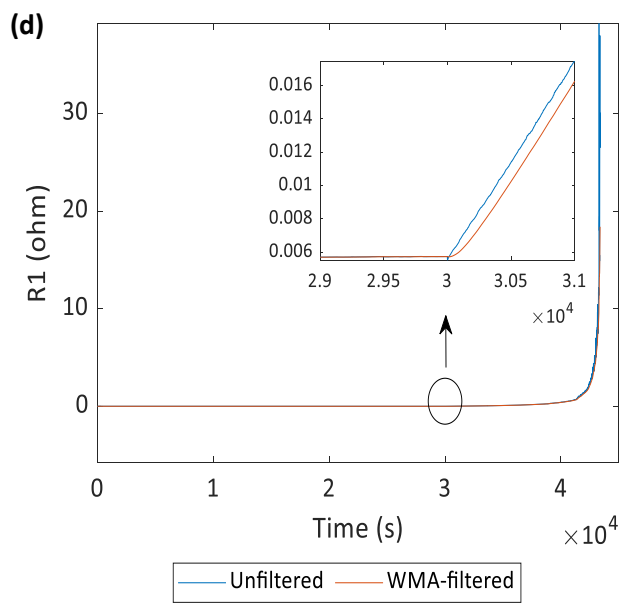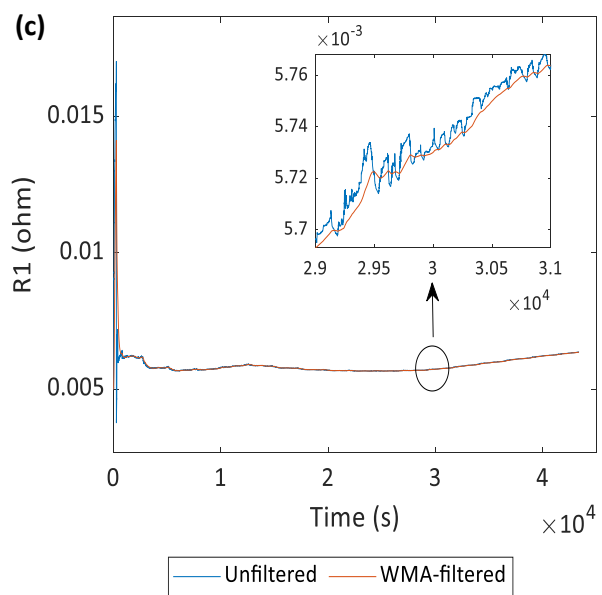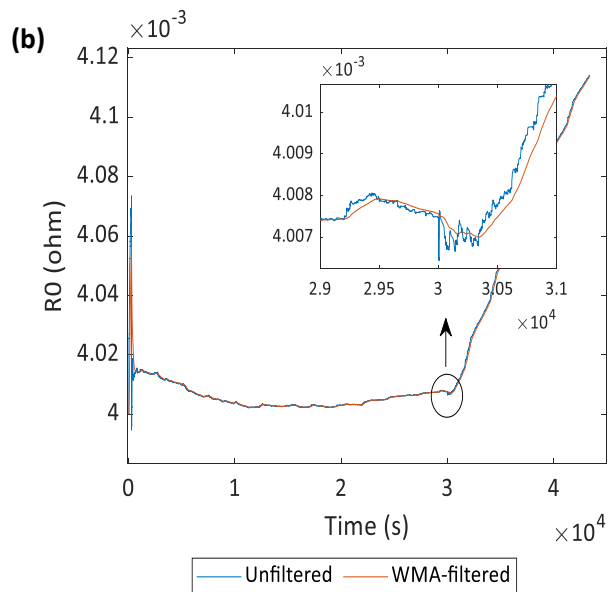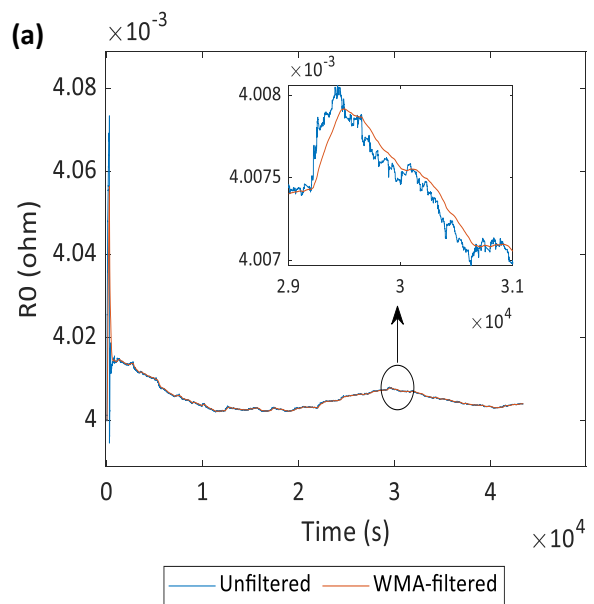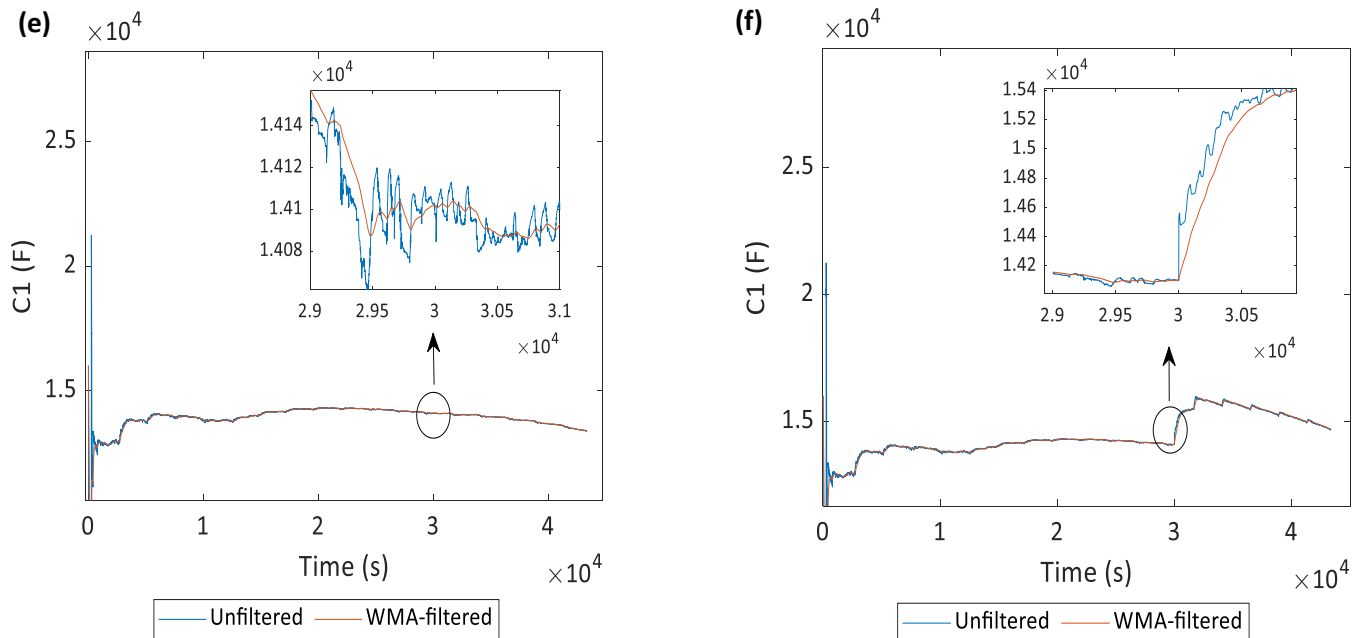
Figure 29. Unfiltered and WMA-filtered ECM parameters obtained from RLS estimation algorithm during normal operation versus when a fault occurs. (a) R_0 during normal operation; (b) R_0 when a fault occurs at time 30,000 s; (c) R_1 during normal operation; (d) R_1 when a fault occurs at time 30,000 s; (e) C_1 during normal operation; (f) C_1 when a fault occurs at time 30,000 s.

When the gain fault occurs on the voltage sensor, as shown in Figures 29 (b), (d) and (f), the parameters diverge significantly away from their original trends. This confirms the significance of the effect of sensor faults on the estimated parameter values. It can also be seen from Figures 29 (a), (c) and (e) that the unfiltered values follow the WMA-filtered line closely during normal operation, while Figures 29 (b), (d) and (f) show that the two lines deviate significantly at the time the fault occurs. This shows that the sensor fault effect is much greater than the effect of other factors such as SOC or temperature. This also confirms the workability of the proposed change-point detection method using WMA and CUSUM. The noises during normal operation are minimal compared to the deviation caused by sensor faults. Therefore, CUSUM should be able to identify sensor faults from the deviation between WMA-filtered values and unfiltered values, due to the faults' significant effect on the estimated ECM parameter values obtained from RLS [75].

It should be noted that the ECM parameters estimated by RLS require some time to converge. This can be seen at the beginning of Figures 29 (a) to (f). Therefore, the proposed FDI scheme would not be able to reliably detect sensor faults for the first hour of battery operation. Considering the long lifespan of Li-ion batteries and the unlikelihood of sensor faults happening within the first hour of operation, it is reasonable to assume there is no fault during the converging period of the RLS algorithm. Another solution for this would be to run the RLS algorithm on the battery for a short period of time to calibrate and stabilize the estimation values before implementing the full FDI scheme.

4.8. Completed FDI Schematic with Fault Isolation

It was discussed in Section 3.5 that the combination of WMA and CUSUM can only detect sensor faults from the RLS estimation but cannot isolate the faults. More studies need to be done to determine how differently the faults affect the parameters. After multiple fault simulations, one particular point was noted during runs, that the parameters do not respond to the faults at the same time, and there was a pattern in the response time. It was found that R_0 deviates from its trend the earliest when current sensor faults occur. Moreover, either R_1 or C_1 responds the fastest to voltage sensor faults, while R_0 takes a longer time to respond. This observation is consistent throughout all simulation runs. This can be explained through the derivation of the RLS algorithm. In Equation (3.4), (3.5) and (3.9), it can be seen that R_0 is the only component in a_2, which is the parameter of I_k (current), while R_1 and C_1 are the components in a_1, which is the parameter of y_{k-1} (voltage). Therefore, abnormality in current would affect R_0 more and faults in voltage would affect R_1 and C_1 more.

From these findings, it is possible to establish a fault isolation schematic to complement the proposed fault detection method. If the CUSUM identifies a fault from R_0, it will be classified as a current sensor fault. If the fault is detected from R_1 or C_1, it will be classified as a voltage sensor fault. It is inconclusive due to the lack of data, whether these faults would have the same effects on a different type of cell, but this will be focused on and further validated in future studies. For this thesis, the FDI scheme will be based on the observations from the tested LFP cell. The

completed FDI scheme includes the fault detection portion presented in Chapter 3, with the addition of the newly established fault isolation method. The final scheme is shown in Figure 30. This FDI algorithm will be used to diagnose sensor faults and validated through simulation in the next chapter.
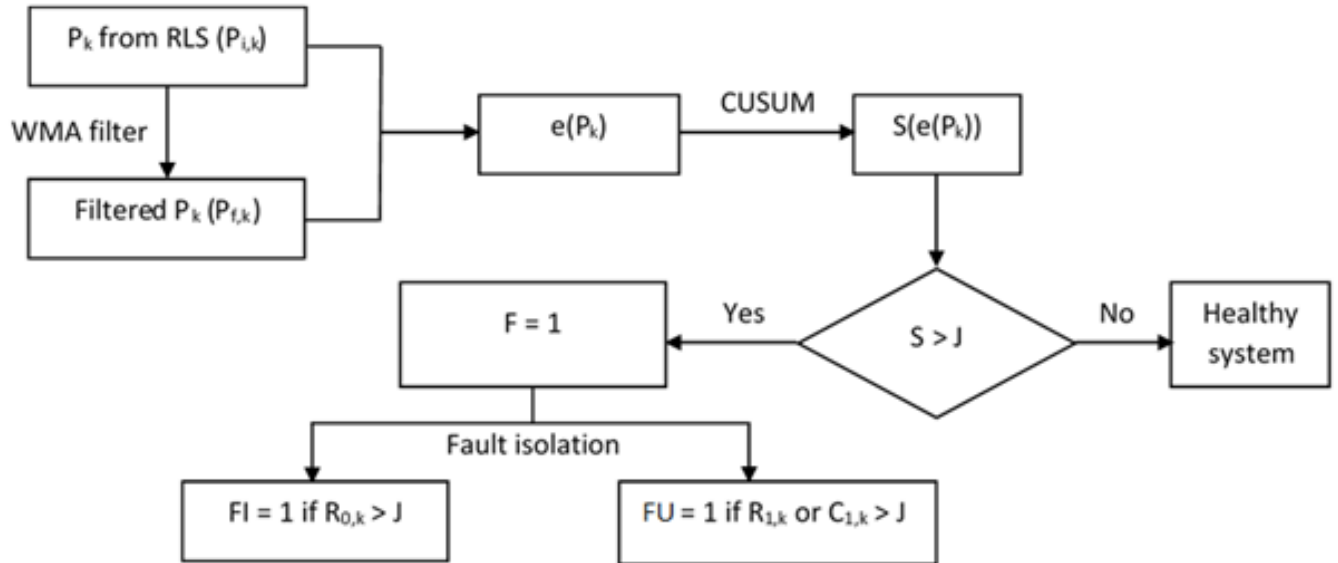

Figure 30. Proposed fault detection and isolation scheme.

5. Fault Detection Scheme Evaluation

This chapter shows the validation results for the proposed FDI scheme. The UDDS drive cycle was selected to be used for validation as it is a realistic daily drive cycle. The experimental runs consisted of multiple UDDS cycles, as described in Section 4.3. The experimental setup is described in Section 4.2. The same set of data obtained in Chapter 4 was also used for the simulations in this chapter. The simulations were conducted at various decreasing cell capacities. Sensor faults of different sizes were injected into the drive cycle at various time points. The FDI scheme was validated at all tested capacities to ensure faults can be diagnosed before and after the cell underwent degradation. The simulation of the FDI scheme was run in MATLAB. The full MATLAB script is shown in Appendix E.

5.1. Simulation of Sensor Faults

Based on the content outlined in Section 2.4, the types of sensor faults chosen for the simulations are bias and gain faults. The selected bias faults for the voltage sensor are [±0.1 V; ±0.5 V], while the gain fault is [±10%]. The selected bias faults for the current sensor are [±4 A; ±7 A] and the gain fault is [±10%]. These faults can be simulated with Equation 2.3, where the actual measurement, after the fault is injected, is offset with a constant value (bias) or with a fraction of its value (gain). The simulation of the fault is done with a MATLAB function script, where the fault size, the fault type, the data file and the fault position are the inputs. The script is shown in Appendix D.

5.2. Voltage Sensor Fault Detection

Multiple voltage sensor faults were injected at different cell capacities in simulation. In this section, one specific case will be shown and discussed in more details as an example. At a cell capacity of 16.47 Ah, a bias fault of +0.5 V was added to the voltage sensor at the time 30,000 s.

The diagnostic results are plotted in Figure 31. Figure 31 (a), (c) and (e) show the deviation between the filtered and unfiltered RLS parameter estimation values in terms of absolute percent error, and the calculation for this error follows Equation 3.18. As can be seen, the error increases significantly shortly after the fault injection time (t = 30,000 s). Figure 31 (b), (d) and (f) show the corresponding CUSUM values for the errors, as calculated using Equation 3.19. The threshold J values for CUSUM were determined to be 0.01, 0.1 and 0.1 for R_0, R_1 and C_1, respectively. These were obtained by running the algorithm without any fault. The CUSUM values should not exceed the thresholds in the case of normal operation, and the threshold values were determined from this criterion. These threshold values are constant for all simulation runs and for this specific cell, but most likely not for all types of cells. Therefore, it should be noted that calibration needs to be done for other cells, before applying the proposed FDI scheme, in order to determine the CUSUM threshold values. Looking closer to the time region when the fault occurs, it can be seen that both CUSUM values for R_1 and C_1 exceed the threshold at 30,002 s, which is 2 seconds after the voltage sensor fault occurs. The CUSUM value for R_0 takes much longer to respond to the fault (856 seconds after fault injection), which is expected for voltage sensor faults and helps to achieve correct fault isolation. Referring back to Figure 30 which shows the completed FDI scheme, the behavior seen with the CUSUM leads to the conclusion that this is a voltage sensor fault. The detected voltage sensor fault signal is plotted in Figure 31 (g). It is concluded that, for this simulation run, the FDI scheme has successfully detected and identified the sensor fault after 2 seconds.

(b)

(c)

(d)
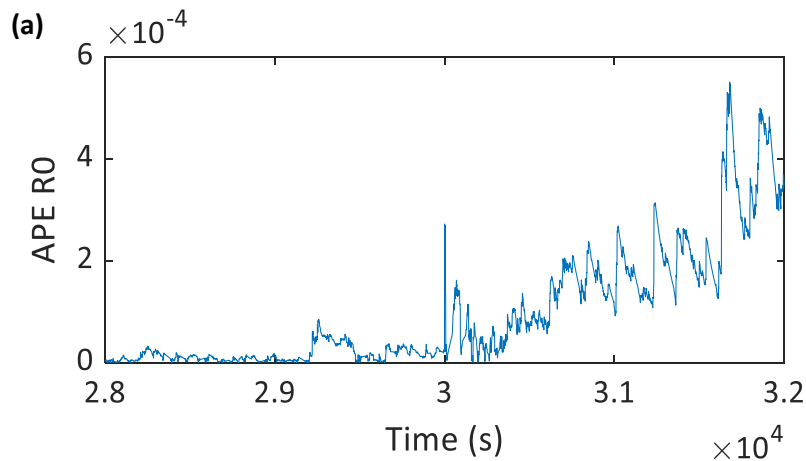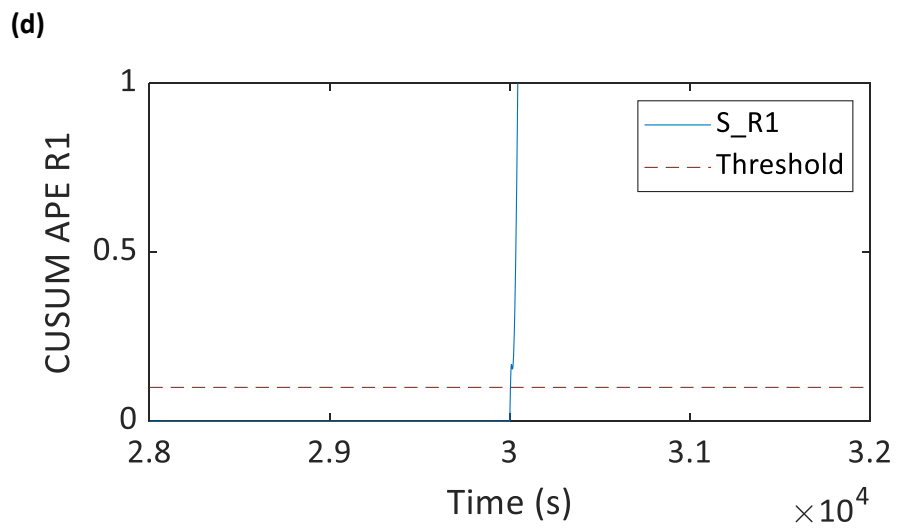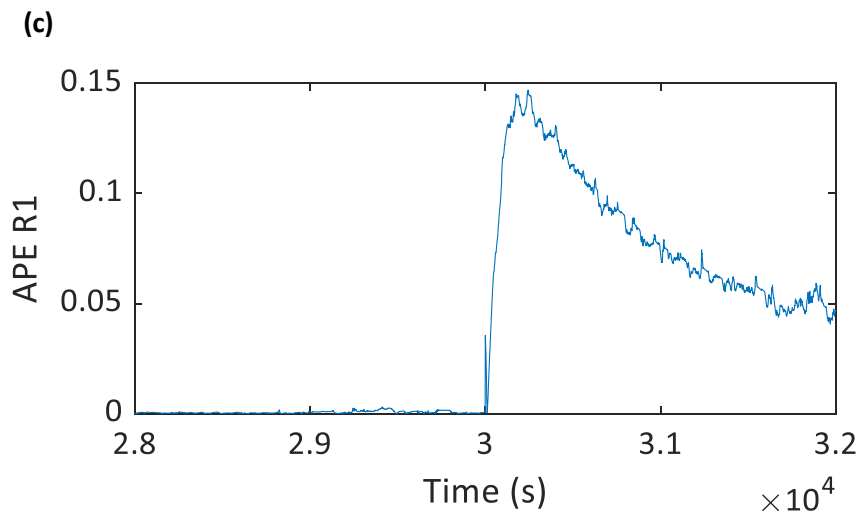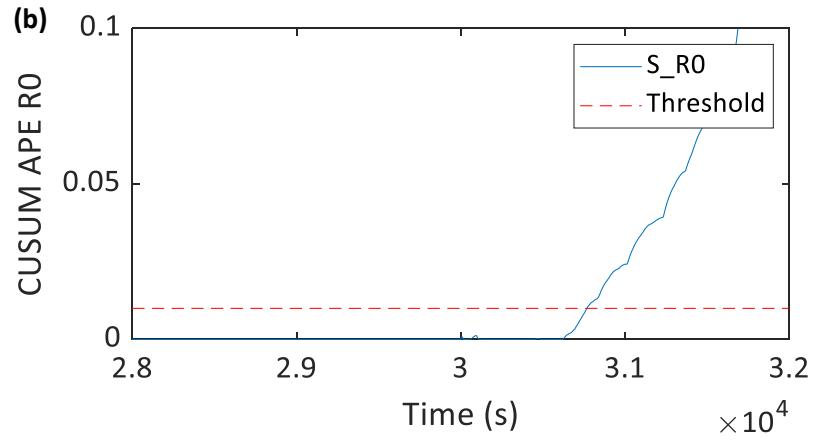
Figure 31. Errors and diagnostic results in the case of voltage sensor fault. (a) Error from R_0; (b) CUSUM control chart for R_0; (c) Error from R_1; (d) CUSUM control chart for R_1; (e) Error from C_1; (f) CUSUM control chart for C_1; (g) Isolated voltage sensor fault F_U signal.

It is not possible to present all graphical results for every simulation run, so the results are better shown as the summary of the detection time for the runs. Table 3 presents results for the detection time of the voltage sensor faults with different fault sizes and cell capacities at an injection time of 30,000 s. As can be seen, larger fault size prompts faster detection time, and cell capacity does not have any clear effect on the detection time.

Table 3. Summary of detection time for voltage sensor faults with different fault sizes and cell capacities.

Fault injected	Capacity (Ah)	18.26	18.01	17.84	17.66	17.32	16.93	16.61	16.47	Average
-0.1 V		14	13	19	12	11	12	10	11	**12.57**
+0.1 V		80	34	44	110	34	115	19	125	**70.13**
-0.5 V	**Detection time (s)**	2	2	3	2	2	2	2	2	**2.13**
+0.5 V		2	2	3	2	2	2	2	2	**2.13**
-10%		3	3	4	3	3	3	3	3	**3.13**
+10%		4	4	5	3	3	3	3	3	**3.50**

5.3. Current Sensor Fault Detection

Similar to the simulation done for voltage sensor fault diagnosis validation, current sensor faults of various sizes were injected at different available cell capacities. The specific case that will be shown as an example is at a cell capacity of 16.47 Ah, where a gain fault of +10% was injected at the time 30,000 s. The diagnostic results are plotted in Figure 32. The absolute percent errors are also found to increase briefly after the time of fault injection, as seen in Figure 32 (a), (c) and (e). Figure 32 (b), (d) and (f) show that the CUSUM values all exceed their respective thresholds after the fault occurs. The results obtained are similar to the ones in Section 5.2, with the only

difference being the response time of the parameters. The CUSUM value for the error of R_0 is the fastest to exceed the threshold, at 30,166 s, while the CUSUM values for R_1 and C_1 exceed their thresholds some time afterward, at 30,376 s and 30,241 s, respectively. This indicates a current sensor fault according to the proposed FDI scheme. Figure 32 (g) shows the detected and isolated current sensor fault signal. The detection time for the current sensor faults suffers from a delay compared to the one for the voltage sensor faults, as the CUSUM values take longer to pass the thresholds. Lowering these thresholds should give faster detection time but risks giving false fault detection, which is a common trade-off in practice [9].
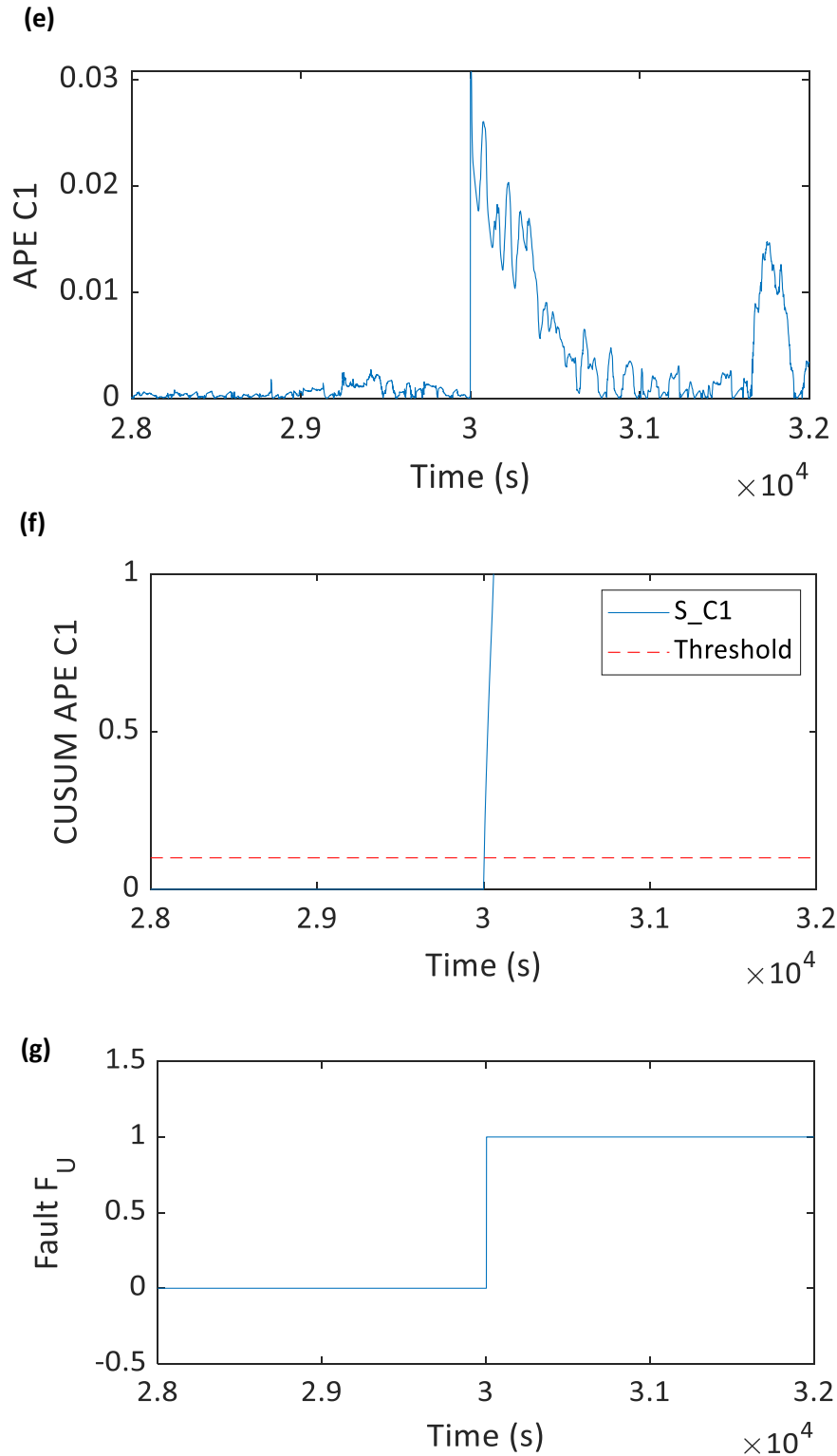
(c)

(d)

(e)

(f)

(g)
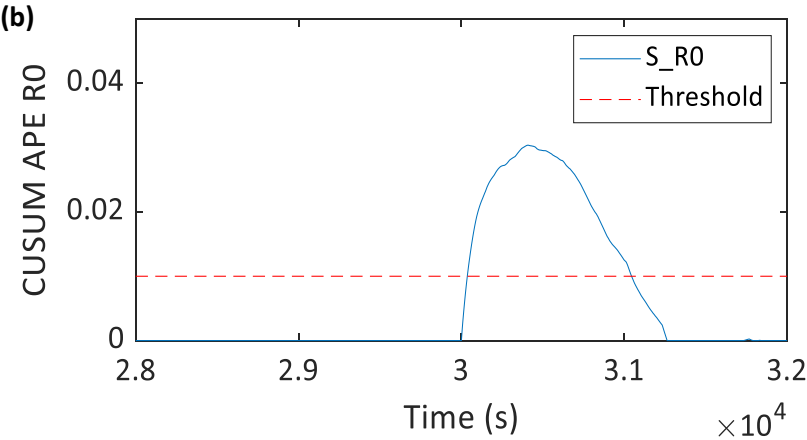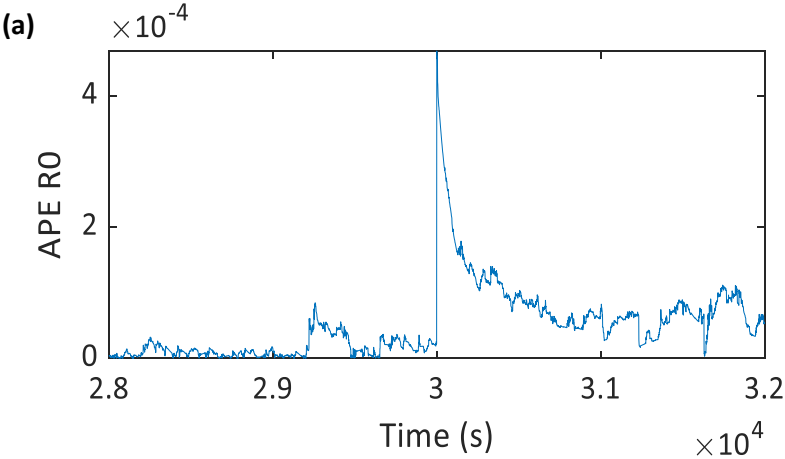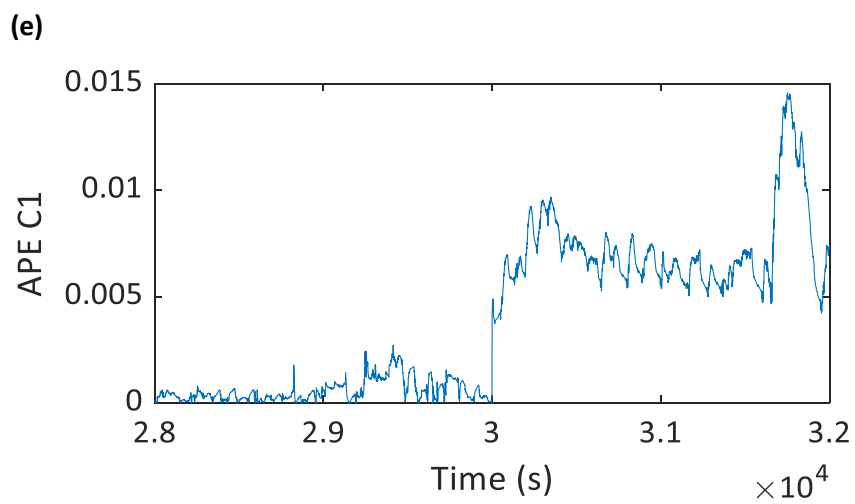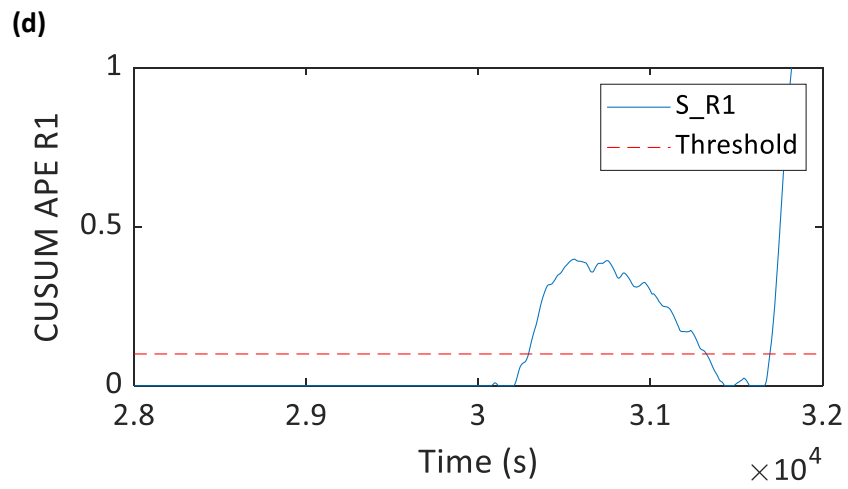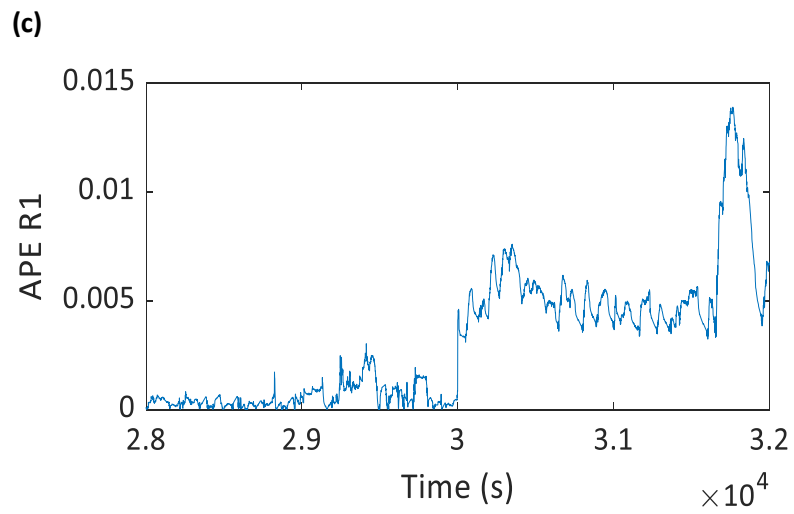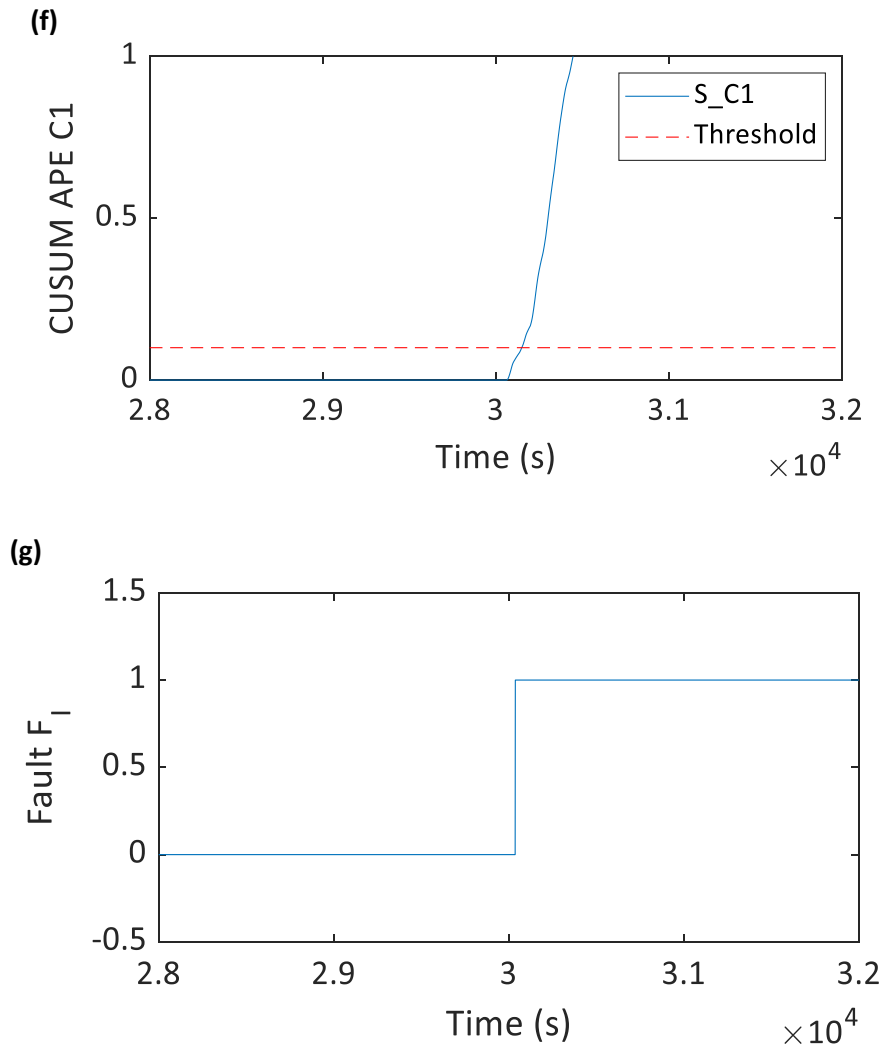
Figure 32. Errors and diagnostic results in the case of current sensor fault. (a) Error from R_0; (b) CUSUM control chart for R_0; (c) Error from R_1; (d) CUSUM control chart for R_1; (e) Error from C_1; (f) CUSUM control chart for C_1; (g) Isolated current sensor fault F_I signal.

Table 4 summarizes the results for detection time for the current sensor at an injection time of 30,000 s with different fault sizes and at different cell capacities. The quantitative results are higher than the ones of voltage sensor faults, but the qualitative observations remain. The larger the fault size, the faster it is detected. Cell capacity is not observed to have any significant effect on fault detection.

**Table 4. Summary of detection time for current sensor faults with different fault sizes and cell capacities.**

Fault injected	Capacity (Ah)	18.26	18.01	17.84	17.66	17.32	16.93	16.61	16.47	Average
-4 A		143	201	190	474	152	560	251	179	**268.75**
+4 A		147	188	174	492	136	543	237	182	**262.38**
-7 A	Detection time (s)	43	65	27	22	57	44	46	37	**42.63**
+7 A		44	54	92	15	54	38	44	36	**47.13**
-10%		175	125	201	29	142	188	176	218	**156.75**
+10%		195	251	181	377	269	180	196	166	**226.88**

5.4. Overall Results

For both voltage and current sensors, more simulations were conducted at different injection times to further test the validity and effectiveness of the proposed FDI scheme, but it is impossible to show all the results individually, so a summary will be presented. The injection times are set at 10,000 s, 20,000 s and 30,000 s. The considered faults for the voltage sensor are [±0.1 V; ±0.5 V; ±10%], while the considered faults for the current sensor are [±4 A; ±7 A; ±10%]. Approximately 300 runs with and without faults were simulated. Table 5 shows the results for maximum, minimum and mean detection time (DT - time from fault occurrence to correct detection and isolation of fault), false detection rate (FDR - fraction of tests that fault is detected where there is no fault) and missed detection rate (MDR - fraction of tests that fault is not detected where there is a fault). It can be concluded from the summary of results that voltage and current sensor faults, on an LFP cell, are successfully detected within a reasonable time using the proposed FDI scheme, with no false detection or missed detection.

Table 5. Summary of the performance evaluation metrics.

	DTmax (s)	DTmin (s)	DTmean (s)	FDR (%)	MDR (%)
Voltage sensor fault	136	2	19	0	0
Current sensor fault	560	15	172	0	0

6. Conclusions and Recommendations

6.1. Conclusions

The objective of this thesis is to confirm the degradation effect on the ECM parameters, design a model-based sensor FDI scheme for a Li-ion cell used in EVs with cell degradation consideration, and validate its performance using a series of experiments and simulations. The proposed FDI scheme should satisfy the requirements of quick detection and diagnosis, isolability, and low modeling and computational requirements. Cell characterization tests, UDDS drive cycles and degradation cycles were carried out on an LFP cell using the Maccor battery test system to collect data to assist with the main framework. The conclusions from the previous chapters of this thesis are summarized as follows:

1) **An FDI scheme is proposed to detect voltage and current sensor faults in the BMS.** The scheme utilizes the RLS algorithm because of its quick convergence and low computational requirements. The RLS is applied to the ECM, a simple battery model, to estimate its parameters in real-time. The estimated parameters are then filtered by the WMA filter. Results from experiments and fault simulations show that, during normal operation, the parameters follow a relatively linear trend, but when a fault occurs, they all deviate from their original trends shortly after. Any significant deviation in the trend of the parameters is detected by the CUSUM control chart, signifying a fault. The threshold values for the CUSUM are calibrated using normal runs without any faults. Finally, fault isolation is achieved based on the response time of the parameters when a sensor fault occurs as certain parameters respond faster to specific types of fault. If the CUSUM identifies a fault from R_0 first, it will be classified as a current sensor fault, while if the fault is detected from R_1 or C_1 first, it will be classified as a voltage sensor fault.

2) **Results from HPPC and RLS parameters estimation show that cell degradation affects the ECM parameters significantly over time.** The degradation is shown through the decrease in cell capacity, from 18.26 Ah to 16.47 Ah. Even though in EVs application the degradation process can take years to manifest, it still makes state observer FDI schemes unreliable because they work under the assumption that the battery model parameters

remain constant. The modeled and predicted state (voltage) values will ramify as the parameters change, especially as the battery approaches its end of life in EVs. The changes in parameters due to degradation, however, do not affect the performance of the proposed FDI scheme as it only detects large deviations (caused by sensor faults) in a short timeframe, and degradation does not cause sharp fluctuations in the ECM parameters.

3) **The proposed sensor FDI scheme is validated and evaluated with experimental data in combination with fault simulation in MATLAB.** The data used to validate the performance of the FDI scheme is generated from running UDDS drive cycles on the LFP cell. Various injection times, fault sizes, fault types and cell capacities are considered. The validation results show that the proposed scheme consistently detects and isolates voltage sensor faults and current sensor faults at different cell capacities in a reasonable time, with no false or missed detection.

6.2. Recommendations

The objective of this thesis, as stated in Section 6.1, has been met, but there is some more work that can be done in the future to improve the proposed BMS sensor FDI scheme. The following recommendations outline areas of focus for future work in the testing of LFP batteries and potential methods to improve the workability of the FDI scheme presented in this work.

1) **The FDI scheme can be expanded to include fault diagnosis for temperature sensor.** There are three main sensors in the BMS (voltage, current, and temperature). Voltage and current sensors have been addressed in this thesis. It will be interesting to study the effect of temperature on the model parameters and how it influences the proposed Li-ion cell fault diagnosis. Two approaches to integrate temperature sensor FDI into the existing scheme are suggested. A separate FDI algorithm can be developed for temperature sensor exclusively to work in conjunction with the existing scheme, while the effect of temperature sensor faults on the existing scheme is studied. Alternatively, a new model, instead of the first-order ECM, can be developed and implemented to include

temperature, and the FDI algorithm (RLS, WMA, and CUSUM) is modified appropriately to accommodate the new model.

2) **Other battery models, including both electrochemical and electrical, can be explored for more accurate modeling of the Li-ion battery behavior.** For example, the second-order ECM should be investigated. The computational cost and the performance of the new FDI scheme (second-order ECM) can be compared to the current one (first-order ECM) to determine if the trade-off is justifiable. Electrochemical models, despite their complexity, should be investigated as well, since they usually include temperature. This fits well with the scope discussed in the first recommendation.

3) **Longer test cycles with more variety of profiles need to be conducted on the cell to improve the reliability of the FDI results.** The duration of the current test cycle is 12 hours, and it only includes the UDDS drive cycle. Ideally, the experiment should include UDDS, HWFET, rest periods and other stochastic current profiles, and run for two weeks to a month, possibly much longer if realistic degradation is desired. Because of the time constraint of this thesis, it was not feasible to carry out such long-term experiment. However, an experiment of this nature is currently under development and will start in the near future.

4) **Other fault diagnosis methods, specifically knowledge-based methods such as machine learning, should be investigated.** Currently, the amount of data collected is not suitable for machine learning. As discussed in the previous point, more dynamic experiments with longer duration will be conducted in the future. Once a sufficient amount of data has been obtained, machine-learning-based fault detection or similar methods should be developed for BMS sensors. This will eliminate the dependency on battery models and improve the reliability of the FDI.

5) **The extension of fault diagnosis from LFP cells to other types of cells, and to battery modules/packs should be examined.** Consistency is an important trait of any FDI scheme. Therefore, Li-ion cells with different chemistry should also be investigated to validate the proposed FDI scheme. Data obtained can also be used to observe whether cell chemistry would have any effect on the response time of the parameters when a fault occurs, and

effectively confirm the fault isolation algorithm. Moreover, since the cells in a battery module/pack can behave differently, it is also necessary to conduct experiments with multiple cells in series or parallel. This is an important study to validate the workability of the proposed FDI scheme in practical applications, especially in the case of EVs where a battery pack consists of hundreds of cells.

6) **The worst-case scenario where the fault occurs during the shutdown period of the vehicle should be investigated.** The current scheme can only detect faults during operation, not when the BMS is turned off. If there is a fault during this period, the fault will go undetected because the proposed scheme assumes normal operation at the beginning. Therefore, this is an important case to look into to improve the completeness of the FDI scheme.

7) **A study on ECM parameters measured by Electrochemical Impedance Spectroscopy should be conducted.** This study is necessary to observe the difference between the estimated parameters and measured parameters. If the two values are similar to a reasonable degree, the algorithm can be improved to detect deviations between the measured and predicted values, to replace the current method of change detection in a time series which is less reliable.

7. References

1. Independent Electricity System Operator, "Supply Overview," 2019. [Online]. Available: http://www.ieso.ca/en/Power-Data/Supply-Overview/Transmission-Connected-Generation [Accessed 10 September 2019].

2. Toyota, 2013. [Online]. Available: http://www.toyotapriusbattery.com/.

3. K. Smith, M. Earleywine, E. Wood, J. Neubauer and A. Pesaran, "Comparison of Plug-In Hybrid Electric Vehicle Battery Life Across Geographies and Drive Cycles," in 2012 SAE World Congress and, Detroit, Michigan, 2012.

4. H. Cars, "History of Hybrid Vehicles," 27 March 2006. [Online]. Available: http://web.archive.org/web/20090208230718/http:/www.hybridcars.com/history/history-of-hybrid-vehicles.html. [Accessed 17 October 2015].

5. "Electric Vehicle Market Forecast Report, 2023 - Top Key Players Analyzed: Tesla, Volkswagen, Mitsubishi, Renault, Nissan, & BMW: Radiant Insights, Inc." Journal of Engineering, 27 May 2019, p. 252. Gale Academic Onefile, https://link.gale.com/apps/doc/A586717504/AONE?u=uniwater&sid=AONE&xid=de6a97bb. Accessed 21 Oct. 2019.

6. IEA (2019), "Global EV Outlook 2019", IEA, Paris, www.iea.org/publications/reports/globalevoutlook2019/.

7. Ould Amrouche, S.; Rekioua, D.; Rekioua, T.; Bacha, S. Overview of energy storage in renewable energy systems. International Journal of Hydrogen Energy 2016, 41, 20914–20927.

8. Lu, L.; Han, X.; Li, J.; Hua, J.; Ouyang, M. A review on the key issues for lithium-ion battery management in electric vehicles. Journal of Power Sources 2013, 226, 272–288.

9. Liu, Z.; He, H. Sensor fault detection and isolation for a lithium-ion battery pack in electric vehicles using adaptive extended Kalman filter. Applied Energy 2017, 185, 2033–2044.

10. Liu, Z.; He, H. Model-based Sensor Fault Diagnosis of a Lithium-ion Battery in Electric Vehicles. Energies 2015, 8, 6509–6527.

11. Wu, C.; Zhu, C.; Ge, Y.; Zhao, Y. A Review on Fault Mechanism and Diagnosis Approach for Li-Ion Batteries. Journal of Nanomaterials 2015, 2015, 1–9.

12. Zhang, X.; Lu, J.; Yuan, S.; Yang, J.; Zhou, X. A novel method for identification of lithium-ion battery equivalent circuit model parameters considering electrochemical properties. Journal of Power Sources 2017, 345, 21–29.

13. Yang, G.; Li, J.; Fu, Z.; Guo, L. Adaptive state of charge estimation of Lithium-ion battery based on battery capacity degradation model. Energy Procedia 2018, 152, 514–519.

14. Dubarry, M.; Berecibar, M.; Devie, A.; Anseán, D.; Omar, N.; Villarreal, I. State of health battery estimator enabling degradation diagnosis: Model and algorithm description. Journal of Power Sources 2017, 360, 59–69.

15. Fleischer, C.; Waag, W.; Heyn, H.-M.; Sauer, D.U. On-line adaptive battery impedance parameter and state estimation considering physical principles in reduced order equivalent circuit battery models part 2. Parameter and state estimation. Journal of Power Sources 2014, 262, 457–482.

16. M. Kassem and C. Delacourt, "Postmortem analysis of calendar-aged graphite/LiFePO4 cells," Journal of Power Sources, vol. 235, pp. 159-171, 2013.

17. M. Safari and C. Delacourt, "Aging of a Commercial Graphite/LiFePO4 Cell," Journal of The Electrochemical Society, vol. 158, no. 10, pp. A1123-A1135, 2011.

18. D. Linden and T. B. Reddy, "Chapter 1 Basic Concepts," in Handbook of Batteries, New York, McGraw-Hill, 2002.

19. D. Linden and T. B. Reddy, Battery Power and Products Technology, vol. 5, no. 2, pp. 10–12, March/April 2008.

20. D. Finley, "Battery Degradation Modeling for Vehicle Applications," University of Waterloo, Waterloo, Ontario, 2014.

21. I. Husain, in Electric and Hybrid Vehicles: Design Fundamentals, Second Edition, CRC Publisher, 2010.

22. D. Linden and T. B. Reddy, "Chapter 2 Electrical Principles and Reactions," in Handbook of Batteries, New York, McGraw-Hill, 2002.

23. S. Grolleau, A. Delaille, H. Gualous, P. Gyan, R. Revel, J. Bernard, E. Redondo-Iglesias and J. Peter, "Calendar aging of commercial graphite/LiFePO4 cell - Predicting capacity fade under time dependent storage conditions," Journal of Power Sources, vol. 255, pp. 450-458, 2014.

24. K. Young, C. Wang, L. Y. Wang and a. K. Strunz, Electric Vehicle Integration into Modern Power Networks, R. Garcia-Valle and J. A. P. Lopes, Eds., New York: Springer Science+Business Media, 2013, pp. 15-56.

25. A. Barré, B. Deguilhem, S. Grolleau, M. Gérard, F. Suard and D. Riu, "A review on lithium-ion battery ageing mechanisms and estimations for automotive applications," Journal of Power Sources, vol. 241, pp. 680-689, 2013.

26. A. Barré, B. Deguilhem, S. Grolleau and M. Gérard, "A review on lithium-ion battery ageing mechanisms and estimations for automotive applications," Journal of Power Sources, vol. 241, pp. 680-689, 2013.

27. B. Xu, "Degradation-limiting Optimization of Battery Energy Storage Systems Operation," Federal Institute of Technology Zurich (ETH Zurich), Zurich, 2013.

28. E. Wood, "Battery End-of-Life Considerations for Plug-in Hybrid Electric Vehicles," Colorado State University, Fort Collins, Colorado, 2011.

29. M. Kassem, J. Bernard, R. Revel, S. Pélissier, F. Duclaudd and C. Delacourt, "Calendar aging of a graphite/LiFePO4 cell," Journal of Power Sources, vol. 208, pp. 296-305, 2012.

30. C. Lin, A. Tang, H. Mu, WenweiWang and C. Wang, "Aging Mechanisms of Electrode Materials in Lithium-Ion Batteries for Electric Vehicles," Journal of Chemistry, vol. 2015, pp. 1-11, 2015.

31. A. Barré, B. Deguilhem, S. Grolleau, M. Gérard, F. Suard and D. Riu, "A review on lithium-ion battery ageing mechanisms and estimations for automotive applications," Journal of Power Sources, vol. 241, pp. 680-689, 2013.

32. P. Keil, S. F. Schuster, J. Wilhelm, J. Travi and A. Hauser, "Calendar Aging of Lithium-Ion Batteries I. Impact of the Graphite Anode on Capacity Fade," Journal of The Electrochemical Society, vol. 163, no. 9, pp. 1872-1880, 2016.

33. Q. Badey, G. Cherouvrier, Y. Reynier, J.-M. Duffault and S. Franger, "Ageing forecast of lithium-ion batteries for electric and hybrid vehicles," Current Topics in Electrochemistry, vol. 16, pp. 65-79, 2011.

34. K. Ohue, T. Utsunomiya, O. Hatozaki, N. Yoshimotoa, M. Egashira and M. Morita, "Self-discharge behavior of polyacenic semiconductor and graphite negative electrodes for lithium-ion batteries," Journal of Power Sources, vol. 196, p. 3604–3610, 2011.

35. M. Kassem, J. Bernard, R. Revel, S. Pélissier, F. Duclaud and C. Delacourt, "Calendar aging of a graphite/LiFePO4 cell," Journal of Power Sources, vol. 208, p. 296–305, 2012.

36. A. W. Golubkov, D. Fuchs, J. Wagner, H. Wiltsche, C. Stangl, G. Fauler, G. Voitic, A. Thaler and V. Hacker, "Thermal-runaway experiments on consumer Li-ion batteries with metal-oxides and olivin-type cathodes," RSC Adv., vol. 4, pp. 3633-3642, 2014.

37. C. Mikolajczak, M. Kahn, K. White and R. T. Long, "Lithium-Ion Batteries Hazard and Use Assessment," Quincy, 2011.

38. V. Ramadesigan, P. W. C. Northrop, S. De, S. Santhanagopalan, R. D. Braatz and a. V. R. Subramaniana, "Modeling and Simulation of Lithium-Ion Batteries from a Systems Engineering Perspective," Journal of The Electrochemical Society, vol. 159, no. 3, pp. 31-45, 2012.

39. X. Hua, S. Li and H. Peng, "A comparative study of equivalent circuit models for Li-ion batteries," Journal of Power Sources, vol. 198, pp. 359-367, 2012.

40. H.Chan, A new battery model for use with battery energy storage systems and electric vehicles power systems, in Power Engineering Society Winter Meeting, 2000:470–475.

41. J. P. Cun, J. N. Fiorina, M. Fraisse, and H. Mabboux, The experience of a UPS company in advanced battery monitoring, in 18th international Telecommunications Energy Conference, 1996: 646–653.

42. M. Chen and G. Rincon-Mora, Accurate electrical battery model capable of predicting runtime and I-V performance, IEEE Transaction on Energy Conversion, 21: 504-511, 2006.

43. S. Buller, M. Thele, R. Doncker, and E. Karden, Impedance based simulation models of super-capacitors and Li-ion batteries for power electronic applications,in Industrial Application Conference, 2003

44. Sun, Kai & Shu, Qifang. (2011). Overview of the types of battery models. Proceedings of the 30th Chinese Control Conference, CCC 2011.

45. Rahimi-Eichi, H.; Ojha, U.; Baronti, F.; Chow, M.-Y. Battery Management System: An Overview of Its Application in the Smart Grid and Electric Vehicles. EEE Ind. Electron. Mag. 2013, 7, 4–16.

46. Lelie, M.; Braun, T.; Knips, M.; Nordmann, H.; Ringbeck, F.; Zappen, H.; Sauer, D. Battery Management System Hardware Concepts: An Overview. Applied Sciences 2018, 8, 534.

47. C. Hendricks, N. Williard, S. Mathew and M. Pecht, "A failure modes, mechanisms, and effects analysis (FMMEA) of lithium-ion batteries," Journal of Power Sources, vol. 297, pp. 113-120, 2015.

48. Fabian Luttenberger, A.L.G. Electric Components in Automotive Battery Systems Above 800 V; Battery Power (Kraftwerk Batterie): Essen, Germany, 2017.

49. Hauser, A.; Kuhn, R. High-voltage battery management systems (BMS) for electric vehicles. In Advances in Battery Technologies for Electric Vehicles; Scrosati, B., Garche, J., Tillmetz, W., Eds.; Elsevier: Amsterdam, The Netherlands, 2015; Chapter 11, pp. 265–281; ISBN 978-1-78242-377-5.

50. Pettigrew,W. Selecting the Most Effective Current Sensing Technology. Power Electron. Eur. 2007, 8, 27–31.

51. Lerch, R. Elektrische Messtechnik, 6th ed.; Springer Vieweg: Berlin, Germany, 2012; ISBN 978-3-642-22608-3.

52. Gao, Z.; Cecati, C.; Ding, S.X. A Survey of Fault Diagnosis and Fault-Tolerant Techniques—Part I: Fault Diagnosis With Model-Based and Signal-Based Approaches. IEEE Trans. Ind. Electron. 2015, 62, 3757–3767.

53. Venkatasubramanian, V.; Rengaswamy, R.; Yin, K.; Ka, S.N. A review of process fault detection and diagnosis Part I: Quantitative model-based methods. Computers and Chemical Engineering 2003, 19.

54. Marcicki, J.; Onori, S.; Rizzoni, G. Nonlinear Fault Detection and Isolation for a Lithium-Ion Battery Management System. In Proceedings of the ASME 2010 Dynamic Systems and Control Conference, Volume 1; ASMEDC: Cambridge, Massachusetts, USA, 2010; pp. 607–614.

55. Chen, W.; Chen, W.-T.; Saif, M.; Li, M.-F.; Wu, H. Simultaneous Fault Isolation and Estimation of Lithium-Ion Batteries via Synthesized Design of Luenberger and Learning Observers. IEEE Trans. Contr. Syst. Technol. 2014, 22, 290–298.

56. Liu, Z.; Ahmed, Q.; Zhang, J.; Rizzoni, G.; He, H. Structural analysis based sensors fault detection and isolation of cylindrical lithium-ion batteries in automotive applications. Control Engineering Practice 2016, 52, 46–58.

57. Dey, S.; Mohon, S.; Pisu, P.; Ayalew, B. Sensor Fault Detection, Isolation, and Estimation in Lithium-Ion Batteries. IEEE Trans. Contr. Syst. Technol. 2016, 24, 2141–2149.

58. Che Mid, E.; Dua, V. Model-Based Parameter Estimation for Fault Detection Using Multiparametric Programming. Ind. Eng. Chem. Res. 2017, 56, 8000–8015.

59. Isermann, R. (1989). Process fault diagnosis based on dynamic models and parameter estimation methods. In R. J. Patton, P. M. Frank & R. N. Clark (Eds.), Fault diagnosis in dynamic systems: theory and applications . NY: Prentice Hall.

60. Aminikhanghahi, S.; Cook, D.J. A survey of methods for time series change point detection. Knowl Inf Syst 2017, 51, 339–367.

61. Montanez GD, Amizadeh S, Laptev N. Inertial Hidden Markov Models: Modeling Change in Multivariate Time Series. AAAI Conference on Artificial Intelligence. 2015:1819–1825.

62. Kawahara Y, Sugiyama M. Sequential Change-Point Detection Based on Direct Density-Ratio Estimation. SIAM International Conference on Data Mining. 2009:389–400.

63. Downey AB. A novel changepoint detection algorithm. Dec.2008

64. R. Nicolas, "The different driving cycles," 5 January 2013. [Online]. Available: http://www.car-engineer.com/the-different-driving-cycles/. [Accessed 03 July 2019].

65. US Environmental Protection Agency, "Dynamometer Drive Schedules," 27 April 2016. [Online]. Available: https://www.epa.gov/vehicle-and-fuel-emissions-testing/dynamometer-drive-schedules. [Accessed 26 February 2019].

66. Christopherson, J.P. Battery Test Manual for Electric Vehicles. Idaho National Laboratory 2015

67. Princeton Applied Research, "MODEL 4200M DESKTOP AUTOMATED TEST SYSTEM", November 2014. [Online]. Available: http://www.maccor.com/ProductDocs/Data%20Sheet%20for%20Model%204200M%20Test%20System.pdf. [Accessed 9 October 2019].

68. Thanagasundram, Suguna & Arunachala, Raghavendra & Makinejad, Kamyar & Teutsch, Tanja & Jossen, Andreas. (2012). A Cell Level Model for Battery Simulation.

69. Taverne, Jonas & Ayub, Ahmad & Sellami, Nazmi & Abu-Bakar, Siti Hawa & Bani, Nurul & Mas'ud, Abdullahi & Iyi, Draco & Muhammad-Sukki, Firdaus. (2018). Design of Solar Powered Charging Backpack. International Journal of Power Electronics and Drive Systems. 9. 10.11591/ijpeds.v9n2.pp848-858.

70. He, H.; Zhang, X.; Xiong, R.; Xu, Y.; Guo, H. Online model-based estimation of state-of-charge and open-circuit voltage of lithium-ion batteries in electric vehicles. Energy 2012, 39, 310–318.

71. Perry, M.B. The Weighted Moving Average Technique. In Wiley Encyclopedia of Operations Research and Management Science; John Wiley & Sons, Inc.: Hoboken, NJ, USA, 2011; p. eorms0964 ISBN 978-0-470-40053-1.

72. Jeske, D.R.; Montes De Oca, V.; Bischoff, W.; Marvasti, M. Cusum techniques for timeslot sequences with applications to network surveillance. Computational Statistics & Data Analysis 2009, 53, 4332–4344.

73. Richa, K., Babbitt, C. W., Gaustad, G., & Wang, X. (2014). A future perspective on lithium-ion battery waste flows from electric vehicles. Resources, Conservation and Recycling, 83, 63–76.

74. Gomez, J.; Nelson, R.; Kalu, E.E.; Weatherspoon, M.H.; Zheng, J.P. Equivalent circuit model parameters of a high-power Li-ion battery: Thermal and state of charge effects. Journal of Power Sources 2011, 196, 4826–4831.

75. Tran, M.-K.; Fowler, M. Sensor Fault Detection and Isolation for Degrading Lithium-Ion Batteries in Electric Vehicles Using Parameter Estimation with Recursive Least Squares. Batteries 2020, 6, 1.

Appendix A: Test Procedure

- Select Channel 9 by clicking on it
- If the channel is not clear, the current data needs to be saved before continuing
- Click "ViewData data viewer" in top righthand corner (third button from the left)
- Select "File → Save As", enter the filename and file location to save the data as a .txt file
- Follow the file naming convention: TestName_MonthDay.txt
- A "Print Range" prompt will appear with "All" being the default, click OK
- Once the confirmation message appears reading "File Saved", click the Stop button in the top righthand corner (the symbol is a Red Square) which will archive the data in Channel 9
    - Do NOT click the Stop button before saving as the Stop button will clear the data from the channel – go to ViewData data viewer first to save the data then click Stop
- At this point, the channel is clear and ready to begin another test
- Right click and select "Start Test" or click the Play button in the top righthand corner
- Scroll through tests to select the desired test
    - For UDDS: LFP_UDDS_Kien.000
    - For RegD: LFP_RegD_Kien.000
    - For Degradation: LFP_Degradation_Kien.000
    - For Capacity: LFP_Capacity_Kien.000
- When test is complete, channel will read "Complete" with all green text
- UDDS and RegD will take approximately one day to complete and they will complete on their own
- Degradation must be terminated by the user after 5 days
    - Click the Pause button in the top righthand corner then save the data, then click Stop
- Testing order: Capacity, UDDS, RegD, Degradation
- Pictures shown below: Maccor user interface, UDDS test, degradation test
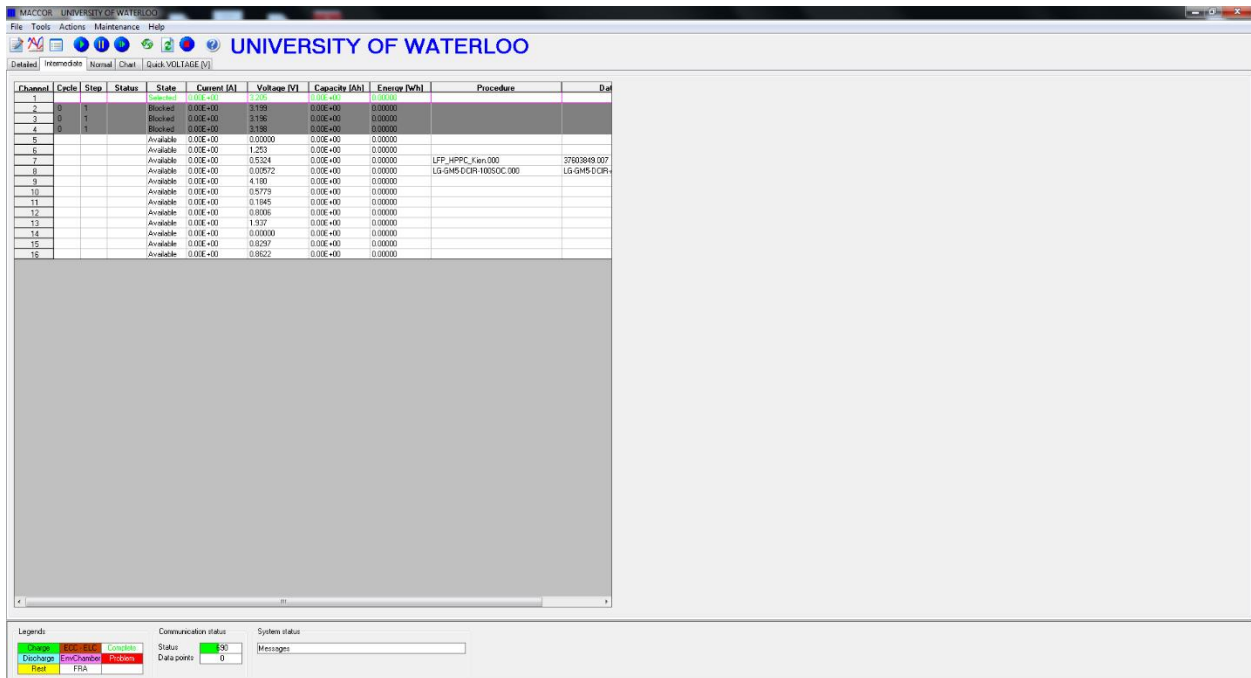
Maccor user interface
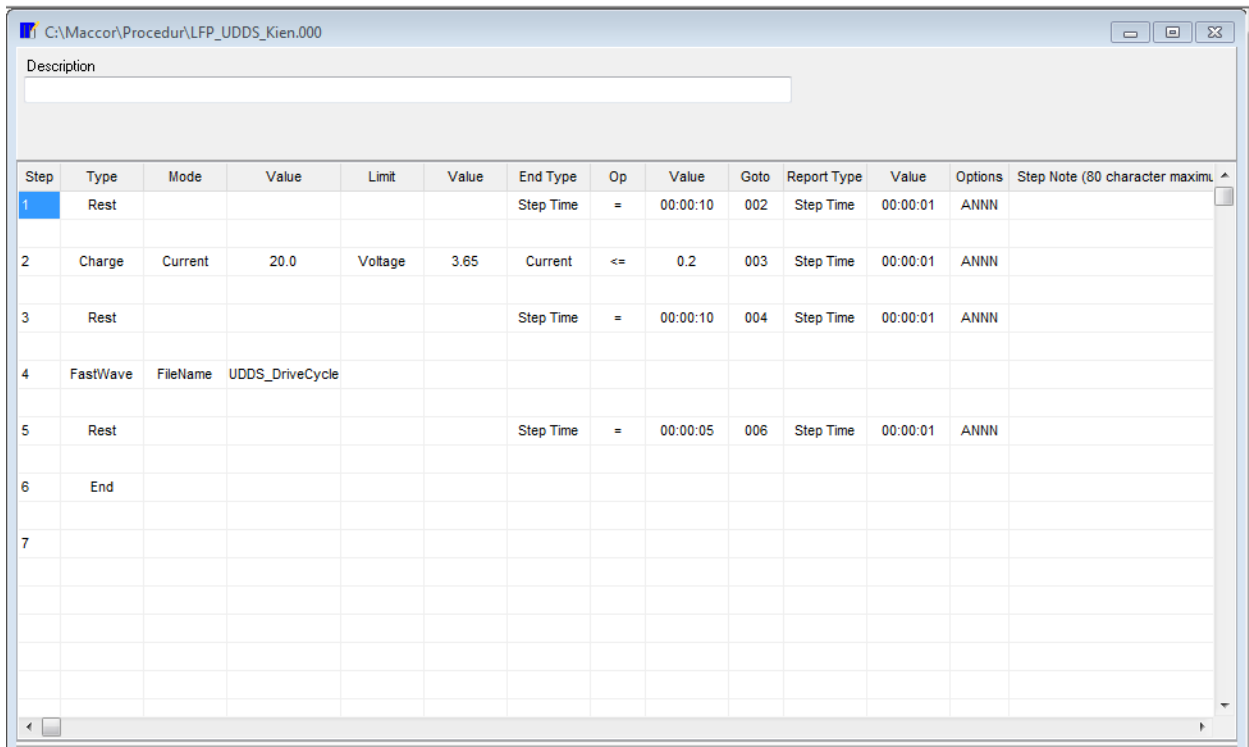
UDDS test procedure in Maccor

Step	Type	Mode	Value	Limit	Value	End Type	Op	Value	Goto	Report Type	Value	Options	Step Note (80 character maximum)
1	Rest					Step Time	=	00:00:05	002	Step Time	00:00:01	ANNN	
2	Do1												
3	Discharge	Current	28.0	Voltage	2.0	Current	<=	1.0	004	Step Time	:::1	ANNN	
4	Rest					Step Time	=	01:00:00	005			ANNN	
5	Charge	Current	28.0	Voltage	3.65	Current	<=	1.0	006	Step Time	:::1	ANNN	
6	Loop1					Loop Count	=	100	007				
7	Rest					Step Time	=	00:00:05	008	Step Time	00:00:01	ANNN	
8	End												
9													

Degradation test procedure in Maccor

Appendix B: OCV-SOC Look-up Table

OCV	SOC
0.00	2.24941
0.01	2.80739
0.02	2.92579
0.03	3.00159
0.04	3.05804
0.05	3.10301
0.06	3.14031
0.07	3.17066
0.08	3.19517
0.09	3.20547
0.10	3.20941
0.11	3.21186
0.12	3.21386
0.13	3.21612
0.14	3.21896
0.15	3.22401
0.16	3.22945
0.17	3.23441
0.18	3.23903
0.19	3.24324
0.20	3.24767
0.21	3.25191
0.22	3.25590
0.23	3.25966
0.24	3.26303
0.25	3.26602
0.26	3.26884
0.27	3.27182
0.28	3.27460
0.29	3.27719
0.30	3.28028
0.31	3.28266
0.32	3.28536
0.33	3.28779
0.34	3.28993
0.35	3.29223
0.36	3.29446
0.37	3.29603
0.38	3.29705

0.39	3.29774
0.40	3.29808
0.41	3.29887
0.42	3.29930
0.43	3.29977
0.44	3.30019
0.45	3.30032
0.46	3.30084
0.47	3.30120
0.48	3.30151
0.49	3.30191
0.50	3.30216
0.51	3.30237
0.52	3.30262
0.53	3.30299
0.54	3.30313
0.55	3.30374
0.56	3.30382
0.57	3.30400
0.58	3.30447
0.59	3.30462
0.60	3.30495
0.61	3.30543
0.62	3.30570
0.63	3.30630
0.64	3.30689
0.65	3.30757
0.66	3.30852
0.67	3.30953
0.68	3.31104
0.69	3.31280
0.70	3.31500
0.71	3.31819
0.72	3.32254
0.73	3.32795
0.74	3.33298
0.75	3.33619
0.76	3.33816
0.77	3.33924
0.78	3.33995
0.79	3.34039
0.80	3.34071
0.81	3.34096

0.82	3.34148
0.83	3.34194
0.84	3.34210
0.85	3.34254
0.86	3.34281
0.87	3.34310
0.88	3.34355
0.89	3.34398
0.90	3.34440
0.91	3.34494
0.92	3.34567
0.93	3.34622
0.94	3.34719
0.95	3.34849
0.96	3.35072
0.97	3.35562
0.98	3.36773
0.99	3.40754
1.00	3.57995

Appendix C: MATLAB Script - Fitting of First-Order ECM Parameters from HPPC

```matlab
%% Oct 27/2018
% Code for estimating the ECM model parameters from HPPC
tests
% Input is HPPC data that is a cell with n HPPC tests
% Each HPPC tests has one column of time (s), then current
(in A), and voltage
% (in V)
% The HPPC test should start with the first element being
the cell at rest
% before the 1C discharge.
% The test assumes that the SOC does not change within the
hppc window

%% Parameters to change in the code
currentLimit = 0.01; % Current above this limit will be
considered as 1C current
iniPar = [0.002;0.002;11000];

%% Parameters used in algorithm
xIni = 0;
[m,n] = size(dataHPPC{1});
outputPar = zeros(3,n);
modelError = zeros(m,n);
vModel = zeros(m,n);

%% Running the objective function and solving for the
parameters
for i = 1:n
    time = dataHPPC{1}(:,i);
    current = dataHPPC{2}(:,i);
    vExp = dataHPPC{3}(:,i);
    vActual = dataHPPC1{3}(:,i);
    % Find the ocvCurve value right before the HPPC test
starts
    index = find(current>currentLimit);
    ocvVoltage = vExp(index(1)-1);

    % Obtaining the parameter estimates
    fun =
@(beta,x)ObjectiveFunction(beta,x,ocvVoltage,xIni);
```

```matlab
    outputPar(:,i) =
nlinfit([time,current],vExp,fun,iniPar);

    % Running the voltage model with the given battery
parameters
    vModel(:,i) =
ObjectiveFunction(outputPar(:,i),[time,current],ocvVoltage,
xIni);
    modelError(:,i) =  abs((vModel(:,i) -
vActual)./vActual)*100;

    % Plotting scripts for the voltage model
    figure
    plot(vModel(:,i))
    hold on
    plot(vActual)

end

output = {outputPar, vModel, modelError};


%% A model that takes a single current value and calculates
the voltage
% response
% Inputs - current: the current value going into the cell
%         - tSample: the time sample for the data points
%         - xPrev: The previous state values for Vrc
%         - ocvVotlage: The open circuit voltage for the
cell.
%         - ECM_Parameters: The parameters of the ECM (r1,
r2, C, Capacity)

% Outputs - vModel: The model voltage for the cell at a
particular current
% input
%          - XTimUp: The updated state values for Vrc


function [vModel,XTimUp] = Model_Thevenin (current,
tSample, xPrev, ocvVoltage, ECM_Parameters)

% Model Parameters
r1 = ECM_Parameters(1);
```

```matlab
r2 = ECM_Parameters(2);
C = ECM_Parameters(3);

tau = r2*C;

%% State Time Update
XTimUp = exp(-tSample/(tau))*xPrev + r2*(1-exp(-
tSample/tau))*current;

%% The voltage response from the model
vModel = ocvVoltage-XTimUp(1)-r1*current;

end


%% The objective function for the least square algorithm

function [vModel] = ObjectiveFunction(ECM_parameters,
input, ocvVoltage,  xNew)

time = input(:,1);
current = input(:,2);

%% Using the initial terminal voltage as the OCV voltage.
vModel = zeros(length(current),1);
vModel(1) = ocvVoltage;

for i = 2:length(current)
    [vModel(i),xNew(1,i)] = Model_Thevenin (current(i),
(time(i)-time(i-1)), xNew(1,i-1), ocvVoltage,
ECM_parameters) ;
end
```

Appendix D: MATLAB Script – Simulation of Sensor Faults

```matlab
% Fault creation (simulation)
function [data] = FaultSim(file1, sensor, fault, faultsize,
pos)

% Load data

load(file1);
clean_data
time = data(:,1);
U = data(:,2);
I = data(:,3);
SOC = data(:,4);
OCV = data(:,5);
n = length(time);

% Fault selection and addition. U and I represent voltage
and current
% sensor faults, respectively. B and G represent bias and
gain faults,
% respectively.

if sensor == 'U'
    if fault == 'B'
        for i1 = pos:n
            U(i1) = U(i1) + faultsize;
        end
    elseif fault == 'G'
        for i2 = pos:n
            U(i2) = U(i2)*(1+faultsize/100);
        end
    end
elseif sensor == 'I'
    if fault == 'B'
        for i3 = pos:n
            I(i3) = I(i3) + faultsize;
        end
    elseif fault == 'G'
        for i4 = pos:n
            I(i4) = I(i4)*(1+faultsize/100);
        end
```

```matlab
        end
    end

    data(:,2) = U;
    data(:,3) = I;
end
```

Appendix E: MATLAB Script – FDI Algorithm Simulation and Evaluation

```matlab
% Final Script - FDI Simulation and Evaluation

clc
clear

% Load initial guesses for each data file
load('InitialGuess.mat')

% Seting up faulted data
% FaultSim(datafile,U/I,B/G,fault size,fault location)
position = 30000;
data = FaultSim('UDDS_Apr25.mat','U','G',0,position);
test = 1; %for initial guess

% Input data from file
time = data(:,1);
U = data(:,2);
I = data(:,3);
SOC = data(:,4);
OCV = data(:,5);

% RLS
T = 0.5;
n = length(time);

R0_ini = InitialR0(test);
R1_ini = InitialR1(test);
C1_ini = InitialC1(test);

P = diag([0.00005,0.02,0.00005,0.00005]);
U_mod = zeros(n,1);
R0_curve = zeros(n,1);
R1_curve = zeros(n,1);
C1_curve = zeros(n,1);
U_mod(1) = U(1);

R0 = R0_ini;
R1 = R1_ini;
C1 = C1_ini;
```

```matlab
R0_curve(1) = R0_ini;
R1_curve(1) = R1_ini;
C1_curve(1) = C1_ini;
for i = 2:n
    [R0,R1,C1,K,P,Umod] =
RLS_func_1st(R0,R1,C1,U(i),I(i),U(i-1),I(i-
1),T,OCV(i),OCV(i-1),P);
    U_mod(i) = Umod;
    R0_curve(i) = R0;
    R1_curve(i) = R1;
    C1_curve(i) = C1;
end
err = immse(U,U_mod);

% Weighted moving average
R0_pre = zeros(n,1);
R1_pre = zeros(n,1);
C1_pre = zeros(n,1);
R0_pre(1) = R0_ini;
R1_pre(1) = R1_ini;
C1_pre(1) = C1_ini;
res1 = zeros(n,1);
res2 = zeros(n,1);
res3 = zeros(n,1);
S1 = zeros(n,1);
S2 = zeros(n,1);
S3 = zeros(n,1);
F1 = zeros(n,1);
F2 = zeros(n,1);
F3 = zeros(n,1);
% Equation 3.17
for i = 2:n
    R0_pre(i) = 0.01*R0_curve(i) + 0.99*R0_pre(i-1);
    R1_pre(i) = 0.01*R1_curve(i) + 0.99*R1_pre(i-1);
    C1_pre(i) = 0.01*C1_curve(i) + 0.99*C1_pre(i-1);
end

% CUSUM
for i = 1000:n
    % Equation 3.18
    res1(i) = abs(R0_curve(i)-R0_pre(i))/R0_pre(i);
    res2(i) = abs(R1_curve(i)-R1_pre(i))/R1_pre(i);
    res3(i) = abs(C1_curve(i)-C1_pre(i))/C1_pre(i);
    % Equation 3.19
```

```matlab
        S1(i) = max(0, (S1(i-1) + res1(i-1)-0.0001));
        S2(i) = max(0, (S2(i-1) + res2(i-1)-0.005));
        S3(i) = max(0, (S3(i-1) + res3(i-1)-0.005));
end

%Fault detection
for i = 1000:n
if S1(i) > 0.01
    F1(i) = 1;
end
if F1(i-1) == 1
    F1(i) = 1;
end
if S2(i) > 0.1
    F2(i) = 1;
end
if F2(i-1) == 1
    F2(i) = 1;
end
if S3(i) > 0.1
    F3(i) = 1;
end
if F3(i-1) == 1
    F3(i) = 1;
end
end

DT = min([find(F1,1) - position; find(F2,1) - position;
find(F3,1) - position]);

%Fault isolation
if F1(DT+position) > 0
    fprintf('The fault was detected after %d seconds and
isolated to be a current sensor fault',DT)
elseif F2(DT+position) > 0 | F3(DT+position) > 0
    fprintf('The fault was detected after %d seconds and
isolated to be a voltage sensor fault',DT)
else
    fprintf('There was no fault detected')
end

%Plotting
closeup = 28000:32000;
```

```matlab
figure
plot(closeup,res1(closeup));
xlabel('Time (s)')
ylabel('APE R0')
set(gca, 'FontName', 'Calibri')
set(gca, 'FontSize', 16)
figure
plot(closeup,res2(closeup));
xlabel('Time (s)')
ylabel('APE R1')
set(gca, 'FontName', 'Calibri')
set(gca, 'FontSize', 16)
figure
plot(closeup,res3(closeup));
xlabel('Time (s)')
ylabel('APE C1')
set(gca, 'FontName', 'Calibri')
set(gca, 'FontSize', 16)
figure
plot(closeup,S1(closeup));
hold on
plot(closeup,ones(size(closeup))*0.01,'r--');
xlabel('Time (s)')
ylabel('CUSUM APE R0')
set(gca, 'FontName', 'Calibri')
set(gca, 'FontSize', 16)
figure
plot(closeup,S2(closeup));
hold on
plot(closeup,ones(size(closeup))*0.1,'r--');
xlabel('Time (s)')
ylabel('CUSUM APE R1')
set(gca, 'FontName', 'Calibri')
set(gca, 'FontSize', 16)
figure
plot(closeup,S3(closeup));
hold on
plot(closeup,ones(size(closeup))*0.1,'r--');
xlabel('Time (s)')
ylabel('CUSUM APE C1')
set(gca, 'FontName', 'Calibri')
set(gca, 'FontSize', 16)

figure
```

```matlab
plot(closeup,F1(closeup));
xlabel('Time (s)')
ylabel('Fault F_I')
set(gca, 'FontName', 'Calibri')
set(gca, 'FontSize', 16)
figure
plot(closeup,F2(closeup));
xlabel('Time (s)')
ylabel('Fault F_U')
set(gca, 'FontName', 'Calibri')
set(gca, 'FontSize', 16)
figure
plot(closeup,F3(closeup));
xlabel('Time (s)')
ylabel('Fault F_U')
set(gca, 'FontName', 'Calibri')
set(gca, 'FontSize', 16)

figure
plot(time,R0_curve);
hold on
plot(time,R0_pre);
a2 = axes();
a2.Position = [0.5 0.5 0.3 0.3]; % xlocation, ylocation,
xsize, ysize
plot(29000:31000,R0_curve(29000:31000))
hold on
plot(29000:31000,R0_pre(29000:31000)); axis tight
annotation('ellipse',[.625 .225 .05 .07])
annotation('arrow',[.65 .65],[.32 .43])

figure
plot(time,R1_curve);
hold on
plot(time,R1_pre);
a2 = axes();
a2.Position = [0.5 0.5 0.3 0.3]; % xlocation, ylocation,
xsize, ysize
plot(29000:31000,R1_curve(29000:31000))
hold on
plot(29000:31000,R1_pre(29000:31000)); axis tight
annotation('ellipse',[.625 .225 .05 .07])
annotation('arrow',[.65 .65],[.32 .43])
```

```matlab
figure
plot(time,C1_curve);
hold on
plot(time,C1_pre);
a2 = axes();
a2.Position = [0.5 0.5 0.3 0.3]; % xlocation, ylocation,
xsize, ysize
plot(29000:31000,C1_curve(29000:31000))
hold on
plot(29000:31000,C1_pre(29000:31000)); axis tight
annotation('ellipse',[.625 .225 .05 .07])
annotation('arrow',[.65 .65],[.32 .43])


% RLS function
function [R0,R1,C1,K,P,Umod] =
RLS_func_1st(R0,R1,C1,Uk1,Ik1,Uk0,Ik0,T,OCV1,OCV0,P)
% Equation 3.4
a1 = T/(R1*C1) - 1;
% Equation 3.5
a2 = -R0;
% Equation 3.6
a3 = R0 - T/C1 - (T*R0)/(R1*C1);
lambda = 0.99999;
theta = [1 ; a1 ; a2 ; a3];
phi = [OCV1; (OCV0-Uk0); Ik1; Ik0];
% Equation 3.10
Umod = transpose(theta)*phi;
% Equation 3.13
K = (P*phi)/(lambda + transpose(phi)*P*phi);
% Equation 3.14
P = (P-K*transpose(phi)*P)/lambda;
% Equation 3.15
theta = theta + K*(Uk1-transpose(theta)*phi);
a1 = theta(2);
a2 = theta(3);
a3 = theta(4);
% Equation 3.5
R0 = -a2;
% Equation 3.7
R1 = -(a3-a1*a2)/(1+a1);
% Equation 3.8
C1 = -T/(a3-a1*a2);
end
```